Investigations on the F region of the ionosphere over low latitudes using optical, radio and simulation techniques

A THESIS

submitted for the award of Ph. D degree of

MOHANLAL SUKHADIA UNIVERSITY

in the

Faculty of Science

by

Dibyendu Chakrabarty

Under the Supervision of

Ramanathan Sekar, Associate Professor, Physical Research Laboratory, Ahmedabad

DEPARTMENT OF PHYSICS

FACULTY OF SCIENCE

MOHANLAL SUKHADIA UNIVERSITY

UDAIPUR

Year of Submission: 2007

Dedicated to

my daughter, Ayushi

DECLARATION

I hereby declare that the work incorporated in the present thesis entitled, “Investigations on the F region of the ionosphere over low latitudes using optical, radio and simulation techniques” is my own work and is original. This work (in part or in full) has not been submitted to any University for the award of a Degree or a Diploma.

Signature of the candidate

CERTIFICATE

I feel great pleasure in certifying that the thesis entitled, “Investigations on the F region of the ionosphere over low latitudes using optical, radio and simulation techniques” embodies a record of the results of investigations carried out by Dibyendu Chakrabarty under my guidance.

I am satisfied with the analysis of data, interpretation of results and conclusions drawn.

He has completed the residential requirement as per rules.

I recommend the submission of thesis.

Date :

Ramanathan Sekar
Associate Professor
(Thesis Supervisor)

Acknowledgements

At the onset, I express my sincere gratitude to Prof. R. Sekar for his invaluable guidance and concern. His scientific objectivity and criticality induced in me an attitude to probe deeper into any given scientific issue. He was a ‘friend’ disguised as thesis supervisor and the informal relationship gave me space to argue freely on several scientific issues. This, in a way, concretized many of the ideas that are recorded in this work. I am greatly indebted to Prof. R. Sridharan as he moulded me into the form of a researcher during the initial phase of my career. I always look up to him for inspiration. During the course of this work, I learnt many things from the discussions with Prof. A. C. Das whose humility I found amazing. I had the priviledge to interact with Prof. R. Raghavarao and Dr. R. Suhasini during my career in PRL. The concern and affection showered by them kept me motivated all the time. I had the good fortune to interact with Prof. P. B. Rao many times during the course of this work. His interest in my work kept me interested in my job. It was always enjoyable to have discussions with Prof. K. N. Iyer. His conceptual clarity coupled with gentle demeanour made huge impact on me. I learnt many things from the work of Prof. J. H. Sastri whose expertise in storm -time physics is fascinating. I thank Prof. Archana Bhattacharyya for her kind support and encouragement all the time. I also thank Dr. B. V. Krishna Murthy and Dr. Sampath for the stimulating discussions I had with them. Prof. V. M. Vasyliunas and Prof. R. A. Wolf were kind enough to send me some rare and important reprints pertaining to magnetosphere-ionosphere coupling. I thank them for their kind gesture.

I am grateful to former PRL director Prof. G. S. Agarwal for allowing me to pursue my doctoral work. I express my sincere gratitude to Prof. J. N. Goswami, PRL director, for his magnanimous support and encouragement. I am thankful to the Dean, PRL for his concern. Thanks to all the faculty members in the Academic Committee who were particularly supportive.

I am fortunate to have great colleagues in our group with whom learning and office hours were/are so much fun. I am greatly indebted to Mr. R. Narayanan and Mr. N. K. Modi for teaching me the experimental nuances of our field and helping me out on innumerable occasions. I enjoyed discussing with Dr. S. P. Gupta whose diverse knowledge was helpful to provide clues to many scientific problems on several occasions. I thank Drs. D. Pallam Raju, S. Gurubaran, Alok Taori, E. A. Kherani, Ms. Ranna Patel, Mrs. Vijaya Mutagi, Mr. S. R. Das, Late Mr. C. L. Piplapure for their support and interest in

my work. I am thankful to Dr. Tarun K. Pant for helping me to learn the scientific nuances of the field at the initial phase of my career and for being supportive throughout. I thank Mr. Sumanta Sarkhel for making our lab a happy place.

The faculty members in our division were always there to lend helping hands to me. The support, and generous encouragements provided by Prof. Shyamlal, Prof. Jayaraman, Dr. Bhas Bapat, Prof. K. P. Subramanian, Prof. Harish Chandra, Prof. R. G. Rastogi, Prof. H. S. S. Sinha and Prof. S. A. Haider were extremely valuable for my scientific growth. Scientific and technical feedbacks obtained from Dr. Ramchandran and Dr. Varun sheel helped me to improve and I thank them for their generosity. I thank Vandana for helping me on various occasions and Rajesh as well as Venkat for various technical helps at different points of time. The presence of Som, Sanat, Uma, Dilip, Amit, Sunil, Swaroopda, Lokesh, Duli, Prabir, Manish and many others made our area a delightful place and I thank them all for their spirit.

I would like to acknowledge at this point the generous help that I obtained from PRL workshop at the time of fabrication of the airglow instrument which is used for the present work. Generous help provided by Mr. G. P. Ubale and his team is highly acknowledged. Mr. P. K. Solanki from the workshop assisted me in many of my field campaigns. He deserves special thanks. The prompt and efficient service provided by PRL library deserves a special mention. Mrs. Nistha Anilkumar from the library helped me in procuring various articles from time to time and I sincerely acknowledge her help and the whole library team's effort to facilitate research in PRL. My colleagues from the computer center / accounts / stores/ purchase / maintenance divisions of PRL made my job easier. I thank them all.

During the course of this work, I spent many days at NARL, Gadanki to conduct coordinated MST radar and airglow experiments. I sincerely thank Director, NARL for the generous support provided to us. I am indebted to Dr. Amit K. Patra, NARL for many useful discussions. His students especially Dr. S. Sripathy and Mr. N. Venkateswara Rao helped me on many occasions on the technical and computational aspects of MST radar. I am grateful to them. I thank Dr. V. K. Anandan for kindly giving me permission to use the ADP software. The support of the technical staffs of NARL especially Dr. Chandrasekhar Sarma is highly acknowledged. It would have been impossible to conduct airglow experiment from Gadanki without the enthusiastic support of all the staffs on various occasions. I thank them all.

I thank Dr. Rajesh Pande and Dr. Nirvikar Dashora of M. L. S. University, Udaipur

for helping me in different official matters related to the M. L. S. University, Udaipur.

Since I joined PRL, I came across so many friends and day-to-day interactions with them enriched me on both professional and personal fronts. I cherished the companies of Swaroopda-Subhradi, Tarun, Siva, Anil, Som, Shashi, Rajesh (T.A.), Panda, Ravi-Sravanidi, Navinji-Priti, Rama, Varun-Joona, Prashant, Jyoti, Venkat, Bhavsar Bhai, Anirban, Koushik, Rajesh (Agnihotri), Soumen, Subrata, Vinai, Sankar, Anil (Patnaik), Rajneesh, Sudhir (Vempatik), Kuljeet, Jayesh, Deshpande, and many others. I thank them all for their contributions in making my life enjoyable.

I am indebted to my baba and ma for bringing me up with love and affection despite tremendous hardships in their respective lives. The affection and support provided by my sister, dida, mama and my masis deserve special mention. The whole Saha family provided me the the logistic as well as emotional space to fall upon whenever I needed. I am thankful to them. My friends Sona, Shankar, Raju, Nabu and their families helped me on innumerable occasions. The support of didi-puranjanda, gablu-nimmi, ratul-rahul, my mother-in-law and late father-in-law are priceless. This work would not have been possible without the compassion, tolerance and support of my wife Amrita and maturity shown by our daughter Ayushi.

List of Publications

Publications related to the thesis work

- Sekar, R., D. Chakrabarty, R. Narayanan, S. Sripathi, A. K. Patra, and K. S. V. Subbarao, Characterization of VHF radar observations associated with equatorial Spread F by narrow-band optical measurements
  Ann. Geophys., 22, 3129, 2004

- Chakrabarty, D., R. Sekar, R. Narayanan, C. V. Devasia and B. M. Pathan, Evidence for the interplanetary electric field effect on the OI 630.0 nm airglow over low latitude
  J. Geophys. Res., 110, A11301, doi:10.1029/2005JA011221, 2005

- Chakrabarty, D., R. Sekar, R. Narayanan, A. K. Patra, and C. V. Devasia, Effects of interplanetary electric field on the development of an equatorial spread F event
  J. Geophys. Res., 111, A12316, doi: 10.1029/2006JA011884, 2006

- Sekar, R., and D. Chakrabarty, Non-linear simulation model investigation on the development of a pre-midnight plume event associated with storm-time electric field
  Communicated to *J. Atmos. Sol-Terr. Phys.*, 2007

- Sekar, R., D. Chakrabarty, R. Narayanan and C. V. Devasia, On the dependence of 777.4 nm airglow on ionospheric parameters
  To be communicated to *Ann. Geophys.*, 2007

- Sekar, R., D. Chakrabarty, R. Narayanan and A. K. Patra, Coordinated observations of Equatorial Spread-F by means of VHF radar and optical techniques over Indian zone
  To be communicated to *Ann. Geophys.*, 2007

Other publications (2004 onwards)

- Chakrabarty, D., R. Sekar, R. Narayanan, Tarun K. Pant and K. Niranjan, Thermospheric gravity wave modes over low and equatorial latitudes during daytime
  J. Geophys. Res., 109, A12309, doi:10.1029/2003JA010169, 2004

- Sekar, R., and D. Chakrabarty, Impact of space weather events on the coupling of ionosphere and thermosphere over low latitudes, *Asian J. of Phys.*, 16, 247, 2007

- Rastogi, R. G., H. Chandra, D. Chakrabarty, K. Kitamura, and K. Yumoto, Day-to-day correlation of equatorial electrojet at two stations separated by 2000km, *Ann. Geophys.*, 25, 875, 2007

Abstract

Equatorial Spread F (ESF) phenomenon affects radio frequency communication even in UHF range. Theoretical modeling studies revealed that plasma enhancement structures beyond 350 km can also get generated during ESF evolution alongside the depletion structures. The degree of enhancement was found to be orders of magnitude smaller than the degree of depletion. Therefore, it was realized that in order to experimentally detect those enhancement structures, one needs an improved (with high signal-to-noise ratio) photometric technique in conjunction with radar technique. Keeping this in mind, a narrow band (0.3 nm) multiwavelength photometer was fabricated and operated from Gadanki, the site of Indian MST radar. The field of view of the photometer was chosen to be equal to the VHF radar beam width ($\sim 3^o$). Based on four years of coordinated optical and radar observations from Gadanki in campaign modes along with satellite, magnetometer and ionosonde data, several unresolved/partially resolved scientific issues pertaining to ESF, space weather and 777.4 nm airglow emission are addressed. A scientific background of these issues is built up in Chapter 1 and the salient features of the observational techniques are described in Chapter 2.

Chapter 3 brings out the observational evidence of the plasma enhancement structures associated with ESF and predicted by modeling studies. In addition to that, characterization of different ESF structures are done based on simultaneous radar and optical observations. Chapter 4 elicits the evidences of the effects of interplanetary electric field (IEF) on 630.0 nm airglow as well as on ESF development. Taking clues from these observations, non-linear numerical simulation studies were carried out to prove that storm-time electric field is a necessary but not sufficient condition for the development of pre-midnight plasma plume associated with storm-time ESF events. This aspect is reported and discussed in Chapter 5. Investigations on the dependence of 777.4 nm airglow emission on the ionospheric parameters on non-ESF nights are reported in Chapter 6.

Keywords

Equatorial Spread-F, Space weather, Geomagnetic storm, airglow, Prompt penetration, Shielding, Undershielding, Overshielding, Numerical simulation

Contents

Chapter 1

Introduction

Earth's atmosphere played a pivotal role in the evolution of life on earth. Terrestrial atmosphere blocks the high energy part of the solar radiation rendering the earth's surface habitable for human beings. Therefore, it is important to understand the properties of different regions of terrestrial atmosphere and the coupling between them so that the properties of the whole atmospheric system can be understood in totality and its response to external perturbation can be predicted. Terrestrial upper atmosphere is greatly modified by the vagaries of the sun, our nearest star. The influence of the sun on terrestrial upper atmosphere is many-fold. However, the effects are sometimes direct and sometimes indirect, complicated. The presence of plasma in the terrestrial upper atmosphere and Earth's magnetic field enhance the complexity of that region as both plasma and neutral processes are important and the coupling between them determine the properties of the medium. The objective of the present work is, however, to study certain important aspects of the plasma-neutral coupling processes in the context of terrestrial upper atmosphere.

1.1 Thermosphere

The terrestrial upper atmosphere comprises of both neutral and plasma species. The temperature of the neutral species sharply increases from $\sim$150K to $\sim$1500K as the altitude is increased from $\sim$90km to $\sim$500km (Figure 1.1). This portion of the terrestrial atmosphere is known as thermosphere. In the thermosphere, the neutral particles maintain diffusive equilibrium above the turbopause which is situated at $\sim$100km. This means that the vertical distribution of the neutrals is governed by the respective masses of the species. For example, at $\sim$300km the O_2 concentration is $\sim 10^7$ per cc whereas the O concentration

is $\sim 10^9$ per cc. Therefore, this region of the terrestrial atmosphere where turbulent mixing ceases and molecular diffusion takes over is often referred to as heterosphere. It is noteworthy that thermosphere starts from the coldest region of the terrestrial atmosphere and extends to the hottest region. Heat conduction in the thermosphere takes place in the downward direction so that the thermospheric temperature increases upward. However, beyond a certain altitude, the heat conductivity becomes so high that the temperature in the upper thermosphere does not change much with altitude generating a nearly isothermal condition. The major constituents of thermosphere are O, O_2 and N_2. Molecular

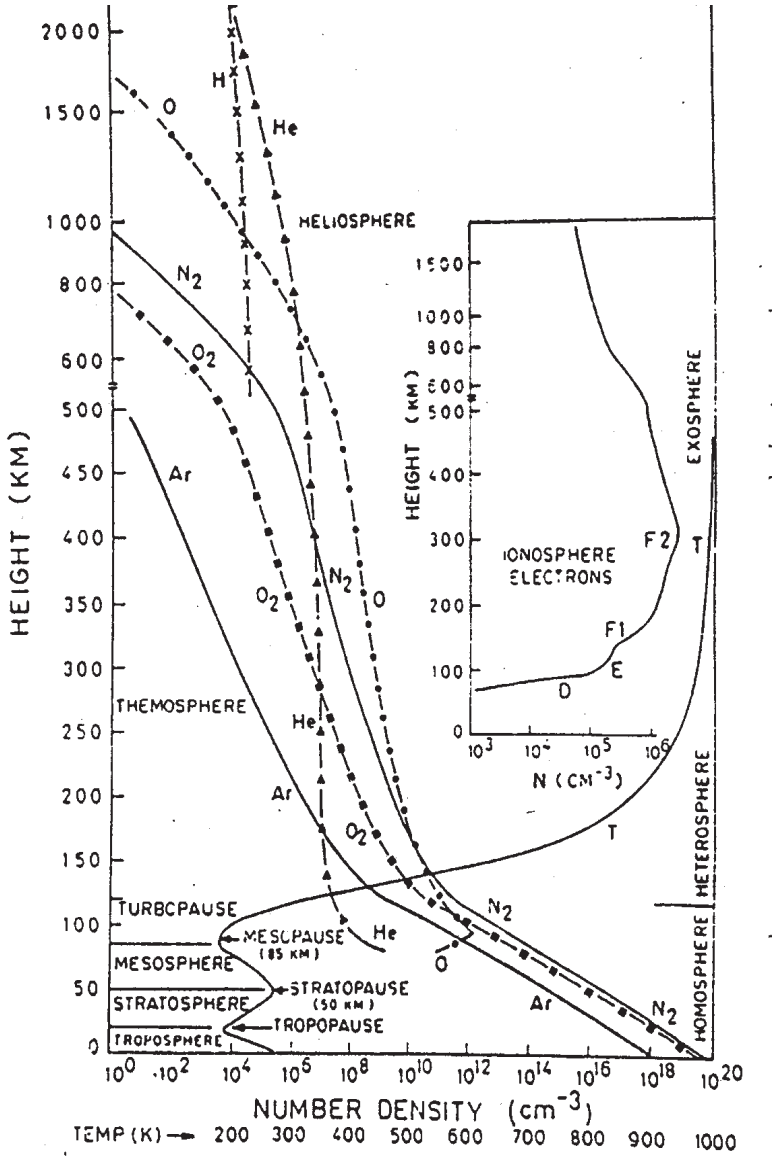

Figure 1.1: Typical temperature profile of neutral atmosphere and plasma density profile of ionosphere. Thermosphere and F region of the ionosphere are marked respectively in left and right figures. Note that a major part of terrestrial ionosphere is embedded in thermosphere enforcing plasma-neutral coupling processes to be important in this region (from *Pallam Raju,* 1996).

oxygen gets photodissociated in the lower thermosphere by the Schumann-Runge continuum ($\sim$130-175 nm) of solar radiation to form the atomic oxygen in a metastable state (O^1D) which gets collisionally quenched in the medium leading to local heating [e.g. *Stolarski et al.*, 1975, 1976]. In the middle and upper thermosphere, solar EUV radiation ($\leq$102.7 nm) causes photo-ionization which generates energetic photoelectrons. The collisions of these photoelectrons with surrounding ions and neutrals also contributes to thermospheric heating. However, a part of total photoelectron energy is lost in space through participation in the chemical reactions involving atoms and molecules that produces airglow radiations. Therefore, the thermal equilibrium in the thermosphere is obtained mostly by the interplay between the absorption of solar UV/EUV radiation and the downward heat conduction. However, during geomagnetically disturbed periods, the energetic particle precipitation and the joule heating associated with enhanced auroral electrojet current system in the auroral latitudes provide additional heat sources for the thermosphere. The radiative cooling by CO_2 and NO (minor constituents) also contributes to the thermal budget of the lower thermosphere to some extent. Tides, atmospheric gravity waves (AGW) and planetary waves also contribute to the thermospheric energy budget. The global thermospheric energy budget is discussed in detail in *Killeen* [1987].

1.2 Ionosphere

Ionosphere is a partially ionized medium with sufficient plasma density to affect radio propagation. Charge particles in the ionosphere over low-equatorial latitudes owing to mainly the photo-ionization of neutrals by the solar radiation. As the strength of ionizing solar radiation falls off with decreasing altitude and the neutral atmospheric gas concentration falls off with increasing altitude, a trade-off is attained from $\sim$60 km to 1000 km in the terrestrial atmosphere and ionized layers get formed. Although the charge number densities are 2-3 orders less than the neutral number densities in the ionosphere, the charge particles influence the medium's electrical properties substantially. The ionosphere is classified into D (60-90km), E (95-150 km) and F ($>$150 km) region (Figure 1.1). Solar X-rays (0.1-0.8 nm), H L_y α (121.6 nm) absorption by NO and cosmic rays cause the D region ionization. Solar X-rays (0.8-14 nm) and UV radiation (79.6-102.7 nm) play important roles in the ionization of E region whereas F region ionization is mostly caused by radiation roughly in the range of 14.0-79.6 nm. During daytime, on occasions, F region splits into two sub-layers, F1 and F2, a feature that is absent during nighttime.

The molecular ions (e.g. NO^+ and $O_2{}^+$) dominate the E and lower F regions and the loss rate in these regions follow square law. However, in the upper F region, atomic ions (e.g. O^+) dominate and linear loss rate prevails over the square loss rate. The transition between the square and linear loss processes takes place at an altitude range of $\sim$160-200 km. When this transition region coincides with the altitude (which may vary from one day to another) at which F layer ion production maximizes, F layer splits into F1 and F2 sub-layers. It is important to note that control of the geomagnetic field over the charge particles in ionosphere varies in the D, E and F region. In the D region, the movement of both ions and electrons are dominated by collisions with neutrals rather than the magnetic field (Collision frequency, $\nu_{i,e} \gg$ Gyro frequency, $\omega_{i,e}$; at 80km, $(\frac{\nu}{\omega})_i \gg 1$, $(\frac{\nu}{\omega})_e \approx 2$). In the E region, however, geomagnetic field governs movement of electrons while ions are still dominated by collision processes ($\nu_i > \omega_i$ but $\nu_e < \omega_i$; at 120 km, $(\frac{\nu}{\omega})_i \approx 2$,$(\frac{\nu}{\omega})_e \ll 1$). Both electrons and ion movements are controlled by magnetic field in the F region ($\nu_{i,e} \ll \omega_{i,e}$; at 300 km, $(\frac{\nu}{\omega})_i \approx \frac{1}{300}$, $(\frac{\nu}{\omega})_e \ll 1$). A comparison of the collision and gyro frequencies of ions and electrons is provided in *Rishbeth* [1997]. One of the important properties of the ionospheric F region is that the region is dominated by transport processes and the life-times of the atomic ions are of the order of a few hours. As a result, even in the absence of ionizing radiation, F layer survives at nighttime. On the other hand, E layer attains photochemical equilibrium during daytime and contains negligible ionization at nighttime as most of the ionization is annihilated by the faster recombination processes.

1.3 Ionosphere-thermosphere system, ITS

The production, loss and transport processes determine the temporal variation of ionospheric plasma at F region altitudes throughout the globe. Production, and transport processes vary considerably with altitude, latitude, longitude, local time, season, solar activity. The spatial distribution of plasma also depends on the characteristic ionospheric dynamical processes that are, on many occasions, vastly different at different latitudes. The fact that geomagnetic field strengths and orientations are different at different latitudes influences the plasma processes significantly. For example, the field strengths at the polar region are nearly double ($\sim 5 \times 10^{-5}$ Tesla or 0.5 Gauss) to that at the equator ($\sim$0.38 Gauss) at F region altitudes. The orientation of the field lines is perpendicular to the surface over polar region whereas the field lines are horizontal over equator. Therefore, magnetic field strength and orientation affects ionospheric dynamics (for example,

plasma drifts) over different latitudes. Ionospheric variabilities are intricately connected with the variations in the thermospheric dynamics as the plasma and neutral processes in the upper atmosphere maintain a feedback relationship. This feedback relationship brings the coupling between ionosphere and thermsophere (ionosphere-thermosphere system, ITS) through actions of the dynamical drivers like winds (both zonal and meridional), waves (e.g. tides, atmospheric gravity waves and planetary waves) and electric fields. In addition, ionosphere and thermosphere coupling is also mediated by chemical processes.

1.3.1 Effects of neutral wind

Thermospheric neutral wind can flow in meridional, zonal and vertical directions. Meridional wind can push the plasma up and down the magnetic field lines through the effects of collisional drag between the plasma and neutrals [e.g *Rishbeth*, 1977, 1998]. As a consequence, the height of ionospheric F layer changes. Therefore, it is implied that meridional wind is not effective in causing ionospheric height variation over magnetic dip equator as the geomagnetic field lines are horizontal to ground there. However, away from dip equator (for a place with finite dip angle), the F region vertical plasma drifts are always affected by the contribution from finite meridional wind [e.g. *Krishna Murthy et al.*, 1990]. As the meridional wind changes the F layer height, the plasma loss processes through recombination also change. Meridional wind can also affect the development of plasma instability structures in the equatorial F region during nighttime by changing the flux-tube integrated conductivity [e.g. *Devasia et al.*, 2002; *Abdu et al.*, 2006]. The direction of meridional wind is important to decide whether the F layer ascends or descends in altitude [e.g. *Rishbeth*, 1977]. In general, the average meridional wind direction is poleward during daytime and equatorward during nighttime. During daytime, the equatorial thermosphere is hotter than polar thermosphere as it receives maximum solar radiation. Therefore, meridional wind flows from equator to poles. However, during nighttime, the direction of meridional wind is generally from poles to equator. Zonal wind, on the other hand, is westward during daytime and eastward during nighttime in the F region. Zonal wind speed is, in general, maximum near midnight and minimum in the pre-dawn hours. Zonal wind gives rise to electric fields through dynamo action although the generation mechanisms are not exactly similar for E (during daytime) and F regions (during nighttime). E region dynamo, in principle, acts as voltage generator where the tidal wind plays a crucial role. F region dynamo, on the other hand, acts as current generator. Character-

istics of E and F region dynamo mechanisms are discussed comprehensively in *Rishbeth* [1997]. Both meridional and zonal winds exhibit latitudinal, longitudinal, seasonal, solar cycle and magnetic activity dependencies [e.g. *Sipler and Biondi*, 1978; *Merwether et al.*, 1986; *Gurubaran*, 1993; *Pant*, 1998; *Emmert et al.*, 2001; *Liu et al.*, 2006]. For example, the magnetic disturbance associated meridional and zonal winds are, in general, equatorward and westward respectively. The third component of the wind vector is vertical wind on which observations are sparse [e.g. *Raghavarao et al.*, 1987, 1993; *Biondi and Sipler*, 1985; *Herrero and Meriwether*, 1994]. Vertical wind can play an important role in thermospheric dynamics [e.g. *Raghavarao et al.*, 1993; *Smith*, 1998] and in the growth of plasma instability processes associated with Equatorial Spread F [e.g. *Sekar and Raghavarao*, 1987; *Raghavarao et al.*, 1993].

1.3.2 Effects of waves

ITS is intricately coupled with the other atmospheric regions. Atmospheric gravity waves (AGW) [*Hines*, 1960] play a significant role in the coupling of ITS with the lower atmosphere. Some modes of the gravity waves, which are originated in the lower atmosphere, escape the dissipation process at the mesopause region and penetrate into TIS [e.g.*Killeen and Johnson*, 1995]. AGWs that affect ITS over low-equatorial latitudes are mostly generated in the lower atmosphere due to orographic variations [e.g. *Meriwether et al.*, 1996] or tropospheric weather disturbances [e.g. *Bertin et al.*, 1978] or generated in the higher latitudes [e.g. *Oliver et al.*, 1997] due to the intensification of auroral electrojet current system during geomagnetic storms. Seeding of Equatorial Spread F (ESF) and associated plasma irregularity development [e.g.*Nicolls et al.*, 2005] is an example of AGW affecting the F region ionosphere over low latitudes. Preferred modes of thermospheric AGW over low-equatorial latitudes during quiet and disturbed periods have been reported by *Chakrabarty et al.*[2004]. Tides and gravity waves have long been identified to be contributors in the thermospheric heat budget [e.g. *Hines*, 1965]. Planetary waves are also found to affect ionosphere. For example, *Rastogi et al.*[2007] reported 15 day periodicity in the variations of horizontal magnetic field (H) during daytime over two dip equatorial stations separated by almost 33^o in longitude which is indicated to be due to planetary waves.

1.3.3 Effects of electric fields

Above ∼90 km, motion of ionospheric electrons is controlled by geomagnetic field lines and movements of the electrons across geomagnetic field lines under the influence of neutral wind are not possible. However, under the effect of an electric field, electrons drift in the Hall direction (perpendicular to electric and magnetic field). In F region, under the effect of eastward electric field, the plasma drift takes place in the vertical direction (upward during daytime and downward during nighttime) and zonal plasma drift (westward during daytime and eastward during nighttime) occurs under the influence of vertical electric field . F region zonal plasma drift has lot of altitudinal variations whereas vertical plasma drift exhibits enormous temporal variabilities. Vertical plasma drift patterns on a global scale were investigated in detail by *Fejer, et al.*, [1995] based on AE-E satellite observations. Investigation on F region vertical and zonal plasma drift patterns over dip equator is reported by *Fejer et al.*, [1991, 2005] based on Jicamarca observations. Moreover, seasonal variations in F region vertical and zonal plasma drifts based on the Jicamarca radar data are described in detail in *Fejer et al.* [1979] and *Fejer et al.* [1981] respectively. Comprehensive reviews on the investigations pertaining to vertical and zonal plasma drifts over dip equator is available in *Fejer* [1997]. As discussed in *Kelley* [1989], zonal drifts are larger in magnitude than their vertical counterpart and over a period of a day, the peak eastward zonal drift at night is generally larger than the peak westward zonal drift during daytime. It is also noted that vertical drift is enhanced during the post-sunset hours (near the sunset terminator) to a great extent. This feature is found to be absent during pre-dawn hours (near the sunrise terminator). In addition to that, strong solar cycle effects are seen in vertical drifts although seasonal effects are moderate in both the drifts. Electric field perturbations associated with geomagnetic disturbances affect the vertical and zonal drifts over dip equator [e.g. *Fejer and Scherliess*, 1997; *Scherliess and Fejer*, 1997, 1999; *Scherliess and Fejer*, 1998; *Fejer and Scherliess*, 1998].

1.3.4 Effects of chemical processes

Neutrals and plasma in ITS participate in various chemical reactions that contribute to energetics of the region. Plasma in the F region is provided by mainly the photoionization of atomic oxygen by solar radiation in the wavelength range of 14.0-79.6 nm.

$$O + h\nu \longrightarrow O^+ + e \tag{1.1}$$

O^+ ions, thus generated are lost by charge exchange processes and molecular ions such as $O_2{}^+$ and NO^+ are produced. However, the loss process of O^+ ions is a two step process.

1. Charge exchange with N_2 and O_2 and production of molecular ions.

$$O^+ + O_2 \xrightarrow{k_1} O_2^+ + O \tag{1.2}$$

$$O^+ + N_2 \xrightarrow{k_2} NO^+ + N \tag{1.3}$$

   where k_1 and k_2 are charge exchange rates.

2. Dissociative recombination of molecular ions with electrons.

$$O_2^+ + e \longrightarrow O^* + O^* \tag{1.4}$$

$$NO^+ + e \longrightarrow O^* + N \tag{1.5}$$

O^* stands for excited oxygen atoms most of them of which are in metastable states.
It is evident from the above set of reactions that recombination rate (ν_R) of the molecular ions are determined by the charge exchange rates (k_1 and k_2) and the concentrations of O_2 and N_2 ([O_2] and [N_2] respectively). The recombination rate is given by the following equation,

$$\nu_R = k_1[O_2] + k_2[N_2] \tag{1.6}$$

where k_1 and k_2 are functions of thermospheric temperatures [*McFarland et al.*, 1973 and *Anderson and Rusch*, 1980]. Based on recombination rate, the loss rate of ions per unit volume above 200km is given by

$$l = -\nu_R N_e \tag{1.7}$$

where, N_e is electron concentration. Therefore, when the loss of electrons is governed by the charge exchange process, the loss rate is lineary dependent on N_e. However, below 160km, when the loss rate is governed by dissociative recombination process, is given by

$$l = -\alpha N_e^2 \tag{1.8}$$

which means that the loss rate is dependent on the square of N_e. Between 160-200km, so to say, both the loss processes are almost equally operative. It is also interesting to note that as the recombination rate is dependent on molecular concentration, it decreases exponentially with height. Therefore, transport processes associated with drift motions associated with electric field and neutral wind, diffusion dominate in the upper F region.

1.4 Thermospheric airglow radiation

As already mentioned, molecular ions dominate in the lower F region below 160 km and atomic ions dominate above 200 km. These ions recombine with the ambient electrons and on many occasions, metastable atomic excited states are produced during dissociative recombination process. The role of metastable species in the thermosphere has been comprehensively discussed in *Torr and Torr*[1982]. The metastable states have lifetimes much longer than $\sim 10^{-8}$sec which is characteristic for the spectroscopically allowed transitions observed in laboratory. Owing to that reason, these transitions are often referred to as "forbidden" as they violate the selection rules for the electric dipole transition. Depending on the lifetimes of these excited atoms and the ambient collisions, the excited states, thus produced, get de-excited by emitting photons (or get quenched through collisions). Recombination can be radiative as well. These emissions are collectively referred to as "airglow". Thermospheric airglow emissions from different altitude bands can reveal the interactions between the thermosphere and ionosphere as these emissions are dependent on many thermospheric and ionospheric parameters. Different neutral and electrodynamical processes also can be investigated using suitable airglow emission line. Among the commonly used thermospheric airglow emissions are the oxygen airglow emissions at 630.0 nm, 777.4 nm, 135.6 nm etc. In the present work, thermospheric emission lines at 630.0 nm and 777.4 nm are used. Metastable states of neutral oxygen atoms are responsible for the thermospheric airglow emission at 630.0 nm (Figure 1.2). On the other hand, radiative recombination of O^+ ions with ionospheric electrons produces 777.4 nm airglow radiation. Airglow emission intensity is generally expressed in the unit of Rayleigh (1 Rayleigh = 10^6 photons $cm^{-2}s^{-1}ster^{-1}$). Contributions in the night sky brightness by terrestrial airglow emissions are worked out by *Priedhorsky* [1996]. It is also important to note that in absence of atmospheric extinction, a thin homogenously emitting airglow layer at height h above the earth's surface shows a brightness increase as the zenith angle increases, which is given by the so-called Van Rhijn function.

$$\frac{I_\theta}{I_o} = \frac{1}{\sqrt{1 - (\frac{R}{R+h})^2 \sin^2\theta}} \tag{1.9}$$

where θ is zenith angle, R is radius of the earth and I_o and I_θ are the airglow intensities at zenith angles 0 and θ respectively. In other words, the slant columnar airglow intensity is more, in general, than the zenith intensity.

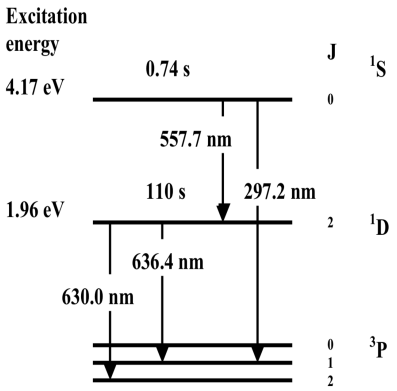

Figure 1.2: Energy level diagram of OI airglow.

1.4.1 OI 630.0 nm and 777.4 nm airglow

OI 630.0 nm airglow emission acts as very good "tracer" for the ITS and as a result, this emission is probably one of the most commonly used emission to probe ITS. During nighttime, the dissociative recombination of molecular oxygen ion with the ambient electrons produces oxygen atom in excited metastable state (^{1}D state, lifetime $\sim$110 sec, energy = 1.96 eV) which subsequently decays giving off 630.0 nm photon emission [e.g. *Peterson*, 1966].

$$O_2^+ + e \longrightarrow O^*(^1D) + O \tag{1.10}$$

$$O^*(^1D) \longrightarrow O(^3P) + h\nu \tag{1.11}$$

It is important to note here that O_2^+ ion, which is produced by the charge exchange between O^+ with O_2, eventually gives rise to 630.0 nm airglow by producing O(^{1}D) state. The rate of the charge exchange reaction depends on the concentration of O_2 molecules which decreases exponentially with height. Therefore, the rate of the charge exchange reaction leading to the formation of O_2^+ decreases with altitude. As a consequence, 630.0 nm emission rate is dependent on the column integral of the product of [O^+] and [O_2]. This factor decides the peak of the 630.0 nm airglow emission layer. 630.0 nm emission intensity ($\sim$50 Rayleigh during nighttime) maximizes at an altitude of $\sim$250km with the semi-thickness of the airglow layer being $\sim$20-30km. *Barbier* [1959] found out an empirical relationship between the instantaneous intensity of OI 630.0 nightglow intensity ($Q_{630.0nm}$) and ionospheric parameters like the peak height of the F2 layer (h_PF_2) and the peak frequency corresponding to the F2 layer (f_oF_2) as follows

$$Q_{630.0nm} = A + B(f_oF_2)^2 \exp^{-\frac{(h_PF_2-200)}{40}} \tag{1.12}$$

where, A and B are constants. $f_oF_2)^2$ is related to electron density (N_mF_2) in the following way

$$N_mF_2 = 1.24 \times 10^{10}(f_oF_2)^2 \tag{1.13}$$

where, f_oF_2 is expressed in MHz and N_mF_2 is expressed in m^{-3}. Therefore, 630.0 nm airglow intensity registers the effects of electric field, winds, waves, composition etc. that can change the height or electron density concentration at the airglow emitting region embedded in ionospheric F layer. However, it is difficult to delineate the signatures of the drivers like electric field, winds, waves etc. in 630.0 nm airglow from one another. This task gets even more complicated when external drivers like the electric field associated with geomagnetic storm affect the low latitude ITS.

Another thermospheric emission that has been used in the present investigation is OI 777.4 nm airglow emission. This emission results from radiative recombination of O^+ with ambient electrons [e.g. *Tinsley*, 1997].

$$O^+ + e \longrightarrow O^*(^5P) \tag{1.14}$$

$$O^*(^5P) \longrightarrow O^*(^5S) + h\nu \tag{1.15}$$

Since the 777.4 nm airglow intensity depends on both O^+ and e, the emission rate is effectively proportional to the column intergral of $[O^+]^2$. In F layer, $[O^+]$ nearly equals plasma density. Therefore, 777.4 nm airglow intensity is believed to depend on the square of the plasma density and not on the F layer height variations [e.g. *Tinsley and Bittencourt*, 1975]. 777.4 nm airglow emission comes from a narrow altitude region centered around the F layer peak. The radiative lifetime of 777.4 nm emission is extremely short ($\sim$tens of nanoseconds)in comparison with 630.0 nm emission and the typical intensity is order of magnitude weaker than 630.0 nm typical nighttime intensity. Using 777.4 nm and 630.0 nm airglow emission, some of the processes pertaining to F region ionosphere over low-equatorial latitudes have been investigated in the present work.

1.5 F region dynamics during daytime: role of E region dynamo

Electric field plays a very important role in the dynamics of F region ionosphere over low-equatorial latitudes. The horizontal orientation of the geomagnetic field over the dip equator is directly or indirectly responsible for the occurrence of several geophysical

processes involving the ionosphere-thermosphere system (ITS) which are characteristic to low-equatorial latitudes. Equatorial Electrojet (EEJ), Counter Electrojet (CEJ), Equatorial Ionization Anomaly (EIA) and Equatorial Spread-F (ESF) are some of the major processes pertaining to the low latitude ITS. The local time dependences of the major ITS phenomena (Figure 1.3) are described in detail by *Abdu* [1997, 2005]. In the above-mentioned processes, EEJ and CEJ occur during daytime, EIA occurs during both day and night and ESF is a nighttime phenomenon. One of the characteristic features of the ionosphere over low-equatorial latitudes is that the ionospheric plasma over dip equator gets redistributed in the low-latitude ionospheric F-region during daytime. This process typically known as the "fountain effect" [*Appleton*, 1946] is primarily initiated by the E-region dynamo mechanism that happens in the equatorial E-region. The ions carried by the tidal winds in the E-region passing across the geomagnetic field (whose strength is denoted by B) lines mimics a dynamo action. The ions move with the neutral wind owing to their larger collision frequency in comparison with the gyro-frequency whereas the electrons are controlled by magnetic field lines as their gyro-frequency is more than the collision frequency at the dynamo region. Thus solar quiet (S_q) time electric fields ($\mathbf{E_{sq}}$) are generated in the E region of the ionosphere. These electric fields are mapped to the F region of the ionosphere through the geomagnetic field lines [*Farley*, 1959, 1960]. Recent satellite investigations experimentally reveal the role of tides in the longitudinal variation of F region electric fields globally [e.g. *Immel et al.*, 2006]. Under the influnece of this mapped electric field, a vertical $\mathbf{E} \times \mathbf{B}$ drift (in the Hall direction) of the plasma over the dip equator [*Hanson and Moffett*, 1966; *Sterling et al.*, 1969; *Anderson*, 1973a, 1973b; *Anderson et al.*, 2002] occurs which is followed by ambipolar diffusion of plasma along the magnetic field lines. Therefore, the equatorial zonal primary dynamo electric field gives rise to cascading processes that eventually modify the electron distribution at F-region altitudes over low latitudes. The fountain effect generates two enhanced (crests) regions of ionization at $\pm 20^o$ in the magnetic north-south plane with depleted plasma concentrations (trough) over the dip equator. Thus, the fountain effect explains the otherwise anomalous distribution of charged particles over the equator, which is termed as the Equatorial Ionization Anomaly (EIA). The zonal electric field (due to global scale dynamo action), which is responsible for EIA, also causes an intense band of current in the E-region of the equatorial ionosphere known as the equatorial electrojet (EEJ). This

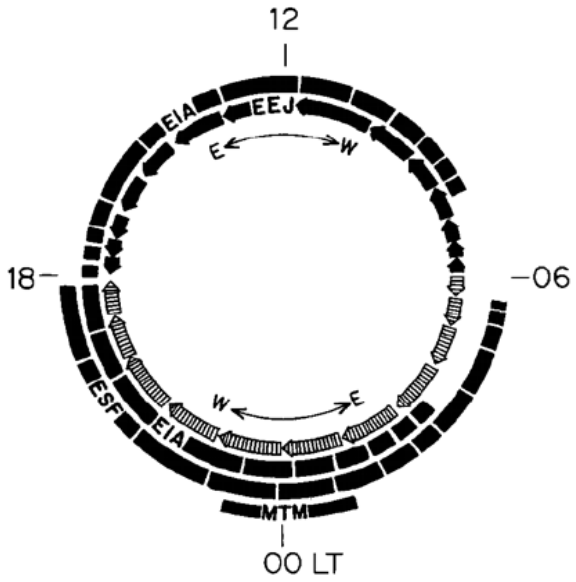

Figure 1.3: Local time dependence of major ITS phenomena (from *Abdu*, 1997).

happens because the motion of the electrons is governed by the strength of the geomagnetic field and thus responds to $\mathbf{E} \times \mathbf{B}$ drift while the ions move with neutrals under the influence of collisions resulting in charge separation and thus a vertical polarization field develops. This polarization field drives the electrons to move westward causing the intense jet of current. Due to the mutually perpendicular geometry of $\mathbf{E_{sq}}$ and $\mathbf{B}$, this effect is most pronounced in a narrow latitudinal belt ($\pm 3^o$) and at a narrow height region (10 km) centered around 106 km. EEJ generally shows a diurnal pattern with peak amplitudes at local noon. However, on certain occasions, even during geomagnetically quiet periods, for reasons still being debated [*Raghavarao and Anandarao*, 1980; *Somayajulu et al.*, 1993; *Stening et al.*, 1996; *Gurubaran*, 2002], the zonal electric field changes its direction from eastward to westward during daytime [*Gouin and Mayaud*, 1967], which is known as the Counter Electrojet (CEJ). Earlier investigations [*Raghavarao et al.*, 1978] revealed that the strength of the EIA has a high degree of correlation (correlation coefficient closer to unity), with the time integrated EEJ strength obtained from ground-based magnetic data. It is also suggested based on ionosonde [*Raghavarao et al.*, 1988] and dayglow observations [*Sridharan et al.*, 1994] that the stronger the EIA, more probable is the occurrence of ESF during nighttime in the equatorial ionosphere.

1.6 F region dynamics during nighttime: role of F region dynamo

During nighttime, zonal thermospheric wind in the ionospheric F region passes across the field lines resembling a dynamo mechanism. This is known as F region dynamo [*Rishbeth*, 1971]. This happens during daytime also. However, the integrated E region Pedersen conductivity is more than the magnetic field line integrated F region conductivity during daytime. As a consequence, the polarization electric fields (essentially in the vertical direction) arising out of the F region dynamo mechanism are largely short-circuited by integrated E region conductivity during daytime. Owing to reduced conductivity of the E region during post-sunset hours and curl-free condition of the ionospheric electric field, the polarization electric field in the zonal direction arises at the sunset terminator on most of the occasions, causing the post-sunset height rise of the F region (see Figures 1.4 and 1.5). Thus the eastward electric field in the equatorial F region reveals a significant enhancement in the post-sunset period before it reverses to the westward direction. This is generally known as pre-reversal enhancement (PRE). The ionization in the equatorial E region, in the post-sunset hours, gets rapidly depleted due to the fast recombination processes (smaller life times) whereas the ionization in the F region is maintained by the dynamical processes. Steep plasma density gradient is, thus, generated in the bottomside F region in the post-sunset hours. This is analogous to an unstable configuration wherein a heavier fluid is supported by lighter fluid. When the plasma density gradient is anti-parallel to gravity, this type of plasma density configuration gives rise Rayleigh-Taylor (RT) instability (see Figure 1.6) under suitable conditions. Under favourable circumstances, this primary instability process grows non-linearly and generates plasma irregularities that sometimes convect to the topside of the ionosphere also. During this time, backscattered echoes from the F region heights manifest as a spread in the range or frequency or both on ionograms which is commonly known as Spread-F. Such events over the equatorial-low latitude regions are generally termed as Equatorial Spread F (ESF). Equatorial Spread F (ESF) is a term coined in the initial years to indicate the spread in the return echoes received by ionosonde when plasma irregularities are present in the ionosphere. This terminology is still continued although many aspects of ESF are understood based on the observations by different techniques. As the scale size of these plasma irregularities range from several hundreds of kilometers to a few centimeters, one

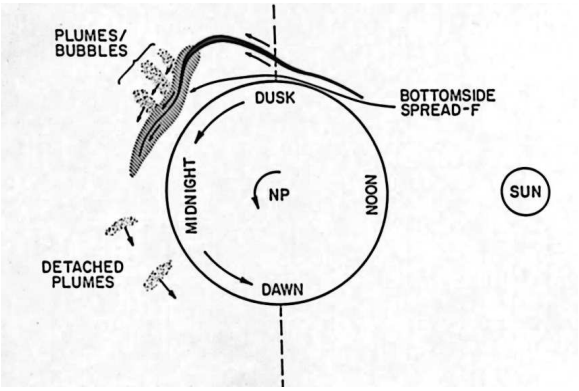

Figure 1.4: Pictorial representation of some of the basic features of ESF like the post-sunset rise of the bottomside F layer, plume structures overlying the bottomside structure and the detached plumes (at non-evolutionary phases) in the midnight-dawn sector termed as “fossil bubbles”(from *Argo and Kelley*, 1986).

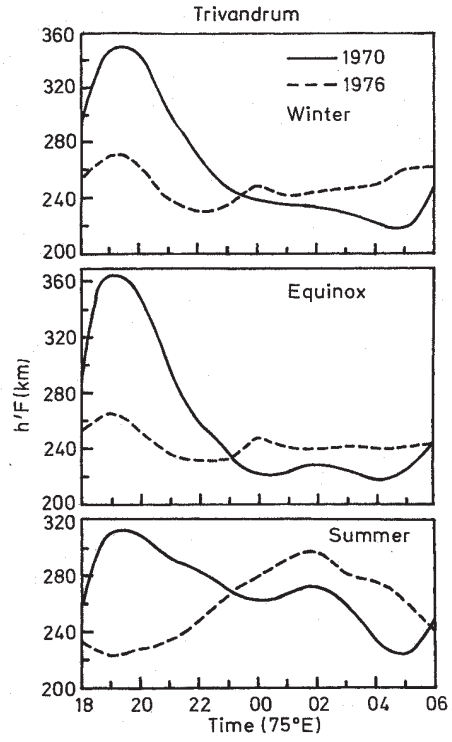

Figure 1.5: Nocturnal variations of h’F at Trivandrum, a dip equatorial station, for each season in sunspot maximum (1970) and minimum (1976) years revealing the variability in pre-reversal enhancement (from *Subbarao and Krishnamurthy*, 1994)

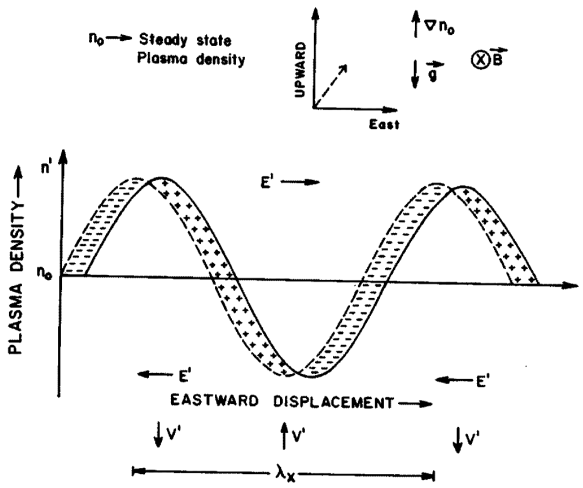

Figure 1.6: Schematic of how Rayleigh-Taylor instability mechanism gives rise to ESF. In the presence of sharp boundary, upward plasma density gradient, downward gravity and horizontal magnetic field line configuration over dip equator, sinusoidal perturbations in the ion and electron densities (n') over the steady state value n_o along the zonal direction results in the generation of differential drifts of ions (drift velocity: g/ν_i) and electrons (drift velocity: g/ν_e) as ions move eastward and electrons move westward under the action of gravity. Polarization electric field (E') gets generated owing to the regions of excess ions and electrons. E' is eastward in the trough region and westward in the crest region that facilitates upward and downward drifts in the trough and crest regions respectively that facilitates further growth of the perturbation amplitude (from *Sekar*, 1990).

requires a variety of probing radio frequencies to study the behavior of different scale sizes. For example, a VHF radar operating at 53 MHz will be able to probe $\sim$3 m scale size plasma irregularities in the F region.

The large scale size (a few hundreds of kilometers) plasma irregularities associated with ESF are now understood to be generated owing to the generalized Rayleigh-Taylor (GRT) instability process involving gravity, electric field, zonal winds in presence of tilted ionosphere, and vertical winds [e.g. see *Sekar and Kelley*, 1998 and references therein]. On the other hand, the plasma plumes arise during the non-linear evolution phase of ESF development. Based on non-linear numerical simulation investigation, it was indicated [*Sekar et al.*, 2001] that more than one wavelength as seed perturbation is required to facilitate the development of plasma enhancement structure during the non-linear evolution phase. Based on that simulation, the presence of plasma enhancement structures moving downward during the evolutionary phase of ESF was predicted. Although the degree of plasma enhancement during ESF events is order of magnitude less than the degree of depletion, it was realized that a suitably sensitive observational technique might be able

to unambiguously identify the presence of plasma enhancement structures. ESF events come with enormous structural variabilities and establishing their relationships with various geophysical processes is the need of the hour. Different variabilities of ESF have been investigated during several decades in the past. Although many aspects of ESF have been reasonably explained based on the theoretical investigations, day-to-day and storm time variabilities of ESF need more attention. Occurrence variability of storm-time, pre-midnight plasma plume associated with ESF is addressed in the present work.

1.7 Space weather disturbances: solar flare and coronal mass ejection

Enormous night-to-night variabilities are observed in the F region processes over low latitudes during even quiet periods. During space weather events, the phenomena pertaining to low-equatorial latitudes deviate from quiet time patterns. Since space weather events are highly variable in space and time, day-to-day variations in the responses of ITS corresponding to different events may also be different. As already recognized, the components of space weather are the sun itself, the solar wind, magnetosphere, ionosphere and terrestrial thermosphere. It is, so to say, that the sun, being the nearest star to earth, drives the space weather of the earth. The solar disturbances come mainly in the form of solar flares and coronal mass ejections (CME). A solar flare is a violent explosion in the Sun's atmosphere. Most flares occur around sunspots, the intense magnetic hotspots on the solar surface. Solar flares may take several hours or even days to build up, but most flares sustain only for a few minutes although long duration flares lasting for a few hours are also observed [e.g. *Phillips et al.*, 2005]. Flares are classified on the basis of the area at the time of maximum brightness in H alpha (656.2 nm). Conventionally, H-alpha flares are divided into 5 classes called "importance". They are denoted by S, 1, 2, 3, and 4. The S class represents faint events called subflares. A brightness qualifier F, N, or B is generally appended to the importance character to indicate faint, normal, or brilliant (for example, 2B) flares. Solar flares are also classified as A, B, C, M or X according to the peak flux (in $\mathrm{W/m^2}$) of 100 to 800 pm (picometer) X-rays near Earth. Each class has a peak flux ten times greater than the preceding one, with X class flares having a peak flux of order 10^{-4} $\mathrm{W/m^2}$. For a given class, the flares are classified based on a linear scale from 1 to 9. Therefore, a X2 flare is twice as powerful as an X1 flare, and is four times

more powerful than an M5 flare. Several investigations reveal the solar flare affects on the terrestrial ITS. Thermospheric densities over low and middle latitudes have been found to even increase $\sim 50\%$ or more in response to X17 class flares [*Sutton et al.*, 2006 and references cited therein]. It is also found that the peak thermospheric response occurred more than an hour after the peak EUV flux emitted by the flare and time taken by the thermosphere to revert back to the pre-flare level was of the order of 12 hours. Ionsopheric electron densities also increase in response to flares [*Tsurutani et al.*, 2005 and references cited therein]. The total electron content (TECU; 1 TECU = 1.0 $\times$ 10^{12} electrons/cm^2) corresponding to a X17 class flare was found to be $\sim$25 TECU which was $\sim$30% above the background level. This ionospheric condition gradually comes back to quiescent level in $\sim$3 hours which was far longer than the flare duration. The above solar flare events are extreme events. Depending on the strengths of the flares, the degree of perturbation on ITS is expected to vary from case to case.

A CME, on the otherhand, is an ejection of plasma material from the solar corona. CMEs are propelled outward at speeds ranging from $<$ 50 to $\sim$2000 km/s. The degree of perturbation the CMEs can bring to the Earth's magnetosphere depends, in general, on the speed of the CME, the strength and polarity of their magnetic fields. CMEs are often preceded by a shock front because they travel faster than the characteristic sound speed of the interplanetary medium. When the shock reaches Earth, a magnetic storm may result. CMEs are also generally associated with solar flares and prominence eruptions but they can also occur in the absence of either of these processes. The association between a solar flare and CME is not clear and being investigated in recent times [e.g. *Kahler*, 1992; *Gosling*, 1993; *Reames*, 2002]. Recent studies [e.g.*Srivastava and Venkatakrishnan*, 2002; *Iyer et al.*, 2006; *Koskinen and Huttunen*, 2006] elicit a close relationship between CME and geomagnetic storm. The 6th January, 1997 CME event [e.g. *Fox et al.*, 1998] had been studied in a comprehensive way from the sun to the ITS and several aspects of CME and its effects on geo-space environment were obtained.

1.8 Impacts of geomagnetic storm on ITS over low-equatorial latitudes

Solar wind originates from the solar coronal holes. Coronal holes are regions of abnormally low density and magnetic field has a single polarity there. This is equivalent to an

open magnetic field configuration, the magnetic field lines being divergent from the sun without curling back to the solar surface. Coronal holes are the sources of fast solar wind streams. With assistances from the open magnetic field configurations and the huge pressure difference that exists between the solar corona and interstellar space, solar plasma is forced to eject outward, despite the enormous backward pull by the solar gravity. Solar wind contains ionized solar plasma comprising predominantly H^+ with He^{++} in small amount. Other compositional ingredients (like ions of heavier elements) are generally found in trace amounts. Solar wind is generally a low-beta (ratio of thermal to magnetic pressure) plasma. However, regions of high-beta in solar wind are not uncommon [e.g. *Mullan and Smith*, 2006]. Solar wind plasma carries a weak magnetic field (a few nT) which is a remnant of the solar magnetic field. Since solar wind is extremely tenuous (5-20 particles/cm^{-3}), it is a collisionless plasma. Electrical conductivity, therefore, is very high. As a consequence, the magnetic field (generally termed as interplanetary magnetic field, IMF) is "frozen in" the solar wind plasma. Typical solar wind velocities are of the order of 400 km/s whereas, the characteristic sound speed at 1 astronomical unit distance (1.5×10^5 km from the sun's center, the earth's orbit being approximately 1AU away), is $\sim$ 60 km/s. Therefore, solar wind is highly supersonic with Mach-number (the ratio of the object velocity to the characteristic acoustic velocity) reaching to 8-10 on many occasions. Although, solar wind comes out radially from the solar surface, the 27 day solar rotation converts this outward flow into spiral form analogous to the working of a garden hose. As the solar wind propagates, the magnetic field is stretched and a configuration similar to the undulations seen in the skirt of a pirouetting ballerina is expected. Hence this concept is famously known as Ballerina model [*Parker*, 1958]. One of the most important earlier discoveries was that the existence of alternate inward (toward the sun) and outward (away from the sun) sectors present in the IMF on most of the occasions. These ingoing and outgoing sectors have magnetic field directions antiparallel to each other and therefore, according to Maxwell's equation

$$\nabla \times \mathbf{B} = \mu_o \mathbf{J} \tag{1.16}$$

current sheets will be formed at the transition regions. In the vicinity of earth, the magnetic field sectors in the IMF will be inward or outward depending upon whether the earth's orbital plane is above or below the current sheets. Another very important consequence of this geometry is that the inclination of the ecliptic plane (the plane consisting of the sun and the earth) with respect to the current sheet gives rise to northward or south-

ward component of the IMF relative to the an axis normal to the ecliptic plane.

The classical condition for a geomagnetic storm onset is the southward turning of the Z-component of interplanetary magnetic field (IMF B_z). This generates a two-cell plasma convection pattern at high latitude ionosphere. During the northward turning of IMF B_z, dayside reconnection occurs at a higher latitude and a complex, multiple convection cells are generated (see Figure 1.7). In both the cases, the potential drop across the polar cap changes that gets mapped in the nightside magnetosphere through the highly conducting field lines. This generates plasma convection towards the earth in the nightside. This plasma motion under the action of gradient and curvature drifts eventually forms the ring current [see *Daglis and Thorne*, 1999; *Daglis*, 2006]. Ring current is driven by the pressure gradient forces in the plasma and to the first order, flows in closed loops around the earth. Current also flows across the tail in the outer magnetosphere which is called tail current. Divergences in the ring and tail current are responded with the generation of field aligned currents (FAC) that connects auroral ionosphere with the inner and outer magnetosphere. The portion of the ring current that closes through auroral ionosphere generally in the dusk-midnight sector is called partial ring current. During substorms, a portion of the tail current is found to collapse and the tail current is diverted to the auroral ionosphere. This portion of the tail current is known substorm current wedge. The ionospheric portions of these current systems are auroral electrojets (eastward in the dusk side, westward in the dawn side) and they flow in the highly conducting channels in the auroral ionosphere. Region 1 field-aligned current (R1 FAC) connects the boundary layer plasma near the magnetopause with the poleward portion of the auroral oval whereas region 2 field-aligned current (R2 FAC) links the inner edge of the ring current with the auroral oval near its equatorward edge (Figure 1.8). The Y component of IMF (IMF B_y) imparts an additional modulation to the convection patterns that get generated corresponding to the south and northward turning of IMF B_z (see Figure 1.7).

The relationship between storm and substorm is not fully clear and is being debated in recent times [e.g.*Kamide et al.*, 1998 and references cited therein]. The characteristic signature of a geomagnetic storm reflects in the depression of the horizontal (H) component of the geomagnetic field which lasts tens of hours in general. Over the equatorial belt, the strength of the magnetospheric ring current (at a distance of $\sim$ 4-6 R_E) increases resulting in the depression in H component. Ring current strengths are monitored by the Dst index (or by the high resolution SYM-H index) which is constructed based on H variations obtained from low latitude stations away from equatorial electrojet region. On the

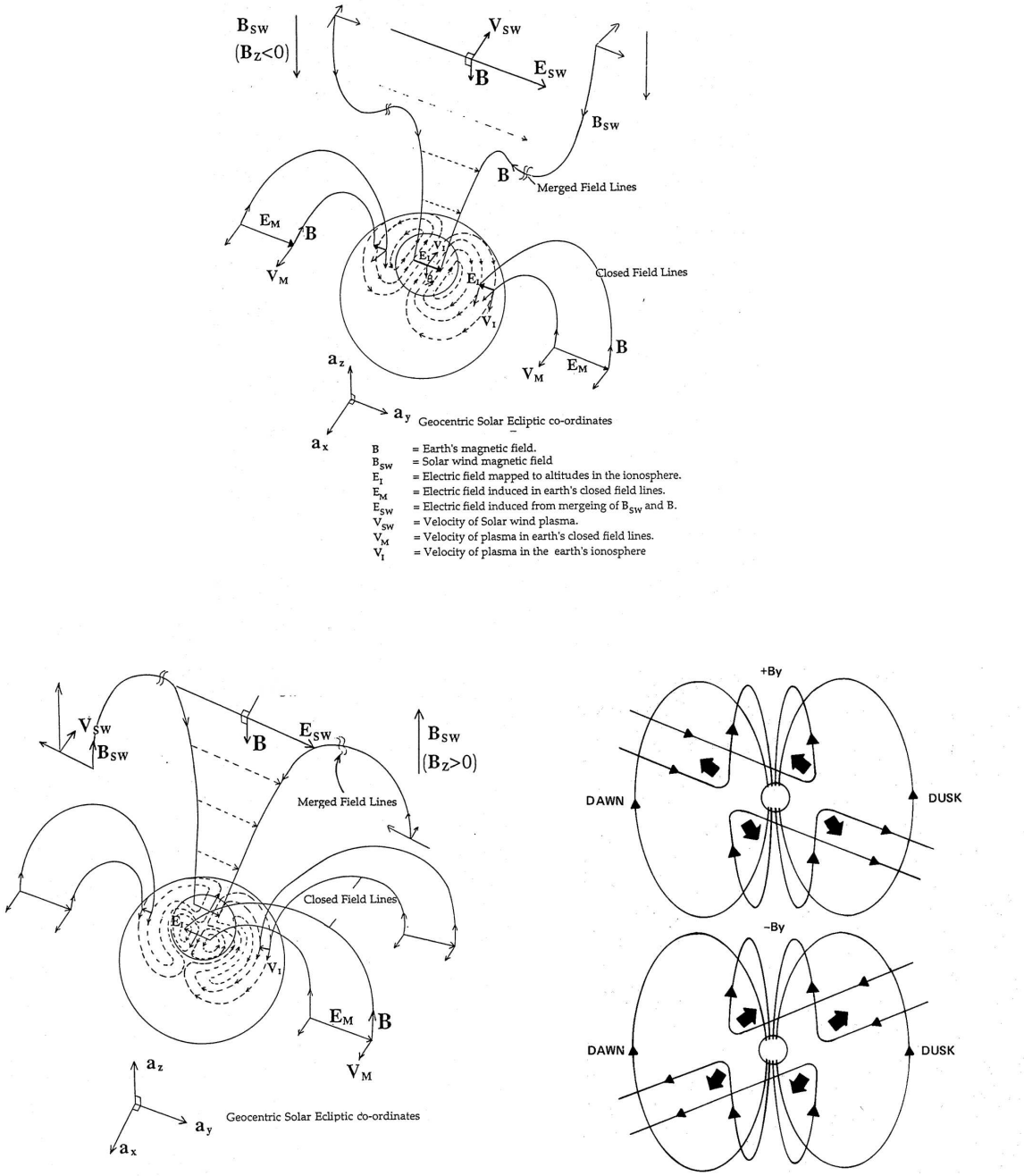

Figure 1.7: Magnetic connection between the solar wind dynamo and the ionospheric load: (top) Idealized two cell convection pattern for southward IMF B_z or IMF $B_z < 0$, (bottom left) idealized four cell convection pattern for IMF $B_z > 0$ (from *Reinisch*, 1996), and (bottom right) additional effects of IMF B_y (from *Kivelson and Russell*, 1995).

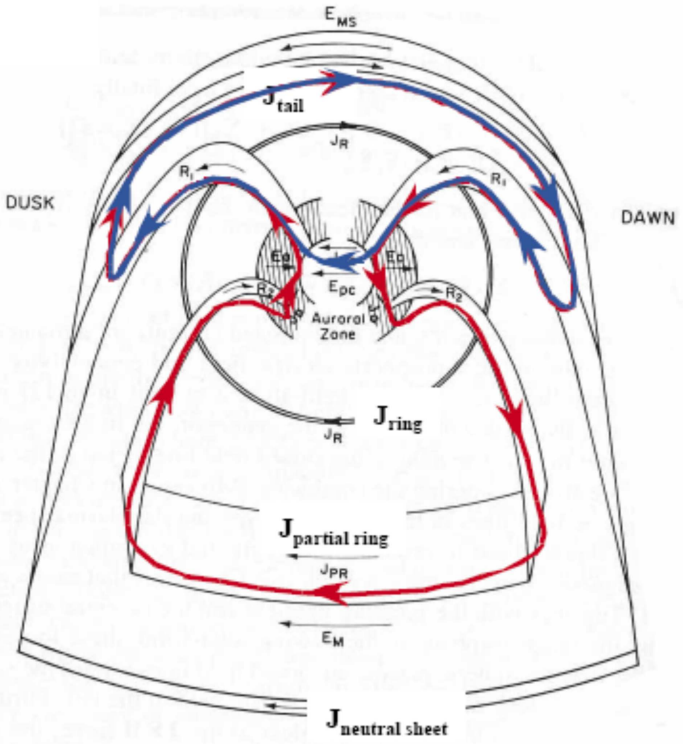

Figure 1.8: Region 1 (R1) and region 2 (R2) field aligned current (FAC) systems. R1 FAC connects the poleward portion of the auroral oval and the polar cap to the magnetosheath, solar wind, or the boundary layer plasma near the magnetopause. R2 FAC, on the other hand, links the inner magnetosphere with the auroral oval near the equatorward edge (based on *Kelley*, 1989).

other hand, one of the characteristic features of substorms is the increase in the auroral electrojet current system. A representative index corresponding to the auroral electrojet strength is the AE index. There are other global storm indices like the K_p and A_p, based on magnetometer measurements, which are available to characterize quiet/storm events [e.g. see *Mayaud*, 1980]. K_p and A_p indices are based on geomagnetic observations made at twelve observatories around the globe. K_p index is obtained by combining K index (ranges from 0 to 9) related to the amplitude of geomagnetic field variation. Accuracy of K_p index is $\frac{1}{3}$ of a unit. K_p index is expressed on a quasi-logarithmic scale. Typically, K = 9 indicates a geomagnetic storm with magnetic disturbances of $\sim$ 300, 500 and 2000 nT over low, mid and high latitudes respectively. A_p index, on the other hand, is computed based on the horizontal (H), vertical (Z) and dip (D) components of magnetic field recorded every three hour. The largest of the three deviations is called amplitude (a). After removing the solar quiet day (S_q) and lunar variations, the amplitude 'a' for twelve observatories are averaged to derive the index A_p.

Before the onset of a storm, the supersonic (Mach number sometimes reaches 7-8),

collisionless solar wind plasma with the frozen-in magnetic field hits the earth. The magnetic field of the earth obstructs the supersonically moving solar wind and a bow shock is generated. Shock waves are normally generated in a collision-dominated medium. However, in solar wind plasma, the frozen-in magnetic field generates fluid-like conditions giving rise to collisionless shocks. At the magnetosheath region, solar wind slows down and the velocity, in principle, becomes zero at the terrestrial magnetopause where the solar wind ram pressure equals the magnetic pressure exerted by the geomagnetic field. The compression of the magnetopause by the solar wind (and associated increase in the current strength flowing in the magnetopause known as Chapman-Ferraro current) reflects in the sudden positive increase in the H components measured by the ground magnetometers at low latitudes and is called the storm sudden commencement (SSC) phase of a storm. The SSC phase is followed by almost constant and elevated H value that persists for sometime which is referred to as the initial phase. Afterward, the H values decrease indicating the main phase of the storm. Recovery phase follows the main phase when the H values over a period of several hours or a few days return back to the pre-storm level. During geomagnetic storm, solar wind energetic particle gets directly precipitated in the auroral region through the polar cusp. Auroral electrojet current subsequently increases and dissipates as Joule heating which results in the generation of atmospheric gravity waves (AGW). These AGWs propagate towards equator and redistribute the additional energy and momentum globally. Comprehensive reviews [e.g *Hocke and Schlegel*, 1996 and references therein] are available in the literature on the critical aspects of these gravity waves. In addition to that, compositional changes occur in the global thermosphere [e.g.*Prolss*, 1982] which bring forth the positive and negative ionospheric storms by changing the O/N_2 ratio globally. The heat content of the polar thermosphere increases. This additional heat gets redistributed globally and the thermospheric temperatures even in the low latitude regions [e.g. *Biondi and Meriwether*, 1985] are found to register enhancements with a time delay. The meridional wind circulation changes both in magnitude and direction following a storm. Therefore, the meridional wind flows from the equator to polar region during daytime. The reverse happens during nighttime. These quiet time patterns change drastically following geomagnetic storms when the disturbed meridional winds flow from the poles to the equatorial region. Different aspects of geomagnetic storm on terrestrial ITS is comprehensively reviewed by *Buonsanto* [1999].

1.9 Disturbance Dynamo

As discussed in the previous section, auroral heating over high latitude during geomagnetic storms change the wind patterns globally. Hadley type of circulation cells are generated and wind starts flowing towards equator above $\sim$120 km. Under the action of Coriolis force, a westward momentum is imparted to this equatorward circulation at mid-latitudes.

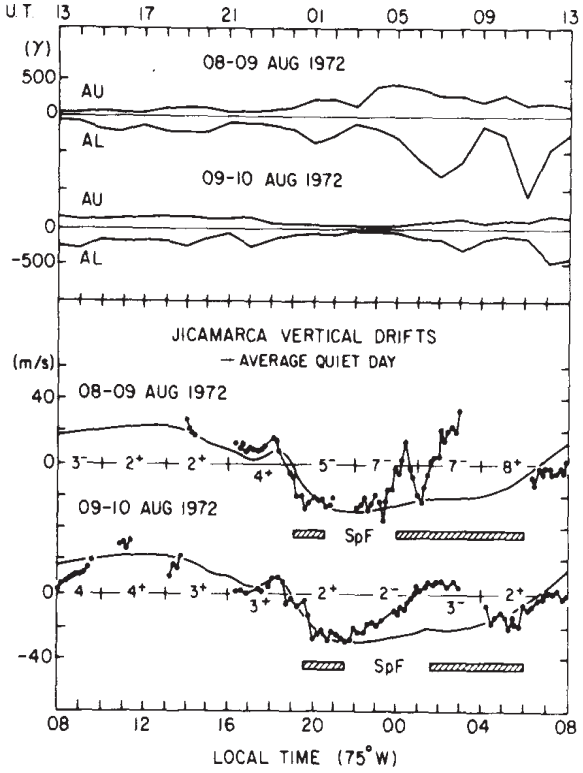

Figure 1.9: Signatures of prompt penetration and disturbance dynamo effects on vertical drifts over dip equator (from *Fejer et al.*, 1983).

The westward winds, in turn, generates a poleward electric field, westward E $\times$ B drift, and an eastward current. The eastward current at mid-latitude, depending upon the strength of the wind and the global conductivity variations, closes partly in the lower latitudes. This eastward current, thus, opposes the "quiet day" S_q current system at low-equatorial latitudes. Therefore, the low latitude currents, electric fields and drift patterns deviate from the "quiet day" patterns. This is known as disturbance dynamo effect [*Blanc and Richmond*, 1980]. Owing to its association with thermospheric wind circulation, disturbance dynamo is a delayed effect. Many a times, the observed features of electric fields and currents over low-equatorial latitudes are found to deviate from the "quiet day" patterns (see Figure 1.9) during the recovery phase of a geomagnetic storm which can not be explained on the basis of the direct effects of magnetospheric electric field on the low lati-

tude ionosphere. Considering the disturbance dynamo effect, these features are addressed [e.g. *Kane* 1973a, b; *Sastri*, 1988; *Scherliess and Fejer*, 1997; *Abdu et al.*, 1997; *Emmert et al.*, 2001; *Fejer and Emmert*, 2003; *Le Huy and Mazaudier*, 2005]. The effects of disturbance dynamo on the electric fields and currents over low latitudes are always difficult to decipher from ionospheric observations as both the disturbance dynamo effect and storm-time direct penetration of magnetospheric electric field plays role in the restructuring ITS over low-equatorial latitudes during storm-time [*Maruyama et al.*, 2005]. In the present work, observations and simulations pertaining to the effects of the direct penetration of magnetospheric electric field on the low latitude ionosphere will be reported. Therefore, the characteristic processes associated with the mechanism of magnetospheric electric field penetrating into the low latitude ionosphere is discussed in the following sections.

1.10 Magnetosphere and plasmasphere

Magnetosphere is the region where geomagnetic field governs the motion of the charge particles. Although, geomagnetic field starts governing the motion of the charge particles at all heights above ∼150 km, the concentration of charged species is more in comparison with neutral species in the magnetosphere. This situation arises from a height of ∼ 1500 km. Magnetosphere ends at magnetopause where the influence of geomagnetic field ends. At magnetopause, the dynamic pressure (= $m_P n_{sw} {V_{sw}}^2$; where m_P, n_{sw}, and V_{sw} are proton mass, density and velocity of solar wind respectively) of the solar wind is equal, in principle, with the static pressure exerted by earth's magnetic field [e.g. *Spreiter et al.*, 1966; *Sibeck et al.*, 1991].

$$k\rho V_{sw}^2 cos^2\theta = \frac{(2fB)^2}{2\mu_o} \tag{1.17}$$

where ρ, θ and B are mass density of solar wind, angle between magnetopause normal and sun-earth line and the magnetic field strength just inside the magnetopause considering a dipole configuration. Constants μ, k and f represent permeability of free space, fraction of solar wind dynamic pressure applied to the magnetosphere, and an enhancement of the magnetic field strength from dipolar values. k ranges from 0.67 to 1.0 and f from 1.0 to 1.5 [e.g. *Schield*, 1969]. ρ is given as follows.

$$\rho = (n_P + 4n_\alpha)M + (n_P + 2n_\alpha)m \tag{1.18}$$

where n_P, n_α, M and m are the proton number density, helium number density, proton mass and electron mass respectively. The ratio $\frac{n_\alpha}{n_P}$ varies from 0.01 to 0.08 [*Robbins et al.*, 1970] and it can be typically taken as 0.037. Contribution of electron in the mass density ρ can be considered negligible. However, helium may contribute significantly. *Kivelson and Russell* [1995] provides a simplified analytical expression for the magnetopause (in the unit of earth's radius, R_E) as follows.

$$L_{mp}(R_E) = 107.4(n_{sw}V_{sw}^2)^{-\frac{1}{6}} \tag{1.19}$$

where n_{sw} is the proton number density which is adjusted for the helium content in the solar wind, and V_{sw} is solar wind velocity in km/s.

Magnetopause lies almost $\sim 10R_E$ (R_E is earth's radius) away on the dayside and at a much greater distance at nightside. Magnetosphere is filled with plasma of solar wind and ionospheric origin. Magnetospheric plasma is governed by the effects of several electric fields of different origin (see Figure 1.10). One of them is co-rotation electric field which arises due to the macroscopic rotation of the upper atmospheric plasma across the geomagnetic field ($\mathbf{V} \times \mathbf{B}$ field). Under the influence of only corotation electric field (directed radially inward towards earth in a non-rotating frame of reference), the ionospheric and magnetospheric plasma will corotate with earth. However, ionospheric plasma corotation is modified by the temperature and pressure gradients created by solar radiation, joule heating by the auroral electrojet current systems, energetic particle precipitation etc. In addition to that, corotation electric field in magnetosphere competes with the electric field generated due to the interaction of solar wind with magnetosphere. Owing to this interaction, a potential difference of the order of tens of volts to hundreds of kilovolts is generated in the dawn-to-dusk direction. This produces sunward plasma convection in the equatorial plane of the magnetosphere. The interplay between corotation and sunward convection electric field (sometimes, referred to as cross-tail electric field also) leads to a boundary region (region of last closed equipotential or LCE) in the earthward side of which the plasma motion is governed by corotation. The region inside this boundary is filled with cold ($<$1 eV) ionospheric plasma (mostly H^+) and is known as plasmasphere. The boundary of plasmasphere is known as plasmapause. In a simplistic corotation-convection model,

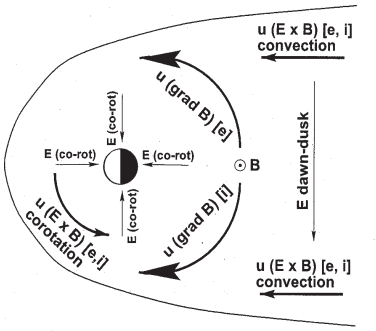

Figure 1.10: Components of particle drift u in the magnetosphere (from *Friedel et al.*, 2001).

corotation and convection electric fields cancel at plasmapause.

$$E_c = \left(\frac{B_o}{L^3}\right) L R_E \omega \tag{1.20}$$

where E_c is the convection electric field, B_o is the magnetic field strength at the Earth'surface over dip equator and ω is the angular rotational velocity of the Earth and R_E is radius of the earth. If plasmapause is typically taken at $4R_E$ away (i.e. $L = 4R_E$), E_c = 1 mV/m. This basic model was proposed soon after the discovery of plasmasphere [e.g. *Nishida*, 1966; *Brice*, 1967, *Carpenter and Park*, 1973]. Across the plasmapause, the plasma density sharply falls by orders of magnitude (e.g. from 10^3 per cc to 1 per cc). Outside plasmapause, the plasmas are mostly hot and of solar wind origin especially during geomagnetically "disturbed" period. Plasma motion (along the open equipotentials) is mostly governed by convection electric field in this region. It is important to note that recent investigations reveal that plasmapause need not coincide with the instantaneous boundary between convection and co-rotation, because time scale for plasmasphere response is slower than time scale of convection variation [e.g. *Burke et al.*, 1998; *Sandel et al.*, 2003; *Burch et al.*, 2004; Burch, 2005; *Goldstein*, 2006; *Wolf et al.*, 2007].

1.11 Magnetosphere-ionosphere coupling: an electric field perspective

Before the impact of IMF in the terrestrial magnetosphere-ionosphere system (MI system) is discussed, there is a need to invoke a proper coordinate system to describe the solar wind from a terrestrial point of view. In the Geocentric Solar Ecliptic (GSE) coordinate system, the X-axis points from the earth towards the sun, Y-axis points towards the dusk and the

Z-axis is positive towards the earth's spin axis (to the north) and parallel to the ecliptic pole. Another coordinate system that is in vogue is Geocentric Solar Magnetospheric (GSM) system. Here X-axis also points from the earth towards the sun. However, the Y-axis is perpendicular to the earth's magnetic dipole and the Z-axis is chosen to be in the direction of the northern magnetic pole. These coordinate systems can be mutually transformed through a rotation about the X-axis. In the present work, GSE coordinate system is used.

The IMF is manifested in the reference frame fixed to earth as an electric field given by

$$\mathbf{E}_{sw} = -\mathbf{V}_{sw} \times \mathbf{B}_{sw} \tag{1.21}$$

E_{sw} is commonly referred to as Interplanetary electric field or IEF. Based on the work of *Sonnerup* [1974], *Burke et al.* [2007], used the following expression for IEF.

$$\mathbf{IEF} = VB_t sin^2\left(\frac{\theta}{2}\right) \tag{1.22}$$

where,

$$B_t = \sqrt{B_y^2 + B_z^2} \tag{1.23}$$

and

$$\theta = cos^{-1}\left(\frac{B_z}{B_t}\right) \tag{1.24}$$

where θ is the IMF clock angle in the Y-Z plane. The electrostatic potential corresponding IEF gets mapped in the polar ionosphere through the highly conducting field lines as the field lines open up at higher latitudes due to merger with IMF. Therefore, the effects of IEF over polar latitudes are direct. Since the field lines are equipotentials, the electric field in the polar cap is mapped to the nightside magnetosphere (or equivalently the voltage drop across the nightside magnetosphere). This increases the $\mathbf{E}\times\mathbf{B}$ plasma convection in the nightside magnetosphere. Therefore, this electric field in the nightside magnetosphere is also referred to as convection electric field. Interestingly, there are occasions when the effects of convection electric field is seen even in the ionosphere over equator and low latitudes almost instantaneously. These events are generally known as prompt penetration (PP) events. Penetration of IEF into low latitude ionosphere has been studied for the past few decades based on geomagnetic field variations, by VHF/HF radar observations,

satellite observations or modeling [e.g. *Nishida*, 1966, 1968a, 1968b; *Rastogi and Patel*, 1975; *Kelley et al.*, 1979, 2003, 2007; *Reddy et al.*, 1979; *Gonzales et al.*, 1979; *Fejer et al.*, 1979, 1998, 2003; *Somayajulu et al.*, 1985; *Earle and Kelley*, 1987; *Spiro et al.*, 1988; *Sastri et al.*, 1992, 2001, 2003; *Kikuchi et al.*, 1996, 2000, 2003; *Abdu et al.*, 1997; *Fejer and Scherliess*, 1998; *Scherliess and Fejer*, 1998; *Peymirat et al.*, 2000; *Goldstein et al.*, 2002; *Ridley and Liemohn*, 2002; *Fok et al.*, 2005; *Huang et al.*, 2005, 2007; *Maruyama et al.*, 2005, *Anghel et al.*, 2007]. PP events are dependent on prevalent coupling between magnetosphere and ionosphere. In order to explain the direct effects of IEF into the ionosphere over dip equator, a shielding mechanism between magnetosphere and ionosphere is generally invoked [*Vasyliunas*, 1970, 1972; *Jaggi and Wolf*, 1973; *Southwood*, 1977; *Senior and Blanc*, 1984; *Wolf*, 1970,1974,2007].

1.11.1 Shielding of Convection electric field: Role of ring current

Since the shielding between magnetosphere and ionosphere occurs at the inner edge of the ring current region, it is necessary to highlight some relevant points pertaining to ring current. Under the influence of cross-tail electric field in the nightside magnetosphere, convection of plasma brings ions and electrons close to earth. Since geomagnetic field strength increases as the plasma reaches closer to earth, a distance is eventually reached when the plasma is stopped from penetrating further and the plasma starts flowing around the earth. However, ions and electrons are deflected in opposite directions by Lorentz forces exerted by earth's magnetic field. Ions take a westward turn and electrons take eastward turn. As a consequence, a westward current is generated. The generation of ring current is constituted by three different motions the time scales of which are sufficiently different so that these motions can be mathematically separated and analyzed with the help of adiabatic invariants. These motions are as follows.

1. **Cyclotron motion:** Gyration around magnetic field lines (Typical time scale: milliseconds to a few seconds).

2. **Bounce motion:** Charge particles bounce back and forth between the mirror points (Typical time scale: a few minutes).

3. **Gradient and curvature drifts:** Drifts perpendicular to magnetic field (Typical time scale: Tens of hours)

   Gradient drift is given by the following expression

$$\mathbf{V}_G = \frac{W_\perp \mathbf{B} \times \nabla B}{qB^3} \tag{1.25}$$

whereas curvature drift is given as follows

$$\mathbf{V}_C = \frac{2W_\parallel \hat{\mathbf{r_c}} \times \mathbf{B}}{qR_C B^2} \tag{1.26}$$

Where $W_\perp$ ($\frac{mv_\perp{}^2}{2}$) and $W_\parallel$ ($\frac{mv_\parallel{}^2}{2}$) are the kinetic energies derived from perpendicular and parallel components of the velocity vector of the charged particles, R_C is the radius of curvature and B is magnetic field strength.

Pitch angle of the particle is defined as

$$\theta = \tan^{-1}\left(\frac{v_\parallel}{v_\perp}\right) \tag{1.27}$$

It is to be noted here that V_G and V_C are in the same direction as $\hat{r_c}$ (positive outward from the center of the earth) and ∇B (negative outward) are in opposite directions in a dipole field.

Adiabatic invariants ($\oint$PdQ where P and Q are the generalized momentum and coordinate) associated with the above mentioned motions of charged particles are the quantities that remain conserved when it is assumed that the changes in the magnetic flux densities are much smaller in comparison with the temporal scales associated with the particle motions. The adiabatic invariants associated with the motions are as follows.

- The first adiabatic invariant is the magnetic moment associated with the cyclotron motion. Magnetic moment remains constant if magnetic field does not change significantly during one gyration period. Mathematically,

$$\mu = \frac{mv_\perp{}^2}{2B} \tag{1.28}$$

where, μ, $v_\perp$ and B are magnetic moment, perpendicular velocity and magnetic field strength respectively.

- The second adiabatic invariant is associated with the bounce motion of the charged particles between mirror points and in this case the integral of the parallel momentum over one bounce between mirror points is conserved if magnetic field does not change significantly during bounce period. Mathematically,

$$J = \oint p_\parallel dl = 2\int_{l_1}^{l_2} mv_\parallel dl \tag{1.29}$$

where, $p_{\|}$ and $v_{\|}$ are the components of parallel momentum and velocity along the magnetic field. l_1 and l_2 are mirror points and dl is the distance covered by the charged particle between the mirror points along the field line.

- The third adiabatic invariant is associated with gradient and curvature drifts. The total geomagnetic flux enclosed by the drift orbit is constant provided magnetic field does not change during the time taken by a particle to encircle the earth. Mathematically,

$$\Phi = \oint v_d r d\psi \tag{1.30}$$

where v_d is the sum of all perpendicular drift velocities, ψ is the azimuthal angle and the integral is taken for one complete drift cycle.

The net effect of the above three motions is a collective azimuthal drift. Electrons move eastward and positively charged ions move westward. The net charge transport associated with this differential responses of ions and electrons produces ring current. The average current density associated with ring current during magnetically quiet period vary from $\sim$ 1-4 nA/m^2 [e.g. *De Michelis et al.*, 1997] whereas during disturbed period, it may exceed even $\sim$ 7 nA/m^2 [e.g. *Lui et al.*, 1987]. The magnetic field disturbance (ΔB) recorded at ground over dip equator during geomagnetic storms is shown [*Dessler and Parker*, 1959; *Sckopke*, 1966] to be associated with the energy of the ring current particles as follows

$$\frac{\Delta B}{B_o} = \frac{2E}{3E_m} \tag{1.31}$$

where B_o is the average geomagnetic field strength recorded at ground over dip equator, E is the total energy associated with ring current particles and E_m ($\sim 10^{18}$J) is the magnetic field energy associated with terrestrial dipole field at the earth's surface [see *Daglis*, 2006]. This is known as Dessler-Parker-Sckopke relation.

1.11.2 Shielding and Alfven layer

At the earthward side of the ring current, the drift trajectories (of constant μ and J) form closed orbits that are not accessible by the plasma sheet particles driven by convection from the magnetotail region whereas open drift trajectories transport plasma from the plasma sheet that eventually drapes around the earth. The boundary between the open and closed drift trajectories is known as Alfven layer (Figure 1.11). With the help of

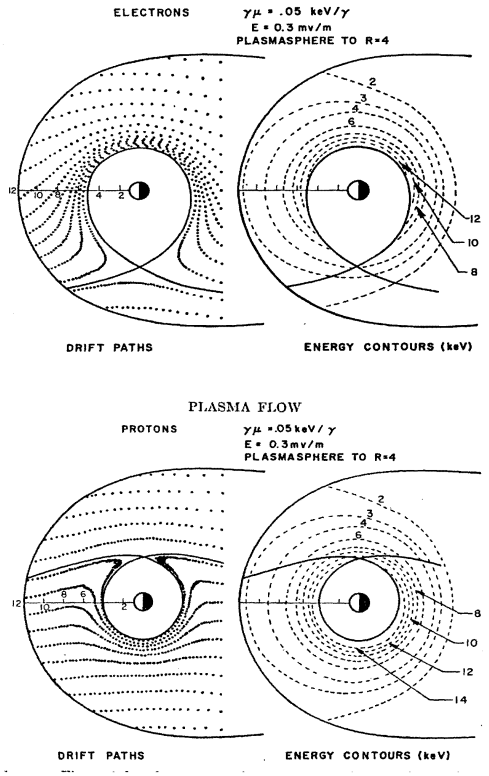

Figure 1.11: Alfven layers for electrons and protons (from *Kavanagh et al.*, 1968).

simple convection-corotation model and taking into account the gradient drift motion, plasmaspheric dynamics during increased convection can be understood analytically [*Kivelson and Russell*, 1995]. Assuming a simple dipole magnetic field configuration, the magnetic field strength at a distance r from the center of the earth can be written as

$$B = \frac{B_o R_E^3}{r^3} \tag{1.32}$$

where B_o is the equatorial magnetic field at the earth's surface ($\sim$31000 nT) and R_E is the radius of the earth ($\sim$6387 km). Now if J = 0 (particles being considered mirror in the equatorial plane), energy of the particles is given by μB. Therefore, considering gradient drift along with convection and corotation, the resultant potential can be written as

$$\phi_{res} = -E_c r sin\psi - B_o \omega \frac{{R_E}^3}{r} + \frac{\mu B_o {R_E}^3}{q r^3} \tag{1.33}$$

where the first, second and the third terms on RHS of the above equation are the convection, corotation and gradient drift terms respectively. ω is the angular velocity of earth's rotation ($\sim$7.43 $\times$ 10^{-5} s^{-1}). ψ is the azimuthal angle which is zero at local noon, $\frac{\pi}{2}$ at local dusk and π at local midnight. Total-drift velocity can now be written in terms of ϕ_{res} as follows.

$$V_d = \frac{B \times \nabla \phi_{res}}{B^2} \tag{1.34}$$

The particles drift along the paths of constant ϕ_{res}. Two cases now can be considered. For cold particles, μ=0. Therefore,

$$\phi_{res}^{cold} = -E_c r sin\psi - B_o \omega \frac{{R_E}^3}{r} \tag{1.35}$$

Several points can be noted here.

- Near earth (as r decreases), corotation term dominates and becomes more and more negative. Electric field points towards the earth. E$\times$B drift is eastward (counter-clockwise).
- At great distances away from earth, convection term dominates and plasma flows towards the sun.
- At intermediate distance, corotation and convection compete with each other for the control of plasma. At the dawnside, corotation and convection get added together (eastward plasma drift) and at the duskside, they try to cancel the effects of each other. One point,thus, in principle, exists in the dusk meridian where flow velocity is zero. If the convection process is not varying temporally, convection-driven plasma cannot cross this boundary (termed as “separatrix”).

Therefore, flow velocity is zero where $\frac{\partial \phi_{res}}{\partial r}$= 0, and $\frac{\partial \phi_{res}}{\partial \phi}$= 0 which gives the coordinate of the point of zero flow as follows.

$$r^2 = \frac{B_o \omega {R_E}^3}{E_c} \tag{1.36}$$

From the above equation, it is implied that plasmasphere is not spherical. It has a bulge on the duskside where plasma flow lines must spread out to reflect the competition between convection and corotation. In times of high geomagnetic activity when convection increases, this simple model also explains the fact that the shape of the plasmasphere changes (in fact, shrinks!). Cold charged particles inside the separatrix go on encircling the earth and form the plasmasphere. Most importantly, for temporally varying convection field, physical plasmapause does not, in general, coincide with the sepratrix (boundary between convection and coroation). Cold plasma has been observed outside plasmapause after an increase in convection [e.g. *Grebowsky*, 1970].

For energetic particles, however, gradient-drift term dominates over corotation term. And the resultant potential is given by,

$$\phi_{res}^{hot} = -E_c r sin\psi + \frac{\mu B_o {R_E}^3}{q r^3} \tag{1.37}$$

Based on the above equation, it can be inferred that ϕ_{res}^{hot} is governed by the gradient drift term near the earth. For positively charged particles, ϕ_{res}^{hot} is large and positive close to earth. Therefore, they drift westward (in the direction of B $\times\nabla\phi_{res}$). Negatively charged particles, on the other hand, drift eastward. At large distances away from the earth, both forms of charged particles convect towards the sun. It is to be noted that, electrons from plasma sheet penetrate closer to the earth on the dawnside than the positive ions. Ions, on the contrary, penetrate closer on the dusk side. For hot particles, coordinate of the point of zero flow is given as follows.

$$r^2 = \left(\frac{3\mu B_o {R_E}^3}{|q|E_c}\right)^{\frac{1}{2}} \tag{1.38}$$

Therefore, as the convection electric field increases, r decreases. Particles reach closer to earth. However, size of the trapped particle region is larger for more energetic (higher μ) particles. Although this simple model can explain many features of plasmaspheric dynamics, it is unable to completely describe several aspects of magnetosphere-ionosphere coupling. One of those coupling aspects is the penetration of magnetospheric convection field into the ionosphere over low-equatorial latitudes during periods of rapid changes despite the so-called shielding between magnetosphere and ionosphere.

1.11.3 Shielding : Undershielding (Prompt penetration) and overshielding

As already stated, based on a simple convection-corotation model, the convection electric field and the corotation electric field must cancel each other at plasmapause. The analytical expression for the potential distribution can then be reached at as follows.

$$\phi_{res}^{cold} = -E_c r sin\psi - B_o\omega\frac{{R_E}^3}{r} \tag{1.39}$$

where r is the radial distance from the center of the earth. The first term on RHS of the above equation is the convection term and the second term is the corotation term. Note that the convection term consists of convection electric field that does not change with time.

This simple convection-corotation model is modified to introduce the concept of shielding of magnetospheric electric field at plasmapause by *Volland* [1973] and *Stern* [1975]. Based on Stern-Volland model, the electric potential configuration can be written as

$$\phi_{res}^{cold} = -br^{\gamma} sin\psi - \frac{a}{r} \tag{1.40}$$

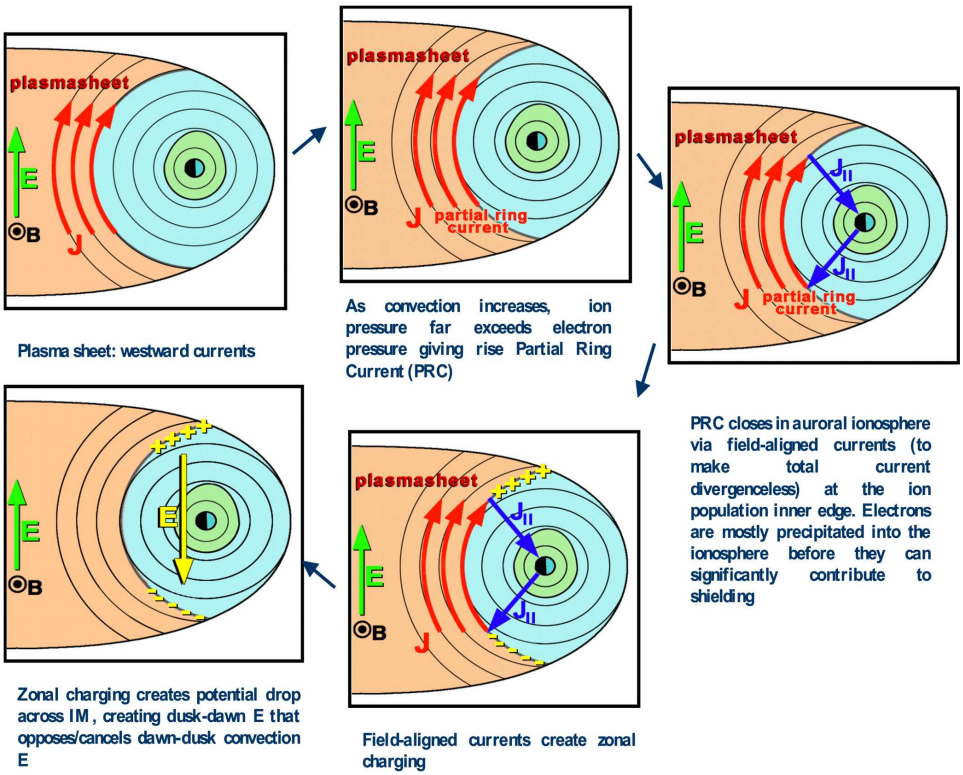

Figure 1.12: Sequence of schematic diagrams showing the generation of shielding electric field at the inner edge of ring current (based on *Goldstein* , 2002web).

where r is the distance from the center of the earth, ψ is the magnetic local time referred to from noon, γ is the shielding factor, and a is the corotation constant given by

$$a = 92.4 \ (kV {R_E}^{-1}) \tag{1.41}$$

The convection term b can be parameterized with the help of K_P index. Based on *Maynard and Chen* [1975], the expression of b can be obtained for γ = 2 as follows,

$$b = \frac{0.045}{(1 - 0.159K_P + 0.0093{K_P}^2)^3} \tag{1.42}$$

b is expressed in the units of $kVR_E{}^{-2}$. b is often determined empirically, although it can be derived based on cross polar cap potential observations [*Goldstein*, 2005]. For γ = 1, the potential distribution patterns based on Stern-Volland model reduces to form similar to that given by simple corotation-convection model. Stern-Volland model, though successful sometimes in reproducing plasmasphere evolution when it is parameterized with time by considering the time variation of K_P index, it is unable to reproduce plasmaspheric structures often and other sources of electric fields need to invoked [e.g. *Goldstein*, 2003]. Recently, *Burke* [2007] tested the efficacy of Stern-Volland model to predict the penetration electric field based on Advanced Composition Explorer (ACE) satellite observations. Self consistent models like Rice Convection Model (RCM) is able to handle

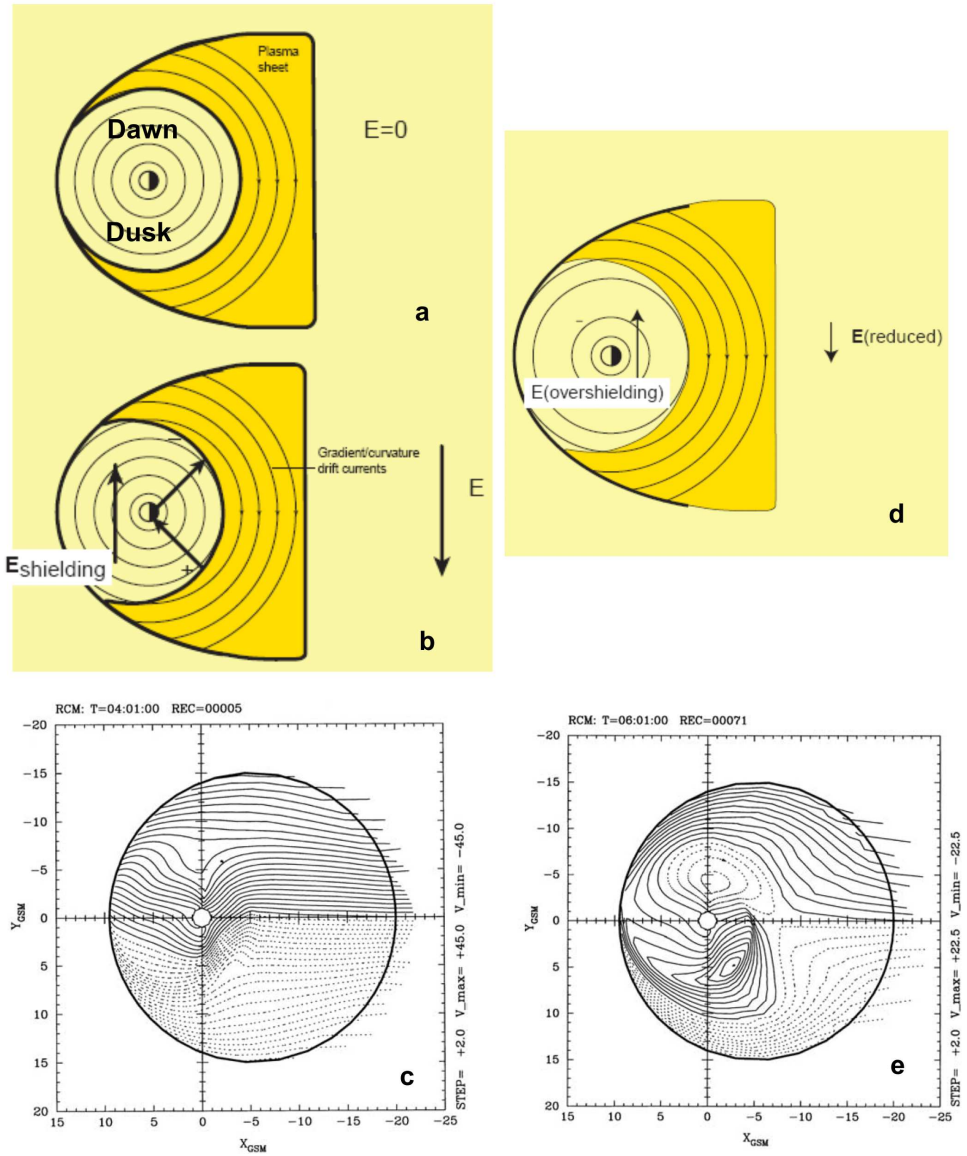

Figure 1.13: (a) Equilibrium condition no convection, with plasma-sheet edge aligned with contours of constant potential, (b) rapid increase of convection electric field and the associated shielding electric field, (c) equatorial plot of RCM computed equipotentials shortly after an increase in the solar wind electric field, (d) sudden decrease of convection electric field and the associated overshielding electric field, and (e) equatorial plot of RCM computed equipotentials revealing the characteristic pattern of overshielding electric fields (based on *Goldstein* , 2002 and *Toffoletto et al.*, 2003).

the discrepancies of Stern-Volland model to a great extent [e.g.*Toffoletto et al.*, 2003]. RCM can reproduce shielding as well as other electric fields quite efficiently. In general, when the convection increases during times of active geomagnetic conditions, ion pressure exceeds the electron pressure (enhanced pressure gradient) at L = 3-4 R_E. This gives rise to partial ring current (PRC). In order to make the total current divergenceless, PRC gets connected with the auroral ionosphere through region 2 field aligned currents (R2

FAC) flowing between magnetosphere and ionosphere and subsequently gets closed by the perpendicular ohmic currents in auroral ionosphere. R2 FAC currents, in turn, change the potential distribution inside the ionosphere and inner magnetosphere [*Burke*, 2007]. Electrons are mostly precipitated into the ionosphere before they can significantly contribute to shielding. R2 FAC originates or terminates at the ion population inner edge of the Alfven layer. R2 FAC goes into the auroral ionosphere in the dusk sector and comes out of the auroral ionosphere in the dawn sector. The directions of R2 FAC is opposite to those of R1 FAC [*Iijima and Potemra*, 1978] which maps the polar cap electric field in the nightside magnetosphere. Development of R2 FAC tends to lag behind the polar cap electric field variations as convection requires time to redistribute magnetospheric plasma. The region 2 FAC creates zonal (in the dusk-to-dawn direction) charging in such a way that the potential drop across the inner magnetosphere more or less cancels the convection electric field in the dawn-to-dusk direction under steady state. In other words, R2 FAC tends to minimize the electric field at low latitudes giving rise the so-called shielding effect. In steady state, R2 FAC enhances the north-south electric field in the auroral ionosphere and decreases the electric field at low latitudes generating a shielding like scenario (Figure 1.12). Theoretical shielding time constant has been analytically derived to be of $\sim$30 minutes [*Senior and Blanc*, 1984]. Several other investigations revealed the time constant of the shielding process to be of $\sim$ 20-30 minutes [e.g. *Spiro et al.*, 1988; *Fejer et al.*, 1990; *Somayajulu et al.*, 1987; *Kikuchi et al.*, 2000; *Peymirat et al.*, 2000]. However, during times of rapid fluctuations in convection electric field, shielding is found to be broken for a much longer duration [e.g. *Kelley et al.*, 2003; *Huang et al.*, 2005] that cannot be explained on the basis of analytical models. During times of rapid increase of convection electric field (southward turning of IMF B_z), R2 FAC takes time to develop and shielding is temporarily rendered inactive or insufficient. During that period, the effects of convection electric field (or high latitude electric field) penetrates into the ionosphere over low-equatorial latitudes. This is popularly known as “prompt penetration” event (Figure 1.13). On the other hand, when the convection electric field suddenly decreases (northward turning of IMF B_z), R2 FAC takes time to again readjust and the residual R2 FAC contributes to the major part of electric field even in the ionosphere over low-equatorial latitudes. This is known as “overshielding” effect (Figure 1.13).

The polarity of prompt penetration electric field is generally westward in the post-midnight sector and eastward in the post-noon sector. On the other hand, overshielding electric field is generally eastward in the post-midnight sector and westward during

post-noon sector. Though prompt penetration and overshielding effects had been studied for several decades, many important questions remain unanswered. To reproduce verbatim *Huang et al.* [2007], “Penetration electric fields have been studied for almost 40 years in the context of aeronomy, magnetospheric physics, and later as an aspect of magnetosphereionosphere coupling. Despite significant progress in those areas, a number of critical problems remain unsolved. For example, how long can the interplanetary/magnetospheric electric field penetrate into the low-latitude ionosphere? How much of the interplanetary electric field can penetrate to the equatorial ionosphere? What determines the duration and strength of penetration electric fields? How effective is the shielding process during magnetic storms? What is the effect of the penetration electric field on the ionospheric plasma?..... ” Electrodynamics and neutral dynamics in the ionosphere over equatorial latitudes critically determine the plasma distribution over these latitudes. So to say, the role of IEF, through the prompt penetration and overshielding effect, can influence the equatorial ionosphere to a considerable extent. As of today, impacts of these effects in the low latitude ionospheric processes have not been understood comprehensively. In the present work, attempts are made to understand a few aspects of these effects.

Chapter 2

Optical, radar and simulation techniques

2.1 Introduction

In order to understand and characterize the equatorial spread-F structures revealed by VHF radar maps, the importance of the simultaneous optical measurement of thermospheric airglow emission was realized. With a view to obtaining the collocated VHF radar and optical airglow observations, an airglow photometer capable of measuring F-region airglow emission intensities at multiple wavelengths was conceived and fabricated at PRL. This photometer was operated in campaign mode during moonless periods mainly during the months of January-March from the year 2003 to 2006 from Gadanki (13.5^{o}N, 79.2^{o}E, dip angle 12.5^{o}N), the site for Indian Mesosphere- Stratosphere-Troposphere (MST) radar. The observations by the photometer and the Indian MST radar (a VHF radar) were supplemented by ionosonde data (HF radar) that were available from Sriharikota (SHAR: 13.8^{o}N, 80.3^{o}E, dip angle 14^{o}N), a station 100 km east of Gadanki, as well as from Thumba (8.68^{o}N, 77.0^{o}E, dip angle 0.5^{o}N), a dip-equatorial station.

2.2 Airglow Photometry

A multi-wavelength scanning nighttime photometer (Figures 2.1 and 2.2) is developed at the Physical Research Laboratory to study the airglow emission intensities from the thermosphere and mesosphere. This photometer has $\frac{f}{2}$ optics that is maintained througout the optical path. The photometer comprises of mainly three sections namely, the

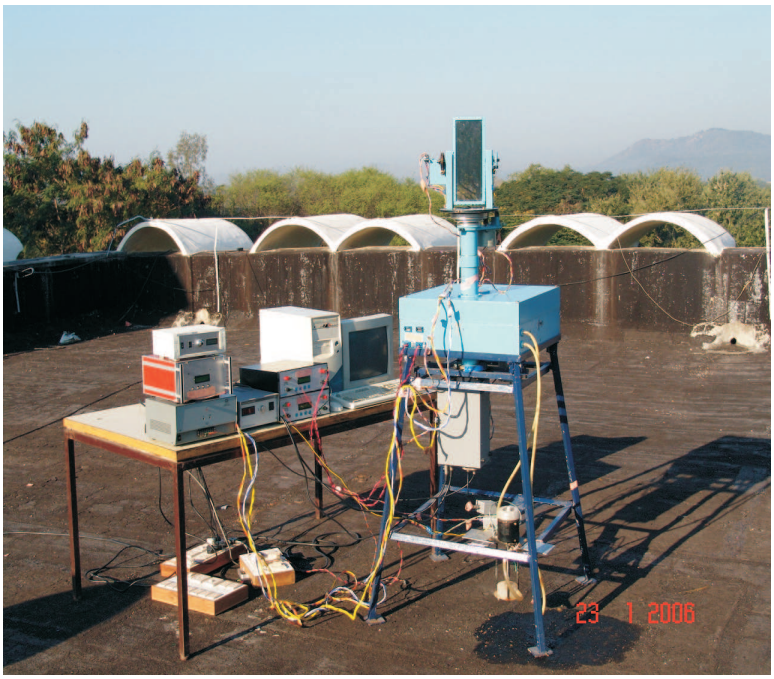

Figure 2.1: The setup of the photometer at the Indian MST Radar site, Gadanki.

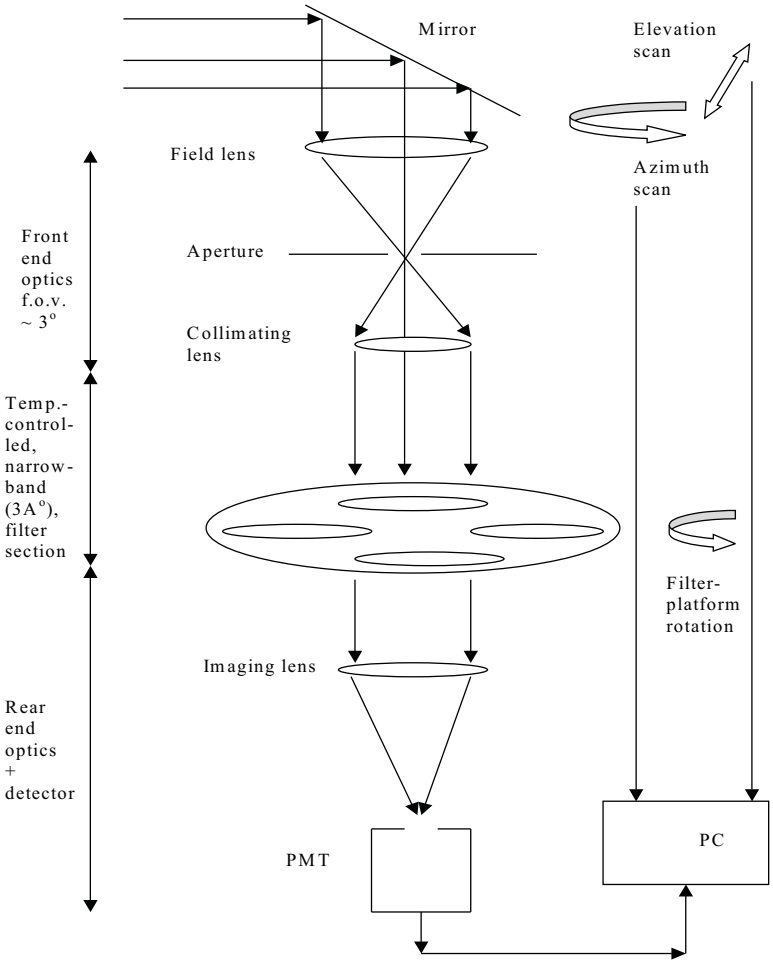

Figure 2.2: Optical schematic of the photometer.

front-end optics, the filter section and a detector section. The movements of the mirrors and the filters are effectively synchronized by control systems.

2.2.1 Front-end optics

The front-end optics section comprises of field and collimating lenses along with a field stop (field of view of $\sim 3^o$ which is close to the VHF radar beam width of ($\sim 2.8^o$)). The field lens and the aperture arrangement is used to strictly limit the undesired incoming rays reaching the optical system from a lower elevation angle. The optical beam is collimated after passing through the front-end optics. The filter section is kept in the collimated portion of the beam.

2.2.2 Filter section

A rotating platform consisting of four filter assemblies is arranged in such a way that one of the filter assemblies gets optically aligned with the front-end optics and the detector attached beneath the filter section. Narrow band (band width $\sim$0.3 nm), temperature-tuned interference filters are used in these filter assemblies. Characteristic features of a typical narrow-band interference filter is described below.

Interference filters are multi-layer thin film devices. The principle of operation of an interference filter is analogous to a lower-order Fabry-Perot etalon. The spectral (wavelength) rejection is done creating destructive interference conditions whereas constructive interference is encouraged for the wavelength of interest. A narrow band interference filter generally consists of several elements called cavities separated by absentee layer (low refractive index material). Multicavity design drastically reduces the transmission of out-of-band wavelengths. A single cavity consists of stacks separated by spacer ($\frac{\lambda}{2}$ thickness, λ peak transmission wavelength). A stack consists of multiple layers of alternate high (e.g. Zinc sulfide, ZnS) and low refractive index materials (e.g. Cryolite, Na_3AlF_6) each with $\frac{\lambda}{4}$ thickness. The number of layers in the stack is adjusted according to the width of the bandpass. In addition to the above layers, to facilitate blocking of undesired wavelengths in the longer and shorter wavelength sides, thin film coating and colored glass are used.

The central passband wavelength of an interference filter shift towards lower wavelength side with the increase in the incident angle. It can be shown that the wavelength of peak transmittance at small angles (ϕ) of incidence (upto $\sim 15^o$) is given by

$$\lambda_t = \lambda_i \sqrt{1 - \left(\frac{n_o}{n_e}\right)^2 \sin^2 \phi} \tag{2.1}$$

where n_o is the refractive index of the external medium (n_o=1 for air) and n_e is the "effective refractive index" of the spacer. λ_t and λ_i are the transmitted and incident wavelengths respectively. In addition to the wavelength dependence on the angle of incidence, the transmittance of an interference filter also depends on the temperature. As temperature increases, the layer thicknesses increase and the layer indices change. These two effects combine in such a way that the transmittance spectrum shift slightly to longer wavelength with increasing temperature.

In order to resist any temperature-related deviation of the peak transmission wavelength, filter temperature controllers are deployed. A typical filter assembly consists of a brass chamber enclosed in thermally insulated housing that provides isolation from the environment. The temperature of the brass chamber is controlled using a bi-polar temperature controller that employs Peltier elements and AD-590 temperature sensors (accuracy of $\sim 0.1^o$C).

2.2.3 Detector section

The filtered beam is focussed on the cathode of a photomultiplier tube (Type S-20; EMI 9863A.) housed in a temperature controller unit (FACT 50) provided by EMI. Some of the salient physical principles pertaining to this type of PMT is discussed below.

PMTs are detectors that are used for low light level applications. They consist of a photocathode and a series of dynodes in an evacuated glass enclosure. Owing to photoelectric effect, photoemissive cathode emits electrons after being hit by photons. The primary electrons are accelerated towards a series of additional electrodes called dynodes. These electrodes are maintained at a more positive potential. Secondary electrons are generated at each dynode. This cascading effect creates 10^5-10^7 electrons for each photon hitting the first cathode depending on the number of dynodes and the accelerating voltage. This amplified signal is finally collected at the anode where it can be measured. The equivalent circuit for a photomultiplier tube is an ideal current source in parallel with an output resistance R_o ($> 10^{12}\Omega$) and capacitance C_o (< 10pF). For current mode operation, the output voltage is a faithful representation of the input current. This occurs when $\tau \ll \tau_s$, where τ is the time constant of the PMT which is basically R_oC_o and τ_s is the time after which the light source decays 1/e of its initial intensity. For the voltage

mode operation, $\tau \gg \tau_s$. In this case, the pulse height in volts is proportional to the total input charge. Therefore, for low light level detection, the PMT is used in pulsed mode (or counting mode). When a PMT is operated in pulsed mode, $1/\tau$ should be fairly less that the event rate to avoid pulse pile-up effects.

Quantum efficiency (Q.E.) at a particular wavelength is the average number of photoelectrons produced per incident photon (expressed in percentage). In the present experimental setup, the quantum efficiency of the PMT used is $\sim 6\%$ for 630.0 nm and $\sim 3\%$ for 777.4 nm.

Depending upon the light level concerned and the gain required, a PMT with correct number of stages is chosen. Too many stages may enhance gain at the cost of electrical performance (low inter-electrode voltage due to space charge effects resulting in poor linearity and timing). On the other hand, too few stages may cause insufficient gain for a given allowed operating voltage. In fact, for low light level investigations, 11-14 stages have been found to be optimum and PMT with 14 stages has been selected for the present work reported here. The size of the cathode has to be optimally chosen as larger cathode size provides more dark counts and lesser cathode size demands stringent optics. The cathode size of the PMT used in the present experiment is 9 mm.

Gain of a PMT is decided by the current amplification. Each dynode amplifies the incident electron current and the overall gain is given by the product of the individual dynode contributions. In the present case, gain is $\sim 10^6$.

PMT output is obtained even in the absence of light input owing to the thermal effects. For dc applications, this is referred to as dark current and in pulsed applications, it is referred to as dark count. Dark count can be minimized using suitable cooling arrangement. In the present experimental setup, a FACT 50 PMT cooling unit (Thorn EMI) is used. This unit consists of a compact, forced air-cooled thermoelectric housing and a controller unit. Temperature can be set to within 0.1^oC and capable of cooling 50^oC below an ambient temperature of 20^oC.

If M photoelectrons are produced by a PMT per second and the PMT output is measured over a period of time T, then the average number of photoelectrons produced is MT. Now the photoelectric effect is a quantum-mechanical process and is subject to statistical fluctuations described by Poisson statistics. In Poisson statistics, the standard deviation associated with MT is $(MT)^{\frac{1}{2}}$. Therefore, the SNR is given by

$$SNR = \frac{MT}{(MT)^{\frac{1}{2}}} = (MT)^{\frac{1}{2}} \tag{2.2}$$

Therefore, even if the gain of the PMT is ideal (not noisy), the output signal will have the fluctuations described by the above expression. There is also an additional noise called multiplication noise associated with the statistical variation in the number of secondary electrons created per incident electron on each dynode.

2.2.4 Mirror and filter movements

A reasonably fast scanning mirror assembly was attached on top of the front-end optics to record the airglow intensity variations at different elevations and azimuths. Microcontroller-driven electronic drivers are used to move the mirrors and to rotate the filter platform. In the present case, the airglow intensity recorded at zenith and in the eastern direction (45^o elevation) are used. It is to be noted here that by comparing the identifiable points in the airglow intensity variations corresponding to vertical and eastern directions, the polarity of the zonal velocity of the background plasma at the airglow emitting altitude can be determined with reasonable accuracy. The rotation of the filter platform and the mirror scanning are controlled by a computer. Although, observations at four different wavelengths are possible with the help of this photometer, the optical observations had been made at two wavelengths (630.0 nm and 777.4 nm) pertaining to the thermosphere-ionosphere system. For a given wavelength observation in a fixed direction, the integration time is chosen to be 10s in the present experiments. However, for bidirectional mode and two wavelength operations, the time between successive counts for a given filter and direction turns out to be $\sim$90s.

2.3 VHF Radar and Ionosonde (HF radar) techniques

2.3.1 Principles of VHF radar

The VHF radar referred in the present work is basically a MST radar that can also be operated in coherent, pulsed mode to receive echoes from ionospheric irregularities. It is to be noted that coherence is the degree of phase correlation that exists at different points of an electromagnetic wave. While the temporal coherence is a measure of the phase correlation at different points along the direction of propagation, spatial coherence is a measure of the phase correlation at different points transverse to the direction of propagation. Temporal coherence reveals how monochromatic a source is whereas spatial coherence reveals how uniform the phase of the wave front is. Coherence length (L_c) is a measure of temporal

coherence. It is the distance over which coherence decays significantly and is measured in terms of the coherence time (τ_c) multiplied by the velocity of light in vacuum. The faster a wave decorrelates (smaller τ_c), the larger the range of frequencies Δf the wave contains (as period is inverse of frequency). Thus, there is a tradeoff.

$$\tau_c \Delta f \approx 1 \tag{2.3}$$

or, to put it in terms of wavelength,

$$\frac{L_c \Delta \lambda}{\lambda^2} \approx 1 \tag{2.4}$$

The above equation follows from the convolution theorem in mathematics, which relates the Fourier transform of the autocorrelation coefficients to the power spectrum (the intensity of each frequency). It is to be noted also that the spatial coherence is the cross-correlation between two points in a wave for all times. The range of separation between the two points over which significant spatial coherence exists is called the coherence area, A_c. Temporal coherence (and spatial coherence too) is obtained in lasers (e.g. a stabilised helium-neon laser can produce light with coherence lengths in excess of 5 m) whereas, spatial coherence principle is applied in the Young's double slit interferometer. A radio antenna array has large spatial coherence because antennas at opposite ends of the array emit with a fixed phase-relationship.

Whether a radar will be able to resolve the changes in a scattering medium (in the present case, F region of ionosphere) depends upon how fast the medium changes in comparison with the inter pulse period (IPP, inverse of pulse repetitive frequency, PRF) of the radar beam. Therefore, if ionospheric F region does not change appreciably between successive radio echoes, the echoes will have the same phase relationship that facilitates coherent addition. Therefore, if the plasma irregularity structures in the F region ionosphere vary slowly in comparison with IPP, the echoes can be added coherently to improve sensitivity. Incoherent radar echoes are uncorrelated in phase. Since the coherence time is relatively short in case of incoherent radars, the thermal fluctuations of the charged particles in the ionosphere can be studied. However, since the return echo is weak, the incoherent scatter radar requires transmitter of high power, large antenna, most sensitive receivers and sophisticated data processing. In contrast to the scattering from individual charge particle in case of incoherent scatter radar, the scattering takes place from the plasma irregularity structures in case of coherent backscatter radar.

In case of coherent backscatter radar, it is assumed that the plasma density fluctuations

do not alter the transmitted beam significantly so that the Born approximation remains valid. In addition to that, the scattering volume is considered to be much larger in comparison with the radar wavelength but not too small for the medium so that the medium can be treated as homogeneous. Under those conditions, if a radio wave impinges on a scattering volume containing discontinuities in the refractive index, then the radio wave scatters from the plasma refractive index changes that match the Bragg condition,

$$\mathbf{k} = \mathbf{k}_i - \mathbf{k}_s \tag{2.5}$$

where, $\mathbf{k}_i$ (rad/m) is the incident wavenumber vector, $\mathbf{k}_s$ (rad/m) is the scattered wavenumber vector, and $\mathbf{k}$ is the wavenumber vector of the refractive index perturbation that satisfies Bragg condition.

Now, in the case of backscattering,

$$\mathbf{k}_s = -\mathbf{k}_i \tag{2.6}$$

Therefore,

$$|\mathbf{k}| = \mathbf{2}|\mathbf{k_i}| \tag{2.7}$$

In terms of wavelength, that means,

$$\lambda = \frac{\lambda_i}{2} \tag{2.8}$$

This means that the backscatter radar, when operated in ionospheric mode, is able to probe ionospheric refractive index structures the spatial scale sizes of which are of the order of half the radar wavelength (in this case,6 m). The electron density fluctuations associated with these structures (spatial scale size is $\sim$3 m) are driven by plasma instability processes during post-sunset hours. In addition to that, the plasma structures are aligned along the geomagnetic field lines. This leads to high aspect sensitivity in the backscattered echoes. Aspect sensitivity refers to the dependence of echo power on the angle of incidence of the radio wave. The echo power decreases as the incident angle increases. In ionospheric backscattering, the radar beam must impinge on the field-aligned plasma structures perpendicularly so that the return echo strength is maximized.

2.3.2 Reduction of VHF radar data

The VHF radar at Gadanki operates at 53 MHz and the peak power-aperture product (product of the peak mean power and the effective antenna area) goes up to 3×10^{10} Wm^2. Higher power-aperture product enhances the radar signal-to-noise ratio (SNR). As stated

earlier, the radar is operated in coherent, pulsed mode to investigate the ionospheric irregularities. In ionospheric mode, the radar beam is oriented 13.2^{o}N and 14.8^{o}N from the zenith to make the beam orthogonal to the field-aligned E and F region plasma irregularities respectively. For an extremely narrow beam, the perpendicularity conditions are satisfied at 100 km and 350 km respectively. However, since the radar beam is 2.8^o wide, the radar beam satisfies the perpendicularity conditions over a broad altitude range. Therefore, it is possible to receive signals from a wide range of altitudes. Indian MST radar has phased antenna array that is aligned along the geomagnetic axis (2^o away from the geographic axis) in anticlockwise manner. The antennas are arranged in a square matrix consisting of 32 rows and 32 columns occupying an area of about 130m $\times$ 130m. The radar system includes 1024 (32$\times$32), three-element, cross-polarized Yagi antennas. 32 high power transmitters, 32 units of transmit-receive duplexers and a phase coherent receiver. One transmitter feeds a row of 32 Yagi antennae through a series feed of directional coupler. Transmitted powers and directional coupler outputs are tapered to achieve modified Taylor distribution with a design sidelobe level of -20dB for the planar array. The beam is tilted by the low power phase shifters associated with exciters of the transmitters. The antenna pattern has been characterized with the help of the radio source Virgo-A (3C 274) that transits over the radar site. It has been established that the beam-pointing accuracy is better than 0.2^o and the 3dB beam width is in the range 2.8 - 3^o. The radar, its subsystems and its operations in ionospheric mode are available in the literature [*Rao et al.*, 1995; *Patra*, 1997].

The return echo obtained by a VHF radar depends on the average transmitted power. However, the range resolution of the radar depends on the pulse width. A larger pulse width provides a better SNR. However, a larger pulse width implies coarser range resolution too. Therefore, there is a trade-off here also. For atmospheric studies, phase coding in the form of complementary codes is used to circumvent this problem as they render optimum range sidelobe suppression. However, for ionospheric applications, this is not done. This is due to the fact that range resolutions of the order of 3-4 km is sufficient for ionospheric investigations on most of the occasions. The backscattered signal obtained by the MST radar operating in ionospheric mode is a Doppler broadened spectrum that requires coherent detection. The quadrature receiver channels (in phase [I] and Quadrature [Q]) provide the in phase and quadrature components of the complex Doppler signal. These quadratures signals are coherently integrated for many pulse returns. This step reduces the volume of the data to be processed and improves SNR. Coherent integration

Table 2.1: Radar parameters for ESF experiments

Aspects	Specifications
Beam direction	14.8^o due magnetic north
Inter Pulse Period (IPP)	5 ms
Pulse width	32 μs
No. of FFT points	256
No. of incoherent integrations	8
No. of coherent integrations	1
Range coverage	84 - 680 km
Range resolution	4.8 km
No. of range bins	125
Code flag	uncoded

is possible because of the oversampling of the target owing to higher PRF of the radar in comparison with the typical characteristic Doppler frequency range. The operation of coherent integration tantamounts to low pass filtering of the signal. In time domain representation, this step is equivalent to applying a rectangular window of T_i duration. The power spectrum is then obtained by applying Fast Fourier Transform (FFT) algorithm. The power spectra, thus computed, are suitably averaged (incoherent integration) to reduce the noisy fluctuations in the spectra. This results in improved signal detectability. The radar parameters for the ESF experiments pertaining to the present work are listed in Table 2.1. Based on the averaged power spectrum, the following low order spectral moments are calculated.

The zeroth moment represents the total signal power, P_s.

$$P_s = M_0 = \sum_{i=l}^{u} P_i \tag{2.9}$$

SNR in dB is derived from P_s as follows

$$SNR = 10 \log \left(\frac{M_o}{N.L} \right) \tag{2.10}$$

where N represents the total number of Doppler bins and L is the mean noise level. The product N.L gives the total noise over the whole bandwidth. Doppler width is the full width of the Doppler spectrum and is equal to $2(M_2)^{\frac{1}{2}}$.

The first moment provides the weighted mean Doppler shift (line-of-sight phase velocity).

$$\overline{f_D} = M_1 = \frac{1}{M_0} \sum_{i=l}^{u} P_i f_i \tag{2.11}$$

The second moment represents the variance which is a measure of dispersion from the mean frequency.

$$f_w{}^2 = M_2 = \frac{1}{M_0} \sum_{i=l}^{u} P_i (f_i - M_1)^2 \tag{2.12}$$

In the above expressions of the moments, l and u represent the lower and upper limit of the Doppler bin of the spectral window, P_i and f_i are the powers and frequencies corresponding to the Doppler bins within the spectral window. In the present work, the zeroth and first moments are used to construct Range-Time-Intensity (RTI) and Range-Time-Velocity (RTV) plots of the plasma irregularity structures associated with ESF events.

2.3.3 Principles of Ionosonde (HF radar)

In addition to VHF radar, ionosondes are also being used to investigate the characteristic equatorial ionospheric phenomenon like ESF. However, the physical principle based on which an ionosonde works is quite different from that of the VHF radar mentioned earlier. In order to describe the propagation of radio waves in a uniform plasma under the presence of magnetic field, magneto-ionic theory that describes how the refractive index of an ionized medium will change, is applied. The Appleton-Hartree equation plays a pivotal role in the magneto-ionic theory. If collisions and the magnetic field are neglected, a simplified expression of the refractive index can be obtained from the Appleton-Hartree equation as follows.

$$n^2 = 1 - \frac{\omega_N{}^2}{\omega^2} \tag{2.13}$$

where ω_N is the angular plasma frequency and is given by

$$\omega_N = \left(\frac{N_e e^2}{\epsilon_0 m} \right)^{\frac{1}{2}} \tag{2.14}$$

Therefore, it is clear that $\omega_N{}^2$ is proportional to the electron density N_e. As a radio wave penetrates into the ionosphere, the electron density increases till the F region peak, and, as a consequence, the refractive index gets smaller. ω_N cannot exceed ω as n will be imaginary in that case. An imaginary b implies that the wave cannot propagate anymore. Therefore, $\omega_N = \omega$ is the level where the plasma frequency equals the radio wave frequency. Based on this, a mathematical expression for the peak electron concentration in

the ionosphere can be found out.

$$f_N = (80.5N_e)^{\frac{1}{2}} \tag{2.15}$$

where f_N is in Hz and N_e is in m^{-3}. Therefore, if one assumes that the pulse travels with uniform speed (with the speed of light), then the peak height can be found out from the time delay of the echo. However, there is a caveat here. The radio pulse does not travel with the speed of light,c, but with the group velocity, u. Group velocity is related to c through the group refractive index in the following way.

$$u = \frac{c}{n_g} \tag{2.16}$$

Therefore, as the group refractive index increases as the wave penetrates ionosphere, the group velocity decreases implying that the radio pulse travels more slowly than light. Therefore, the height information obtained from the time delay is not “true” but “virtual”. The “virtual height” arising out of the group retardation of the radio wave needs to be corrected to determine the “true height”. The maximum plasma frequency of a given ionospheric layer is called the critical frequency for that layer. The maximum critical frequency of the whole ionosphere is conventionally termed as penetration frequency.

If the magnetic field is included, the refractive index becomes double-valued. The ionosphere becomes birefringent and the situation is analogous to the response of an optically active crystal to light. Radio waves propagates at two different speeds. These two “characteristic waves” are named as ordinary (in the present work, only ordinary waves are addressed) and extra-ordinary waves if refractive index is positive and negative respectively. When collisions are significant, the refractive index is complex and a wave propagating through the medium varies with time and distance. Absorption of radio waves becomes significant.

2.3.4 Reduction of ionosonde data

In an ionosonde, a pulsed transmitter and a receiver are swept synchronously in frequency and the echo delay time (which gives virtual height information) is recorded as a function of radio frequency. A plot of virtual heights of the returned echo with respect to the swept frequencies is generally known as ionogram. The ionograms from Thumba and SHAR are used in the present study. Both the ionosondes are IPS-42 type (manufactured by KEL Aerospace). The ionograms are scaled with the help of the DIGION software, real heights are determined based on POLAN software and afterwards, bottomside electron

density profiles are constructed based on EDEN software [*Titheridge*, 1998]. Further, based on the layer height measurements over dip equator (in the present investigation, Thumba), the vertical plasma drifts corresponding to the zonal electric field are obtained based on the methodology described by *Krishna Murthy et al.* [1990]. In this method, the vertical drifts, determined from the temporal movements of the F-layer height, are corrected for the chemical loss process if the layer height is below $\sim$ 300 km as pointed out by *Bittencourt and Abdu* [1981]. In the initial years of ionospheric research, broadened echo traces on ionograms in the presence of plasma irregularity structures in the nighttime equatorial ionosphere was termed as Equatorial Spread-F (ESF) events. This terminology is still continued although many aspects of ESF are understood based on many techniques including the present work which involves optical, radar and numerical simulation techniques. The principles of optical and radar techniques are already discussed. Numerical simulation technique is discussed in the following section.

2.4 Numerical Simulation technique

The nighttime development of plasma bubble is investigated by means of numerical simulation model of ESF described by *Sekar et al.* [1990, 1994]. In this model, the equatorial ionosphere during the post-sunset hours is treated in a slab geometry. The $\mathbf{X}$, $\mathbf{Y}$, and $\mathbf{Z}$ of the coordinate system used in the model are directed along westward, upward and northward directions respectively. The effects of the off-equatorial E region conductivities are not considered in the development of the field-aligned plasma irregularities so that the two-dimensional treatment of the non-linear evolution of plasma bubbles is possible. Following set of plasma fluid equations describe this model.

$$\frac{\partial N_\alpha}{\partial t} = P - L - \nabla \cdot (N_\alpha \mathbf{V}_\alpha) \tag{2.17}$$

$$\Big(\frac{\partial}{\partial t} + \mathbf{V}_\alpha \cdot \nabla\Big)\mathbf{V}_\alpha = \frac{q_\alpha}{m_\alpha}\Big[\mathbf{E} + \mathbf{V}_\alpha \times \mathbf{B}\Big] + \mathbf{g} - \nu_{\alpha n}(\mathbf{V}_\alpha - \mathbf{W}_n) \tag{2.18}$$

$$\nabla \cdot \mathbf{J} = 0 \tag{2.19}$$

$$\mathbf{J} = |q|\ (N_i \mathbf{V}_i - N_e \mathbf{V}_e) \tag{2.20}$$

where charged species is denoted by α ($\alpha \equiv$ i for ions and and e for electrons). The first equation in the above set of equations is the continuity equation where P is the production rate which closer to zero during nighttime. L is the loss term given by $\nu_R \mathrm{N}_\alpha$, where ν_R is recombination coefficient and N_α is the number density of the species (α = i for

ions, and e for electrons). The second equation is the momentum equation where the effects of neutral wind ($\mathbf{W}_n$), gravity (g), electric field (**E**), and the Lorentz force due to the movement ($\mathbf{V}_\alpha$) of the charged particles are taken into account. In this equation, q, $\nu_{\alpha n}$, and m represent the charge of the species, the collisional frequency of the charged particles with the neutrals, and the mass of the species respectively. The third equation is basically the current conservation equation where the total current density is given by the fourth equation. The left hand side (LHS) of the momentum equation is taken as zero since the inertial timescale is much larger than either the gyro period or the average inter-collision time. The steady state velocities of ions and electrons perpendicular to the magnetic field are obtained by solving the second equation with the assumptions that $\nu_{en} \gg \Omega_e$, $\nu_{in} \gg \Omega_i$, and e$\mathbf{E} \gg$ m$_e$**g**. These assumptions hold good for the F region of the ionosphere. Assuming quasi neutrality (N$_i \simeq$ N$_e$ = N), the total current density **J** is obtained from the fourth equation. It is to be noted here that **J** depends on the differential velocity between ions and electrons. Thereafter, **J** is replaced in the current conservation equation (third equation) and it is assumed that the field aligned currents (currents parallel to **B**) are negligible in the equatorial ionosphere. The electric field term in the divergence equation can now be replaced by the negative gradient of the potential Φ.

$$\mathbf{E} = -\nabla_\perp \Phi \tag{2.21}$$

It is to be noted here that since the ionospheric electric fields are curl-free, the potential is electrostatic in nature. A first order perturbation analysis is then worked out assuming that the potential Φ is composed of a steady state potential (Φ_o) and a perturbation potential (Φ_1).

$$\Phi = \Phi_o + \Phi_1 \tag{2.22}$$

As a consequence, the basic plasma fluid equations are eventually reduced to the following two coupled partial differential equations.

$$\nabla.(\nu_{in} N \nabla_\perp \Phi_1) = B[-g + W_y \nu_{in} + (E_{xo}/B)\nu_{in}]\frac{\partial N}{\partial x} \tag{2.23}$$

$$\frac{\partial N}{\partial t} - \frac{\partial}{\partial x}[(N/B)(E_{yo} + \frac{\partial \Phi_1}{\partial y})] + \frac{\partial}{\partial y}[(N/B)(-E_{xo} + \frac{\partial \Phi_1}{\partial x})] = -\nu_R N \tag{2.24}$$

In the above equations, E_{xo}, E_{yo} and W_y are the background electric field components in zonal (**X**) and vertical (**Y**) directions and vertical wind respectively. The first term in equation 2.23 is the Rayleigh-Taylor term that is contributed by gravity. The second and third terms take care of the effects of vertical wind and zonal electric field respectively in

the perturbation potential. Equation 2.23 brings out the spatial distribution of the perturbation potential generated by the generalized Rayleigh-Taylor (GRT) instability in a slab geometry. The temporal evolution of plasma density is described by equation 2.24. In this equation, the transport effects due to the perturbation potential and the effects of recombination are taken into account. Numerical solutions of these coupled partial differential equations are obtained over a plane orthogonal to earth's magnetic field over dip equator.

Equation 2.23 is an elliptic partial differential equation which is first approximated by finite difference equivalence that divides the solution into grids or nodes. The difference equations are subject to the prescribed boundary/initial conditions. Thereafter, successive over-relaxation (S.O.R) method is used in an iterative manner to solve the potential equation. In S.O.R, using the weighted average of the previous and present iterate values, a new Φ^k_{1new}(I,J) is constructed from the old Φ^k_1(I,J) (note that Φ^k_1(I,J) is the kth iterate by convention) with the help of a relaxation factor R. To determine the optimum value of R is probably the most difficult job. The value of R lies between 1.0 and 2.0 for S.O.R. In the present case, it has been found that R = 1.75 is the most appropriate value for convergence purpose. For every iteration, the maximum relative error is evaluated and compared with certain number (1×10^{-4} in this case) that determines the relative accuracy of the numerical results. Equation 2.23 is solved at incremental times (Δt) wherein the new input N(t) is obtained by solving equation 2.24. The initial values for potential at different times (t) are taken to be the potential values corresponding to the previous times (t-Δt) with the exception of t_o when potential is taken to be zero. It is to be noted here that the finite difference method is always associated with "truncation error". Whenever there exists steep gradients in N, the truncation error by second order difference scheme may be as large as that of the solution. Or to put it in different words, the lower order schemes suffer from excessive numerical diffusion. The truncation error can be reduced by using higher order difference scheme but the solution may contain spurious oscillation wherever steep gradients are present. In order to address this problem ("numerical shock"), the multi-dimensional flux-corrected transport (FCT) algorithm is formulated by *Zalesak* [1979] based on the FCT algorithm originally developed for single dimension by *Boris and Book* [1973, 1976] and *Book et al.* [1975]. The FCT algorithm is able to handle conservation equations in the vicinity of shock waves and other discontinuities without violating the positivity and monotonicity of mass and energy. FCT is carried out by adding a strong numerical diffusion (by using a low order scheme) to obtain monotonic ("ripple-free") results (with guaranteed positivity) followed by a compensating "antidiffusion"(constructed

by taking a weighted average of a flux computed by a low order scheme and a flux computed by a high order scheme) that reduces numerical error. The basic objective of FCT is to “limit” or “correct” these antidiffusive fluxes before they are applied so that no unphysical extrema are created in the solution (for a detailed discussion on the solutions of equations 2.23 and 2.24, see *Sekar*, 1990]. Using these methods, the solutions for N(t,x,y) are obtained.

Chapter 3

Coordinated observations of Equatorial Spread F by optical and radar techniques

3.1 Background

The structures and dynamics of equatorial Spread F (ESF) irregularities have been investigated with VHF backscatter radar which is one of the powerful tools to simultaneously observe the bottomside and topside ionospheric irregularities. Many observations from various longitudinal sectors [*Tsunoda*, 1980; *Patra et al.*, 1995] have been reported ever since the first backscatter radar observation was reported by *Woodman and La Hoz*[1976]. In order to understand different aspects of ESF, a number of co-ordinated measurements have been carried out by different workers [*Szuszezewicz et al.*, 1980; *Kelley et al.*, 1986; *Raghavarao et al.*, 1987; *Sridharan et al.*, 1997]. Plasma irregularities associated with equatorial Spread F manifest themselves in a variety of forms on VHF radar maps ranging from rising plumes and multiple plumes to ESF structures confined to the bottomside of the ionosphere. A few meter scale size irregularities are generally responsible for the back scatter echoes recorded by the VHF radar. The causative mechanism for the ESF irregularities in the scale sizes of 1-10 m is not yet comprehensively understood [*Huba and Ossakow*, 1979]. However, co-ordinated measurements [*Szuszezewicz et al.*, 1980; *Kelley et al.*, 1986] have revealed that the plume structures as observed by the VHF radar are found to be collocated with large scale plasma bubbles generated by the action of collisional Rayleigh-Taylor (CRT) instability [*Haerendel*, 1974] and associated nonlinear

processes [*Ossakow*, 1981; *Sekar et al.*, 1994]. The multiple plume structures are generated by CRT instability seeded by spatially varying electric fields associated with gravity waves [*Huang and Kelley*, 1996]. The confinement of ESF structures to the bottomside of the ionosphere was shown [*Sekar and Kelley*, 1998] to be due to the combined action of vertical shear in zonal plasma drift and westward electric field associated with a particular temporal pattern of the zonal electric field. Thus the VHF radar echoes have been used to interpret the physical processes associated with the large scale ESF structures. However, as the return echo strength in a VHF radar is proportional to the square of the electron density fluctuations, VHF radar technique is insufficient to characterize the plasma irregularity structures (associated with ESF) in terms of plasma depletion or enhancement. The Doppler velocities inside some of the structures are predominantly upwards which are generally associated with plasma bubble. However, downward velocities inside the structures are also not uncommon [*Patra et al.*, 1997; *Rao et al.*, 1997; *Laakso et al.*, 1994]. The structures observed by VHF radar moving with downward drift could be associated with plasma enhancements under certain conditions. On the other hand, the "fossil" bubble (plasma depletion in non-evolutionary phase), under the action of westward ambient electric field, can also move downward. Thus the presence of downward movement in the RTV (Range-Time-Velocity) map need not unequivocally indicate the presence of enhancement structures. As the radar technique alone is inadequate to identify the nature of the structures, simultaneous airglow measurements have also been carried out to characterize the VHF radar observations.

Airglow photometry in multiple wavelengths can serve as a potentially complementary technique to address the above issue. The structures in ESF, particularly those with large scale sizes have been studied using scanning optical photometers [*Takahashi et al.*, 1989; *Sipler et al.*, 1981] and all sky imagers [*Weber et al.*, 1978; *Sahai et al.*, 1994; *Mendillo et al.*, 1997; *Sinha et al.*, 1996]. Depletions and enhancements in airglow intensities during ESF events [*Mendillo et al.*, 1985; *Sinha et al.*, 1996] have been recorded by imagers. Thermospheric airglow emissions like 630.0 nm from $\sim$250-300 km altitude region and 777.4 nm from the F region peak altitude have generally been used as tracers to record the modulations in the F region ionization. It is known that the 630.0 nm emission line intensity during nighttime is proportional to the electron density as the emission process is an outcome of dissociative recombination of O_2^+ with the ambient electron. Similarly, the 777.4 nm emission intensity due to the radiative recombination process of O^+ is proportional to the square of the electron densities. However, the temporal variation

in 777.4 nm emission intensity is directly proportional to the product of electron density and its variation. In view of these aspects, both these thermospheric emission line intensities are used to infer the modulations in the F region ionosphere. The modulations in the temporal variation of nocturnal airglow intensities have been found to be associated with the variations in the F layer heights [*Barbier*, 1959], with the well known equatorial reverse plasma fountain [*Kulkarni and Rao*, 1972; *Sridharan et al.*, 1993; *Sekar et al.*, 1993], with the meridional wind reversal associated with midnight temperature anomaly [*Herrero and Meriwether*, 1980] and plasma depletions [*Sipler et al.*, 1981]. Most of the earlier studies have been carried out using photometers having a broad spectral range (band width ranging from 0.6 nm to a few nm) and as a consequence, without the requirement of stringent temperature tuning of the interference filters used. On the other hand, the airglow imagers which have been usually deployed for ESF investigations are devices aimed at having large spatial coverage (large field of view) and hence filters with large bandwidth are used. A narrow band ($\sim$0.3 nm) photometer along with the ALTAIR radar [*Sipler et al.*, 1981] was operated to obtain all sky map of airglow intensities which revealed airglow depletions. Although the plasma drift velocities obtained by the photometer were compared with the line- of-sight neutral wind velocities measured by a collocated airglow spectrometer, the variations in the airglow intensity were not compared with the ESF structures obtained by the radar.

In order to unravel the association of the variations in the airglow intensity with the ESF structures revealed by VHF radars, co-ordinated campaigns were conducted at Gadanki by simultaneously operating the MST radar and a narrow pass-band photometer during the months of March, 2003 and January-March for the past four years (2004-2006). Simultaneous radar and optical observations reveal optical signatures corresponding to a variety of equatorial spread F (ESF) structures. Depending upon the altitude of the plume structures and the bottomside structures, the optical signatures in 630.0 nm and 777.4 nm are found to be in conformity with large scale structures of ESF.

3.2 Identification of plasma enhancement structure associated with ESF

Based on a two-dimensional, non-linear numerical simulation model developed at Physical Research Laboratory, *Sekar et al.* [2001] predicted the presence of plasma enhance-

ment structures moving downward at altitude region beyond 350 km during ESF events. It was shown that multiple wavelength mode seed perturbation can explain such plasma enhancement structures in a buoyancy-dominated region. In order to experimentally detect such plasma enhancement structures, a coordinated campaign using Indian MST radar and narrow band, multi-wavelength airglow photometer was conducted during March, 2003 from Gadanki. Figure 3.1 depicts composite results obtained from this campaign on 25th March, 2003 when ESF was present. The horizontal axis corresponds to time in IST (Indian Standard Time, IST = Universal Time, UT + 5.5 Hr) which is common for all the subplots. The range- time-intensity (RTI) and range-time-velocity (RTV) of the radar echoes are plotted in subplots (A and B). The colour codes in them correspond to intensity of return echoes in (A) and line-of-sight Doppler velocities in (B). The vertical columnar intensities of 630.0 nm and 777.4 nm airglow emissions are depicted in (C) and (D) subplots of Figure 3.1. The RTI map in Figure 3.1A consists of wave-like bottomside structures and vertically rising and/or slanted plume structures in the height region above 350 km. The velocities in the bottomside structures are predominantly downward except during 20:15 to 20:30 and 21:45 to 22:15 IST. The velocities inside plume structures are upward in certain regions and downward in other regions. Downward velocities of the order of 50 m/s are also seen. The temporal variation of the 630.0 nm airglow intensities in Figure 3.1C comprises of a monotonic decrease during the initial phase along with macro and micro variations in the later phase. The macro variations are marked at the nodal points by alpha-numerical letters L1 to L7. It is to be noted that any variations in the airglow intensity which spans in time $\leq$15 min and in amplitude $\sim$2-3 times more than the statistical noise level (square root of the count level) are considered to be as “micro” variations. They are marked at the regions of mutual correspondence by the tips of the pointers emanating from the symbol boxes denoted by “S”. These boxes are placed suitably to avoid cluttering and to prevent them obscuring the structures shown by the radar map. In Figure 3.1C, the micro variations are denoted by S4 to S7. Note that the symbols corresponding to micro variations are marked in the RTV maps instead of the RTI maps for the purpose of clarity. The altitude variation of the base height of the F region (h’F) obtained from the ionograms over SHAR is also plotted in Figure 3.1C along with the temporal variation of the 630.0 nm intensity. The macro variations in the 777.4 nm airglow intensity in Figure 3.1D are reasonably similar with those in the 630.0 nm intensity corresponding to Figure 3.1C. In addition to them, micro variations are seen in between 20:30 to 20:45 IST, which are denoted by S1 to S3.

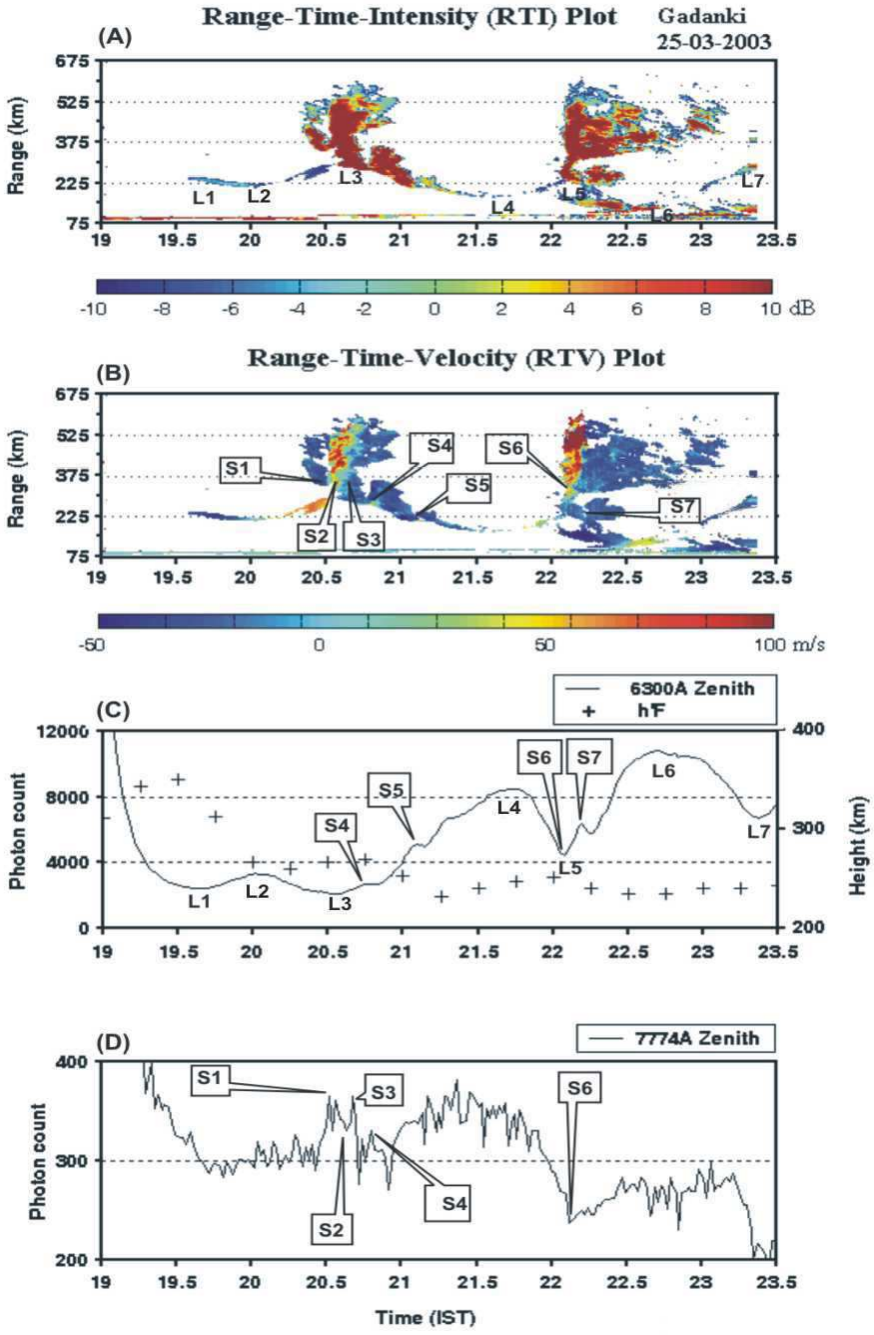

Figure 3.1: Composite plots of temporal variations of (A) Range and Intensity (RTI), (B) Range and Velocity (RTV), (C) 630.0 nm airglow intensity (solid line) along with h'F (+) and (D) 777.4 nm airglow intensity on an equatorial Spread F night, 25 March, 2003. The colour codes in (A) and (B) denote the intensity and the velocity respectively. L1 to L7 represent the nodal points of the macro variations in airglow intensity corresponding to the bottom side structures revealed by RTI map. S1 to S7 represent the region of mutual correspondence between the radar structures and the micro variations in the airglow intensity. Note that the variations denoted by S1 to S3 are only in 777.4 nm while the variation denoted by S7 is only in 630.0nm. However, the variarions denoted by S4 to S6 are found in both the emission lines.

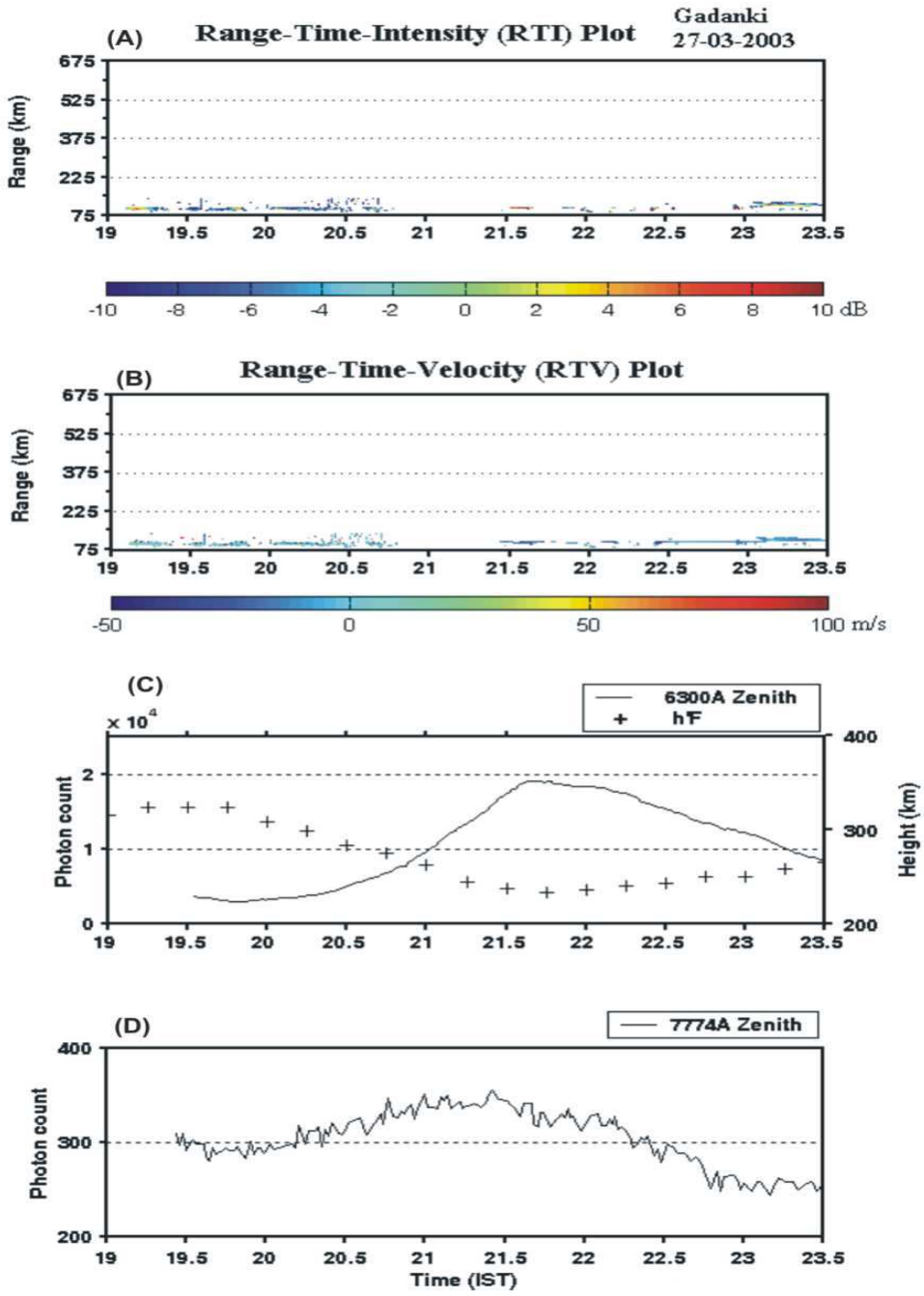

Figure 3.2: Similar to Figure 3.1 showing the absence of micro variations in the airglow intensity on a non-ESF night, 27 March, 2003.

Note that these micro variations are present only in 777.4 nm intensities corresponding to high altitude plume structures in Figure 3.1A. The micro variations such as S4 and S6 are present in both the emission lines while the micro variation denoted by S7 is present only in 630.0 nm emission line.

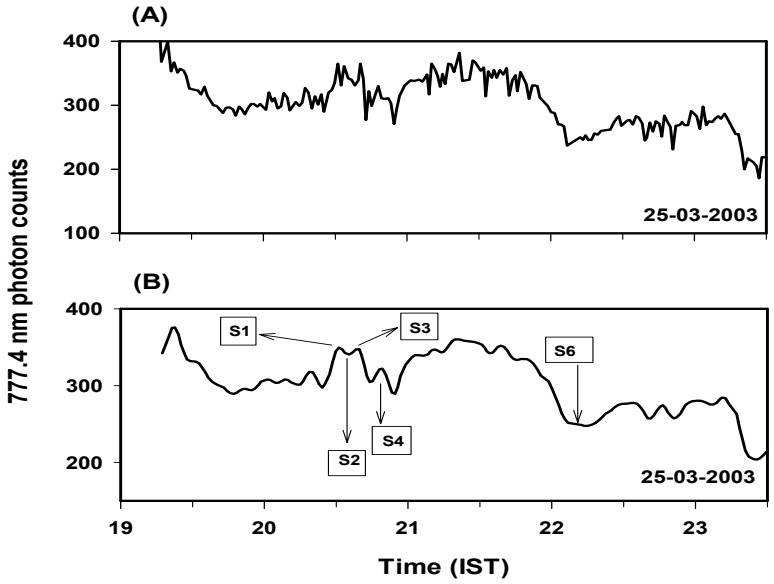

Figure 3.3: (A) Nocturnal variation of 777.4 nm intensity on 25 March, 2003 as observed by the photometer and, (B) reconstructed variation after the removal of high frequency components in the frequency domain.

Figure 3.2, consisting of similar subplots (3.2A-D), depicts the corresponding temporal variations on a night (27 March 2003) when ESF activity was not present. As expected, there is no VHF radar structure in the F region, only some E region structures. In subplots 3.2C and 3.2D micro variations above the statistical noise are not seen. However, macro variation in the airglow intensity corresponding to the F region base height (h'F) variation is observed. The temporal variation of the F region base height depicted in the subplot 3.2C is found to be in anti-correlation with the macro variation present in 630.0 nm intensity.

The 777.4 nm emission intensities on both nights are, in general, less intense compared to the 630.0 nm emission intensities as the radiative recombination rate responsible for 777.4 nm emission is orders of magnitude smaller than dissociative recombination rate. Further, the quantum efficiency of the photomultiplier tube used in the present optical experiment is less in the wavelength regime of 777.4 nm compared to 630.0 nm. Thus the statistical noises are higher in 777.4 nm emission intensities. In order to reduce the statistical noise in 777.4 nm intensity variation, the following procedure is adopted. The time series data obtained on 25 March 2003 were subjected to Fourier analysis and a low pass filter (frequencies more than 6 cycles/hr are eliminated) was applied in the frequency domain and a reconstruction was made in the time domain. Figure 3.3 depicts the reconstructed data along with the original one. All the micro variations marked in Figure 3.1

are clearly seen in the reconstructed data.

3.3 Discussion on the observational evidence of plasma enhancement structures associated with ESF

The optical observations obtained on an equatorial Spread F night (25 March, 2003) exhibit macro and micro intensity variations. (see Figure 3.1C-D). The nodal points indicating phase changes in the macro variations of 630.0 nm intensity are in anti-correlation (intensity maximum coincide with altitude minimum) with the phase changes in the observed bottomside wave- like structures on the RTI map depicted in Figure 3.1A. As expected from the well known Barbier type relation, the macro variations in the airglow intensities are found to be anti-correlated with the variation of the base height of F region. However, the amplitudes of the large scale structure in 630.0 nm variations are not proportional to the amplitude variation of F region base height. This can be attributed to the additional role played by the F region electron density to the 630.0 nm emission intensities as given by the Barbier relation [*Barbier*, 1959]. Certain characteristic low-latitude processes like reverse fountain effect and/or midnight temperature anomaly may also contribute to the above mentioned departure in amplitude. However, the similarities in the macro variations of both the line emissions (630.0 nm and 777.4 nm) suggest that these macro variations are mainly due to the altitude variations of the F layer. As the macro variations in airglow intensity primarily depend on the base height variation of the F region, they are also found on the nights when ESF is not observed (see Figure 3.2). On certain equatorial Spread F nights, variations in the F region base height manifest as a bottomside large scale wave-like structure depending on the amplification by Rayleigh-Taylor instability mechanism of large scale perturbation associated with the F region layer movement.

The micro variations observed in 630.0 nm and 777.4 nm intensities are found to be in correspondence with the plume structures in RTI maps. Those plume structures whose roots extend up to 250 to 300 km altitude region such as S4 to S7 register their presence as micro variations in 630.0 nm intensity and those plume structures which spread over F region peak altitude register their signatures only in 777.4 nm intensity. For example, the structures in the RTI maps corresponding to S1 to S3 have optical signatures only in 777.4 nm and not in 630.0 nm intensity. In addition to the micro variations (see S2 and

S6) corresponding to plasma depleted structures, micro variations (see S1, S3 and S7) corresponding to plasma enhancement structures are also observed. Some of these micro variations (see S1 and S3) which represent plasma enhancement structure extend well above 350 km with corresponding significant downward movement. This is an evidence for enhancement which is seen well above 350 km in a buoyancy dominated region which cannot be controlled by ambient westward electric field alone. Further, micro variations are found to be absent on the night when ESF is not observed. Thus the micro variations are essentially associated with plasma structures developed during ESF activity.

The upward moving depletions have been observed by other optical measurements involving imaging technique [*Mendillo et al.*, 1985; *Sinha et al.*, 1996]. The measurements of airglow enhancement flanking depletions were reported over Asian [*Sinha et al.*, 1996] and South American [*Mendillo et al.*, 1985] longitudes using imagers with wide band filters. *Mendillo et al.*[1985] compared their observation with the simulation studies using a long wavelength mode as seed perturbation. This study [*Mendillo et al.*, 1985] revealed that the airglow depletions corresponding to ESF bubble structure flanked by regions with relatively enhanced plasma concentration. However, in this investigation the variation of the background F region of the ionosphere is not included. As discussed earlier, the background F region movement can also manifest into macro variation in airglow intensity in the temporal domain. Therefore using an imaging technique, which employs a wide band filter and wide angle coverage, it is difficult to differentiate whether those airglow structures (particularly in 630.0 nm) correspond to the F region height variation or are due to plasma processes associated with ESF structures, especially when the observation site is close to the magnetic equator. With the help of such imaging technique, it is easier to identify the ESF structures which correspond to plasma depletions rather than plasma enhancements as the degree of depletion is an order of magnitude larger compared to the degree of enhancement with respect to the background ionization level during Spread F events. In addition to that, relatively small enhancements are often embedded in the depletion zones (see S7) making the identification by optical imaging technique even more difficult. However, using narrow band photometry with temperature-tuned interference filter, it is possible to unambiguously identify these structures in ESF.

As mentioned earlier, the radar observations were obtained at $14.8^{o}N$ with respect to zenith. The optical measurements, on the other hand, correspond to the zenith direction. Therefore, it is clear that in spite of the radar and the optical instrument being collocated, two different spatial regions in the sky are probed by the radar and the photometer at

the altitude range of 250-300 km. The regions probed by radar and the photometer are separated along the meridional direction by 65-90 Km. However, despite this horizontal separation, a remarkable similarity between the radar structures and the micro variations in airglow intensity is observed. Taking into consideration of the magnetic field aligned nature of ESF structures, the magnetic field geometry over the Indian zone, and the altitude extent of the airglow emission layers, it is easy to visualize that the field line mapping is responsible for the similarity between the optical and radar measurements. This suggests that the micro variations are the manifestation of large scale magnetic field aligned structures like plasma bubbles which provide platform for the generation of meter scale size plume structures. Earlier co-ordinated measurements [*Tsunoda and Towle*, 1979] revealing collocated large scale bubble with meter scale size irregularities, provide support for the present observation. Owing to narrow band and narrow beam photometry, the plasma bubble and enhancement structures register micro variation in this type of photometry. Thus, this kind of photometry provides the opportunity to get both micro variations due to plasma structures and macro variations due to background ionization.

Figure 3.1 suggests that the seed perturbation with more than one wavelength is required to give rise plume structure modulated over a bottom side wave like structure. In this connection, the numerical simulation of F region plasma structures with two long wavelength modes as initial perturbation is relevant. That simulation revealed the presence of plasma enhancements which move downwards at an altitude beyond 350 km [*Sekar et al.*, 2001]. These relative enhancement structures are found to vary with relative amplitude, wavelength and phases of the two modes. The present observation of 777.4 nm airglow intensity enhancement which is likely to be due to the plasma enhancement provides an experimental verification of the earlier prediction [*Sekar et al.*, 2001].

3.4 Simultaneous optical and radar observations during 2003-2006 on ESF structures

As already stated, coordinated optical and radar observations of ESF events were made in campaign modes during the months of March, 2003 and January-March from the year 2004 to 2006 in the moonless periods and in the clear-sky conditions. Twenty-four cases of ESF events were captured during these campaigns. Most of these ESF events were pre-midnight events and a few ESF events continued during the post-midnight hours also.

In the following section, some of the ESF events are presented where optical signatures are available corresponding to the ESF structures.

3.4.1 11 February, 2004

Figure 3.5 depicts the results obtained from both the VHF radar and airglow photometer on 11 February, 2004. The Range-Time-Intensity (RTI) and Range-Time-Velocity (RTV) of the radar echoes are shown in subplots 3.5a and 3.5b. The colour codes in them correspond to intensity of return echoes in (3.5a) and line-of-sight Doppler velocities in (3.5b). The vertical and slant (along east 45^o) columnar intensities of 630.0 nm and 777.4 nm airglow emissions are depicted in (c)and (d) subplots of figure 3.5. Note that there are gaps in radar data during 20:45 to 21:15 hr and in photometer data during 19:50-20:30 hr. The RTI map in figure 3.5a reveals a wave-like bottomside undulation along with vertically rising or slanted plume structures. The bottomside undulation encompassed from ~ 225 km to as high as $\sim$400 km altitude region. The temporal variations of 630.0 nm airglow intensities observed from zenith (red) and east (blue) reveal monotonic decrease during initial phase followed by large and small scale variations. The small scale variations are not prominent in slant columnar intensity while large scale variations are prominent in both directions. It is interesting to note that the integrated slant columnar intensity is less than vertical columnar intensity on occasions. The temporal variations of 630.0nm along zenith direction depicted in figure 3.5c, reveal a large scale enhancement between 21:15 to 22:00 IST. Corresponding to this time interval, the integrated intensity over slant columnar intensity is found to be less. An enhancement is observed at a displaced time interval for the slant columnar intensity variation depicted as dotted profile in figure 3.5c. Comparing figure 3.5c and 3.5d, it is clear that 777.4 nm intensity variations over zenith during 21:15 to 23:00 IST are anti-correlated with the intensity variations of 630.0 nm over zenith. During the same time interval, the intensity variation of 777.4 nm over east is found to be correlated with the intensity variation of 630.0 nm over zenith. A similar correlation is also observed between the intensity variations of 777.4 nm over zenith with 630.0 nm over east.

3.4.2 19 March, 2004

Figure 3.6 depicts a similar set of VHF radar map and corresponding airglow signatures. In figure 3.6a, the RTI map reveals that ESF structures are confined around 250-300 km.

Thus the bottomside confined ESF structure is observed without any plume events. The corresponding RTV map in figure 3.6b brings out the upward moving region flanked by downward moving regions in that confined structure. Corresponding to this structure, the response is seen only in 630.0 nm airglow intensity variation over zenith as depicted in figure 3.6c. It is interesting to note that the vertical columnar intensity during 19:45 to 20:15 IST is found to be more than the slant columnar intensity. A steep rise in 630.0 nm intensity is observed in both vertical and slant columnar intensities at around 20:45 IST and at 20:15 IST respectively. In the absence of high altitude structures (like plumes), no significant intensity variation is observed in 777.4 nm as revealed by figure 3.6d.

3.4.3 21 March, 2004

Figure 3.7 depicts a similar set of subplots for yet another case of ESF. Figure 3.7a reveals a wavelike bottomside structure confined between 250-300 km during time interval of 20:00 to 21:30 IST. However, a couple of plume structures extending upto around 380 km are also noticed around 22:00 IST. A trough in the bottomside structure with a very slanted plume is seen around 20:45 IST. The RTV plot in figure 3.7b reveals downward velocity in the vertically elongated plume structures as well as in the slanted plume. An increase in 630.0 nm emission intensity is noticed in zenith observation corresponding to the trough in the bottomside structure around 20:45 IST which is evident in figure 3.7c. Depletion and enhancement in 630.0 nm zenith intensity around 21:45 IST and 22:00 IST respectively are observed where there are crest and trough in the bottomside structure respectively. No discernible response is observed in 777.4 nm intensity variation corresponding to ESF structures (Figure 3.7d).

3.4.4 28 March, 2003

Figure 3.8 depicts another case of ESF event on 28 March, 2003. A large scale bottomside structure with a flat crest region around 20:15 IST is observed in figure 3.8a. Couple of plume structures are also seen to override the bottomside structure during 20:00-20:20 IST. Figure 3.8b reveals the predominantly downward velocity in the bottomside as well as in the plume structures. A steep increase in intensity is observed in the temporal variation of 630.0 nm intensity (Figure 3.8c). However, signatures of plume structures are recorded only in zenith 777.4 nm intensity variations $\sim$20:00 IST. Corresponding to small patches between 22:00 to 23:00 IST, irregular variations are observed in 630.0 nm zenith

intensities.

3.4.5 12 February, 2005

Figure 3.9 depicts an ESF event on 12 February, 2005 wherein two vertically erect structures extending from ∼200 km to ∼425 km are observed in RTI map. Radar data are not available after 22:00 IST on this night. It is interesting to note that the velocities inside the first structure are predominantly downward barring a small region wherein the velocities are upward. The vertical airglow emission corresponding to this structure clearly reveals an enhancement in 630.0 nm and possibly so in 777.4 nm. This serves as a clear example for a plasma enhancement structure extending upto 450 km. The second structure was broader and the velocities were predominantly upward with corresponding decrease in 630.0 nm intensity over zenith. The signature for this structure in 777.4 nm is not clear. The fluctuations observed in 630.0 nm intensity after ∼22:00 IST are difficult to characterize owing to the absence of radar data.

3.4.6 6 March, 2005

Another ESF event obtained on 6 March, 2005 is depicted in Figure 3.10. A bottomside undulation followed by a plume structure at around 23:00 IST were observed on this night. The velocities inside this plume structure are predominantly upward. The airglow intensity variations in 630.0 nm and 777.4 nm emissions over zenith record unambiguous signatures of plasma depletion around 23:00 IST. The slant columnar intensity variations do not record signatures corresponding to vertically erect depletion. Interestingly, the slant columnar intensity of 777.4 nm depicted in 3.9d is found to be less in comparison with the zenith intensity throughout the period till 23:00 IST. Further, the structure recorded between 20:00-22:00 IST does not reveal corresponding signatures in 630.0 nm while the 777.4 nm intensity show a broad minimum. The height integrated depletion and enhancement did not probably leave any signature in 630.0 nm.

3.4.7 7 February, 2005

Figure 3.11 depicts another special event of ESF observed on 7 February, 2005. During initial phase (20:00 to 20:45 IST), both bottomside structures and a plume event is observed in the radar map. Correspondingly, the airglow intensities in 630.0 nm and 777.4

nm emission lines over zenith reveal increase and decrease in intensity. After 20:45 IST, the bottomside structures moved well beyond the 630.0 nm emission layer encompassing the altitude region around 400 km.

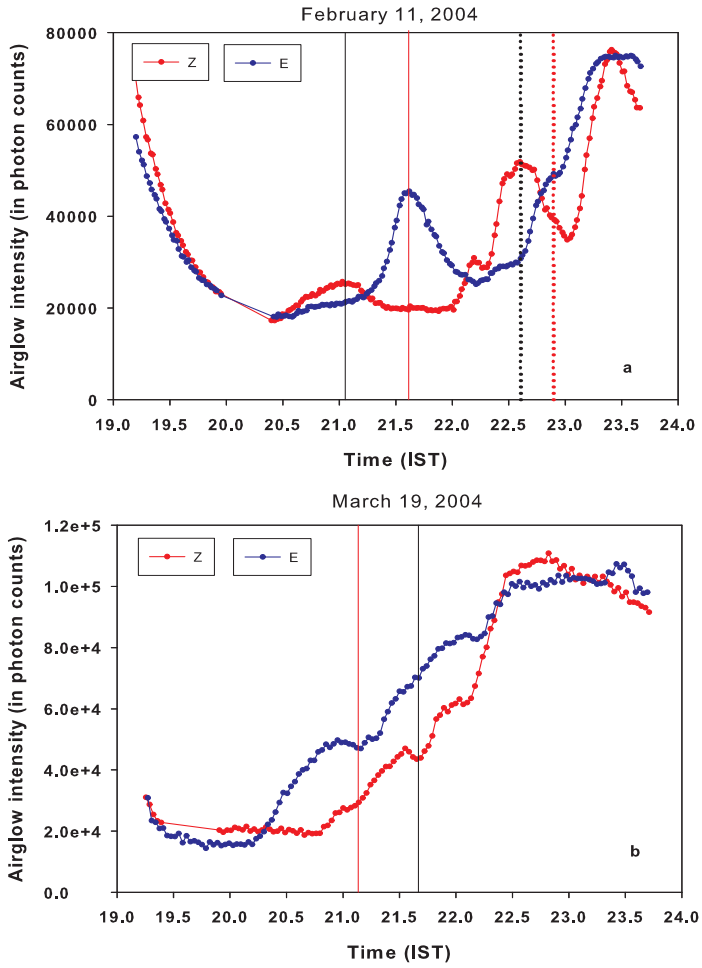

Figure 3.4: Temporal variations of 630.0 nm airglow intensity over zenith (red line) and 45^o east (blue line) on (a) 11 February, 2004, and (b) 19 March, 2004. Points of mutual correspondence are marked by colored vertical lines. Note that, in general, zenith variations precede the variations over eastern direction on 11 February, 2004 indicating an eastward trace velocity of the background plasma. On the other hand, zenith variations seem to succeed the variations over eastern direction till 22:00 hr on 19 March, 2004 indicating an westward movement of background plasma.

Correspondingly, the zenith emission intensities in 630.0 nm and 777.4 nm reveal flat and oscillatory responses in them. However, the slant columnar intensity in 630.0 nm emission revealed a slight enhancement corresponding to this bottomside structure. Around 23:30

Table 3.1: Trace velocities calculated during ESF periods

Date	Time in hr	Trace velocity m/s
11 February, 2004	21.03-21.58	126.26
	22.59-22.94	198.41
19 March, 2004	21.65-21.16	-141.72
21 March, 2004	21.05-21.85	86.81
	21.8-22.8	69.44
07 February, 2005	20.54-21.35	85.73
	22.0-22.4	173.61
	22.85-23.2	198.41
12 February, 2005	21.35-21.95	115.74

P. S. Note that 45^o elevation of the mirror means spatial coverage of 250 km.

IST, a plume structure with corresponding to decreases in 630.0 nm and 777.4 nm is recorded.

3.4.8 6 February, 2005

Figure 3.12 depicts yet another special event of ESF observed on 6 February, 2005. Comb-like structures whose altitude extents are well below 400 km are observed by the radar. The velocities inside these structures are predominantly downward. The temporal correspondence with 630.0 nm airglow intensity reveals that enhancement peaks represent most of the comb-like structures while the trough in 630.0 nm intensity variations corresponds to lack of structures as revealed by the radar map. The intensity variations in 630.0 nm registers comb-like ESF structures while 777.4 nm intensity variations do not record such variation. However, a broad enhancement observed in 777.4 nm intensity variation around 20:15-20:30 IST over zenith. As the F layer peak around 21:00-22:00 hr IST was found to be less than 350 km, enhancement in 777.4 nm intensity is possible only during that time in the presence of structures within 350 km.

3.4.9 20 March, 2004

Figure 3.13 depicts two isolated ESF structures and a small patch which are observed around 22:00 IST on 20 March, 2004 along with corresponding airglow observations. An enhancement is observed corresponding to the second ESF structure in 630.0 nm airglow intensity. Signatures in airglow intensities corresponding to other ESF structures are ambiguous.

3.4.10 29-30 January, 2006

Figure 3.14 depicts the coordinated measurement on ESF event during 29-30 January, 2006. Due to technical reasons, airglow measurement on 777.4 nm is not available on this night. The onset of ESF $\sim$2200 km was delayed during this event which persisted well beyond midnight till 02:00 IST on the next day. The optical observation corresponding to the ESF structures during the interval 22:00-26:00 (04:00 hr of the next day) IST are presented. The figure reveals oscillatory features in 630.0 nm airglow intensity which only corresponds to bottomside structures.

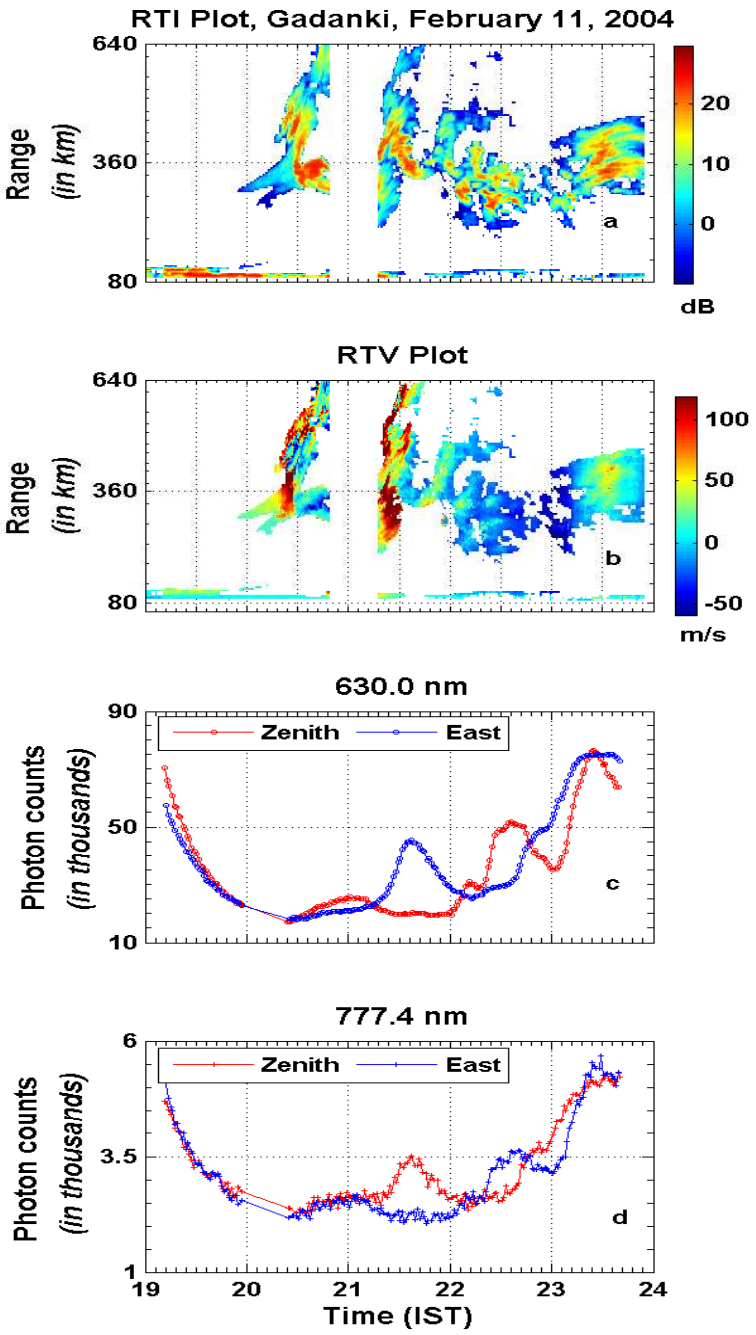

Figure 3.5: Composite plots of temporal variations of (a) Range and Intensity (RTI), (b) Range and Velocity (RTV), (c) 630.0 nm airglow intensity over zenith (red) and 45^o elevation in the eastern direction (blue), and (d) 777.4 nm airglow intensity variations over zenith (red) and 45^o elevation in the eastern direction (blue) on 11 February, 2005. The colour codes in (a) and (b) denote the intensity and the velocity respectively.

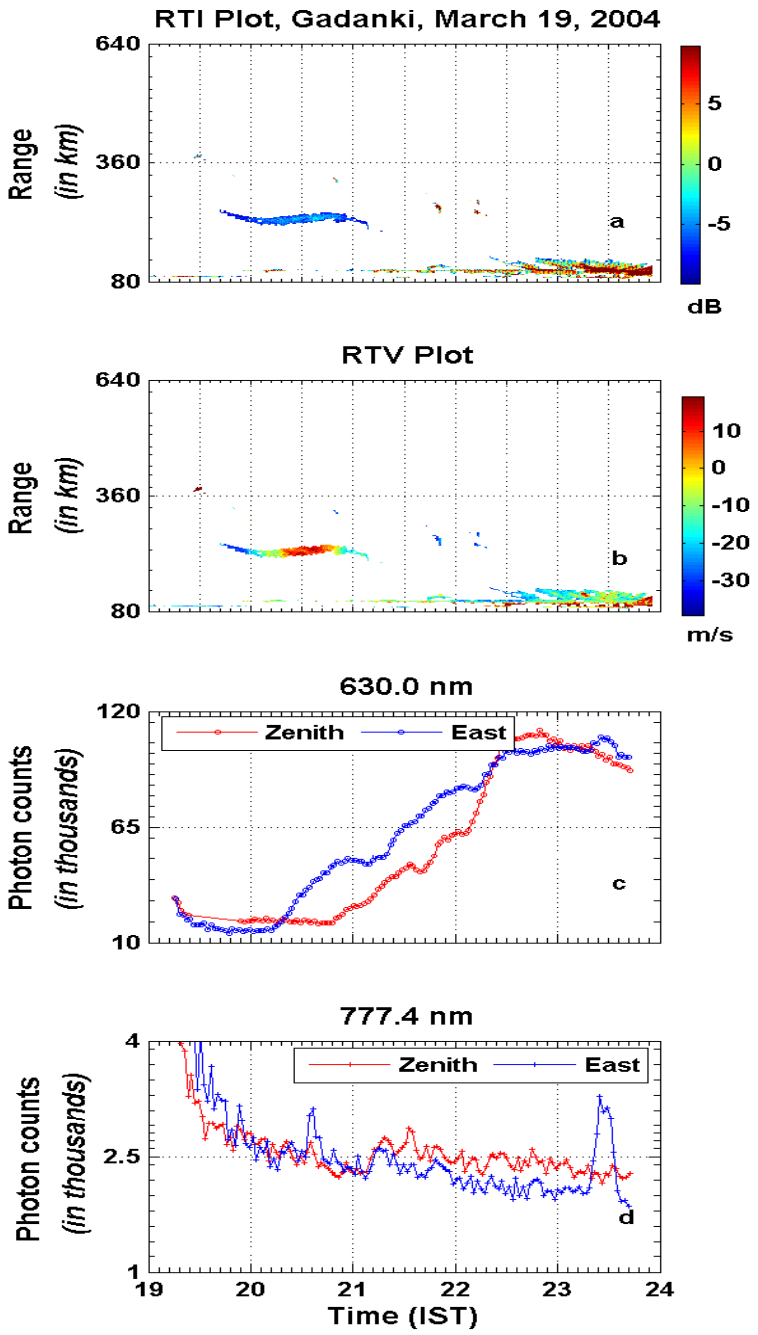

Figure 3.6: Same as Figure 3.5 but on 19 March, 2004.

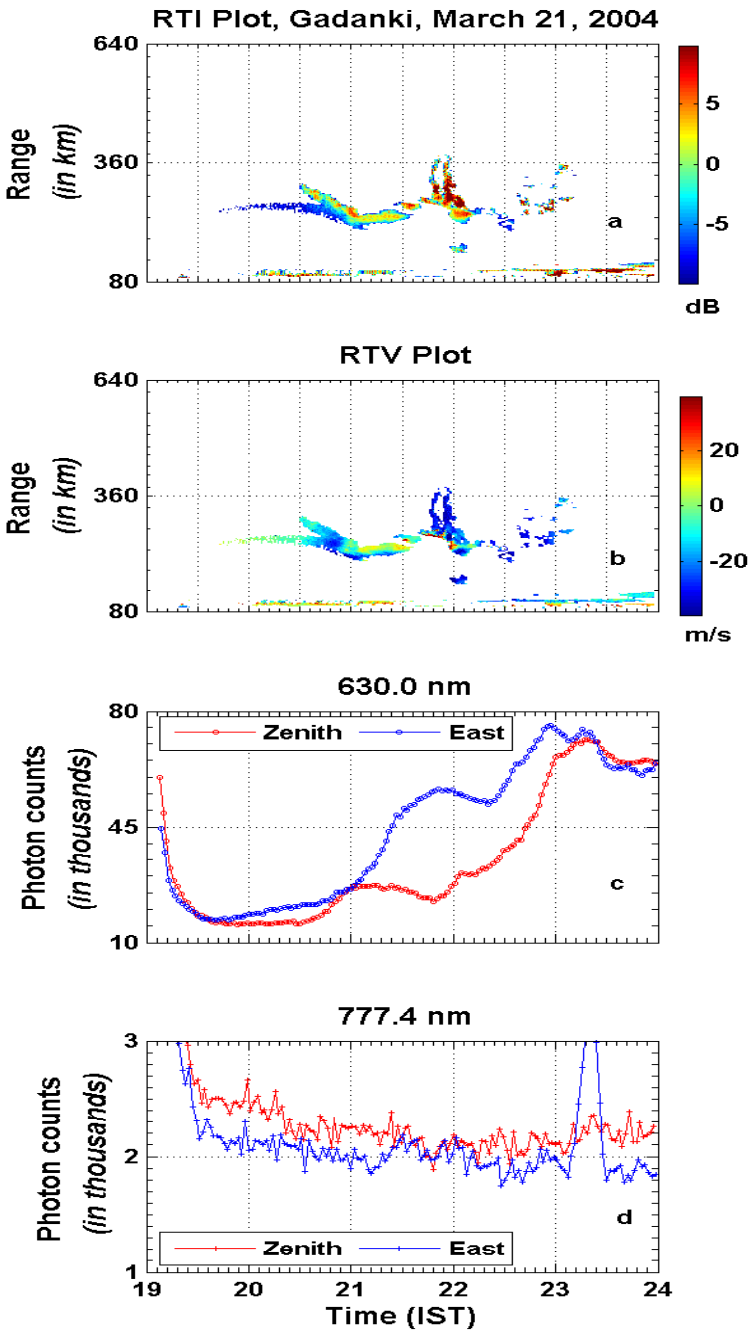

Figure 3.7: Same as Figure 3.5 but on 21 March, 2004.

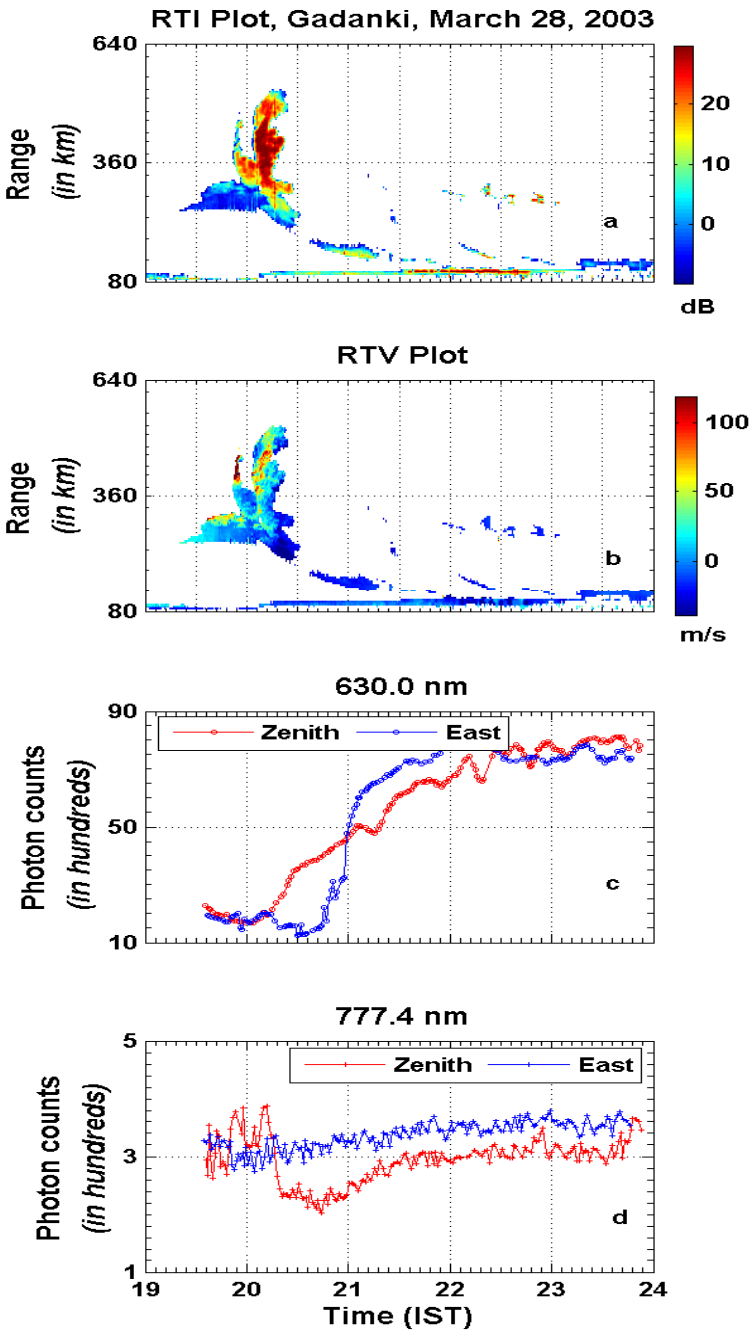

Figure 3.8: Same as Figure 3.5 but on 28 March, 2003.

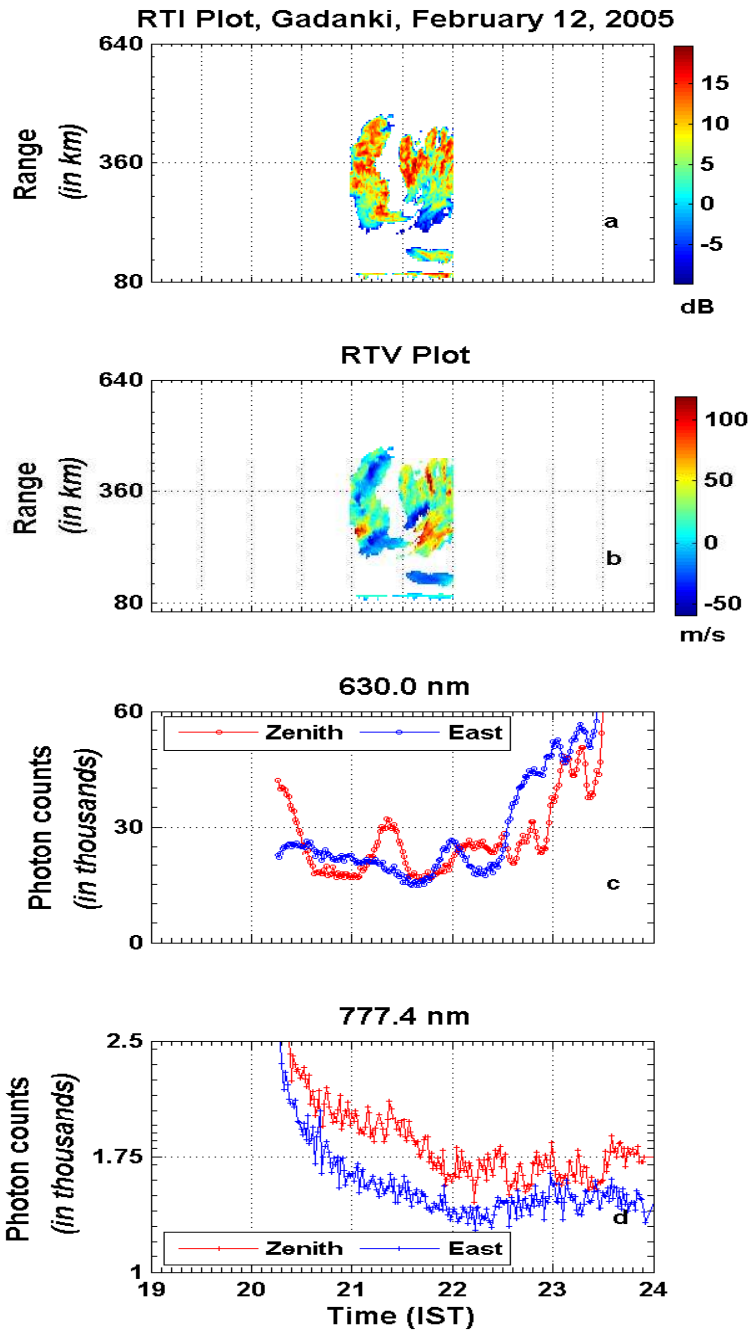

Figure 3.9: Same as Figure 3.5 but on 12 February, 2005. Radar data are not available after 22:00 IST on this night.

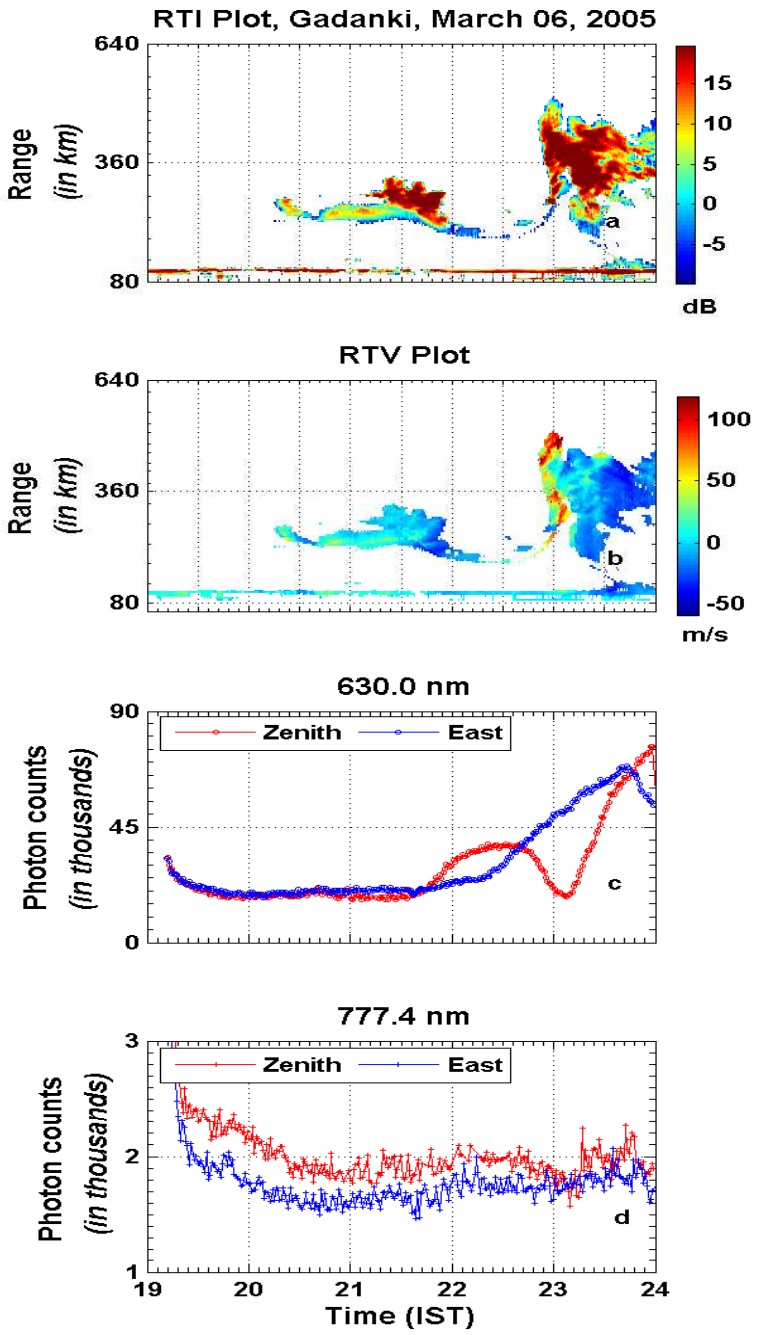

Figure 3.10: Same as Figure 3.5 but on 6 March, 2005.

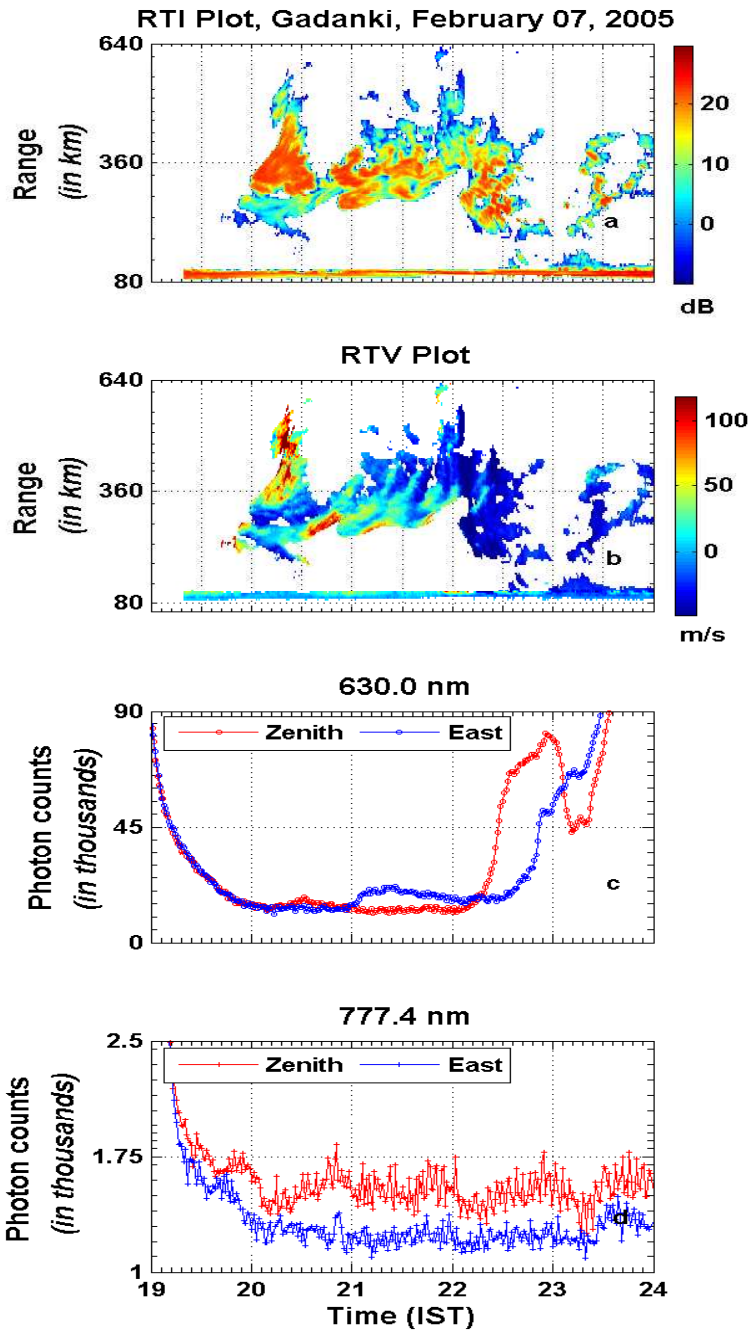

Figure 3.11: Same as Figure 3.5 but on 7 February, 2005.

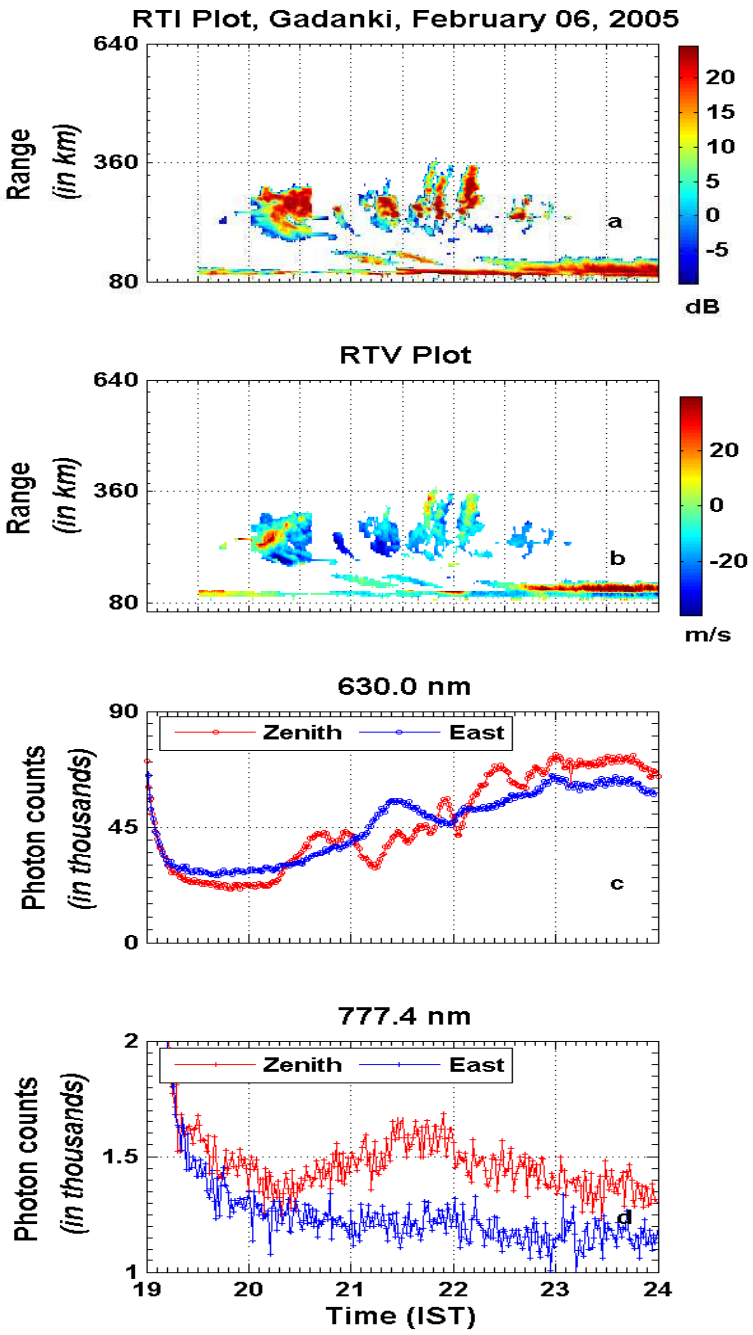

Figure 3.12: Same as Figure 3.5 but on 6 February, 2005.

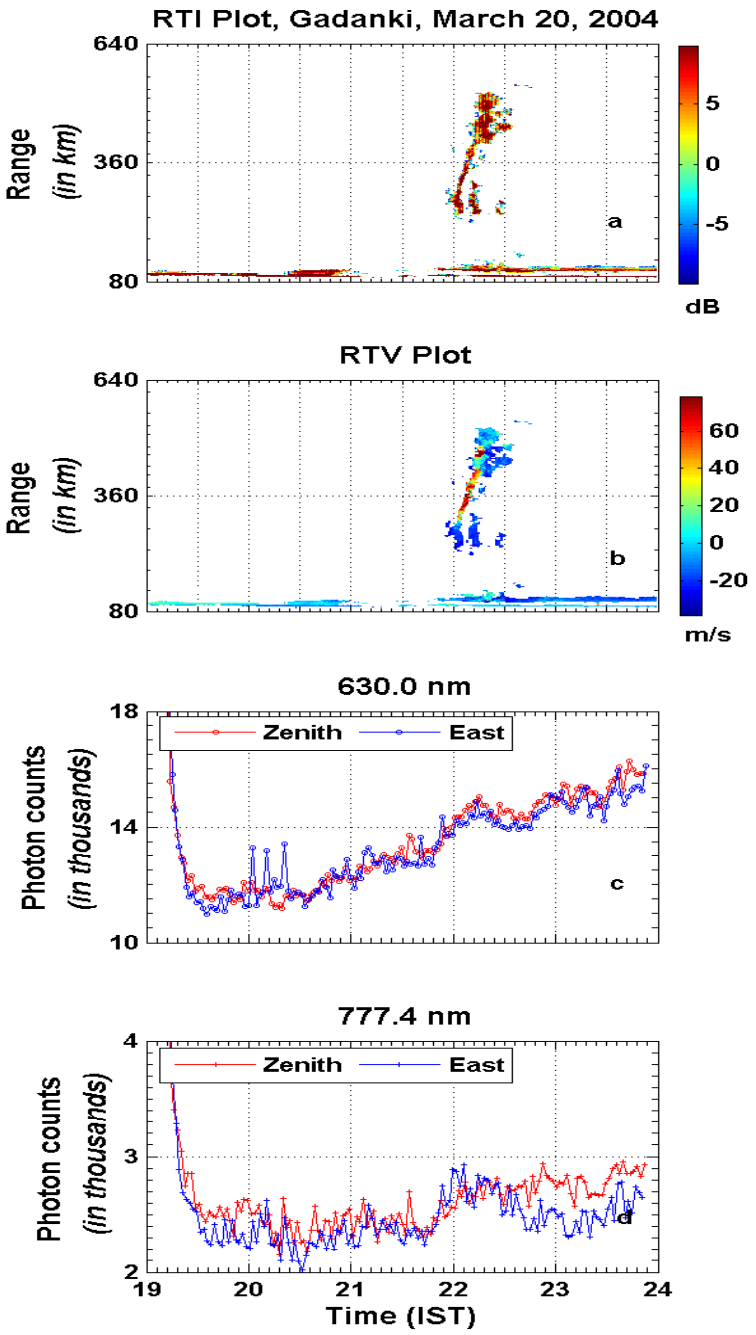

Figure 3.13: Same as Figure 3.5 but on 20 March, 2004.

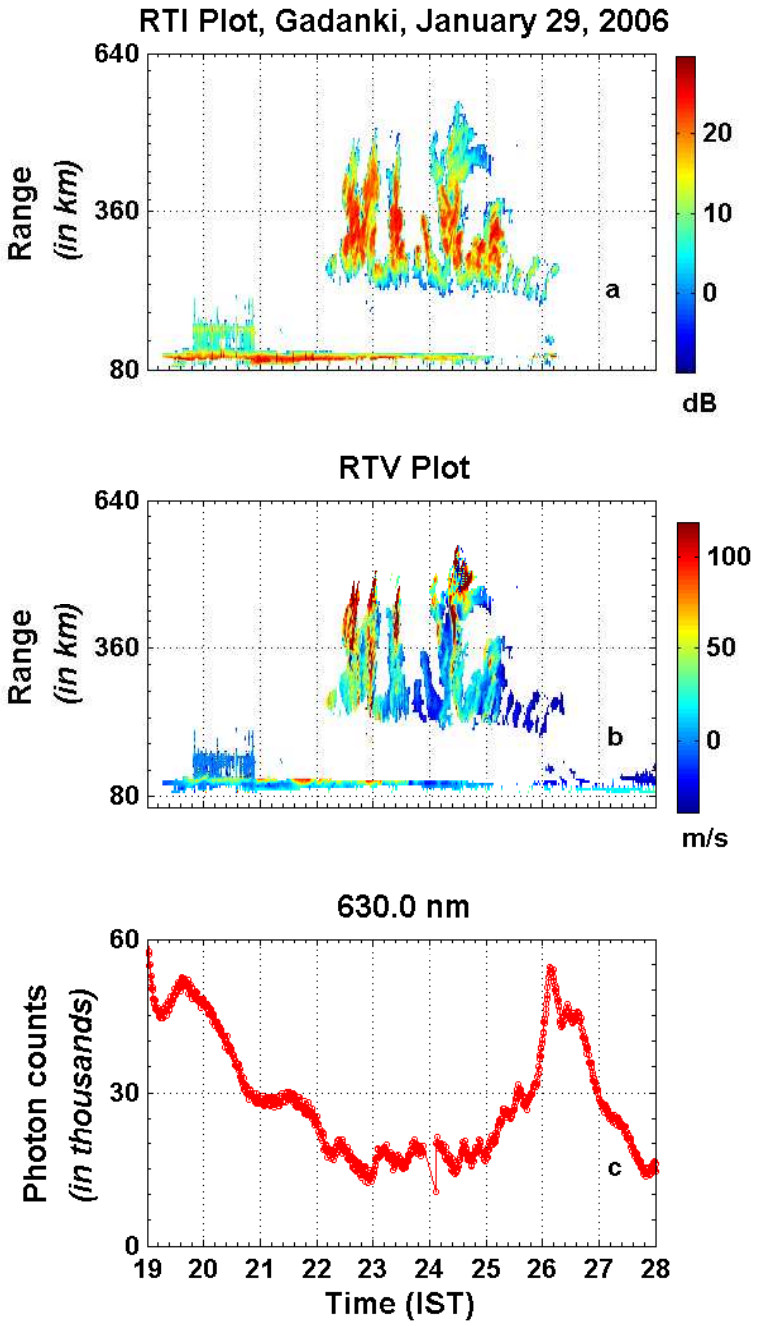

Figure 3.14: Same as Figure 3.5 but on 29-30 January, 2006.

3.5 Discussion on the observational features during 2003-2006

The observations reported in section 3.4 reveal upward moving depletions and downward moving enhancements extending even beyond 350 km altitudes. Earlier simulation analysis [*Sekar et al.*, 2001] brought out the importance of the seeding more than one mode for the generation of plasma enhancement beyond 350 km. The structures depicted in figures

3.5 and 3.8 indicate in support of this simulation as the plume structures ride over a large scale bottomside structures. The enhancement structure in figure 3.9 is also conspicuous.

In the absence of steering facility in VHF radar, it is difficult to decipher the ESF structures observed in RTI maps are due to temporal variations or spatially varying structures moving into the radar field of view by the background zonal wind [*Woodman and LaHoz*, 1976]. Bi-directional airglow measurements can be used to determine the trace velocities of the background ionosphere based on the time differences between the points of mutual correspondence and the spatial separation between two scans at the time of ESF events (see Figure 3.4). On most of the occasions, the polarity of the trace velocity is found to be eastward. However, on 19 March, 2004, the trace velocity is found to be in westward direction till 22:00 IST. This means that the plasma drift in the altitude region of 250-300 km, where the 630.0 nm emission originates, is westward. Above this altitude region, the zonal plasma movement is dictated by F region dynamo mechanism which is governed by zonal neutral wind flow. As the zonal wind direction is determined by thermal gradient, the direction of wind as well as the plasma motion must be eastward during nighttime. Combining these points, it is inferred that a strong shear in the zonal plasma drift might be present on 19 March, 2004 till 22:00 IST. *Sekar and Kelley* [1998], on the basis of numerical simulation investigation, showed that long wavelength ESF structures can be confined to bottomside in a localized region with the combined effects of shear in the zonal plasma drift and nighttime westward electric field. A possible presence of shear in the zonal plasma drift might be one of the possible factors for the bottomside confinement of the ESF structure observed on 19 March, 2004 (see Figure 3.6). Similarly, simultaneous triggering of ESF at two zonally separated location can be identified [see Figure 4.6 in chapter 4] using this type of bi-directional airglow observation.

Another interesting point emerges using bi-directional airglow measurements that the slant columnar airglow intensities, in spite of geometrical advantages (Van Rhijn advantage principle), on occasions, are found to be less than the corresponding zenith observations. This can happen in the presence of depleted ESF structures in off-zenith directions. This is particularly found true in 630.0 nm emission intensities wherein the slant columnar intensities in the presence of ESF structures are found to be less in comparison with the corresponding zenith intensities on several occasions.

3.6 Summary

Narrow band photometric observations on 630.0 nm and 777.4 nm emission lines reveal micro variations during ESF nights in addition to the usual macro variations. Such micro variations are not observed on a non-ESF, geomagnetically quiet nights whereas macro variations are seen on both ESF and non-ESF nights. In addition to the well known anti-correlation between the base height of the F region and the macro variations of thermospheric airglow intensity, the variation of the base height, on occasion, manifest as a bottomside wave like structure. Using coordinated airglow and VHF radar measurements, the micro variations are identified to be due to the plasma structures associated with ESF and found to be in correspondence with the VHF radar plume structures. Further, on some occasions, the VHF radar structures observed well beyond 350 km and moving downward are characterized as plasma enhancements. The observation of enhancement in 777.4 nm airglow intensity which is characterized as plasma enhancement brings out the importance of the multiple modes as seed perturbation in the generation of ESF. It is also indicated that using bi-directional scanning arrangement of the thermospheric airglow emission, the trace velocity of the background plasma can be roughly estimated and the simultaneous occurrence of ESF event over a longitude zone can be identified. In addition to that, it is also found that in the presence of ESF structures, zenith intensity can exceed slant columnar airglow intensity violating Van Rhijn advantage principle.

Chapter 4

Space weather events and ionospheric F region over low latitudes

4.1 Background: Interplanetary electric field and thermospheric airglow emission

During geomagnetic storm events, the low latitude ionosphere, on occasions, is subjected to the interplanetary electric field (IEF) penetrating through the magnetosphere-ionosphere system. Using geomagnetic data from multiple stations and IMP-1 satellite data, *Nishida* [1968] was the first to systematically identify the coherence between the interplanetary magnetic field and the DP2 fluctuations. Thereafter, many important investigations [e.g. *Gonzales et al.*, 1979; *Fejer et al.*, 1979; *Reddy et al.*, 1979; *Kikuchi et al.*, 1996, *Sastri*, 2002; *Kelley et al.*, 2003, 2007; *Huang et al.*, 2007] have revealed the connection between the equatorial and auroral electric field variations during geomagnetically disturbed conditions on the basis of magnetic and radar data obtained simultaneously from multiple stations. Recently, *Kelley et al.* [2003] have quantified the ratio of the dawn-to-dusk component of the IEF to the dawn-to-dusk electric field in the equatorial ionosphere by investigating a long duration electric field penetration event captured by Jicamarca incoherent scatter radar. Although a number of investigations have been carried out to find out the signatures of IEF in the ionospheric F region over latitudes, the effect of IEF on the thermospheric airglow emission over low latitudes has not been reported so far.

OI 630.0 nm airglow photometry has long been recognized as a diagnostic tool in the investigation of ionospheric F region embedded in the terrestrial thermosphere. The F re-

gion processes have been studied using both ground based [e.g. *Kulkarni and Rao*, 1972] and satellite borne broad band photometers [e.g. *Chandra et al.*, 1973s]. As of today, characteristic signatures in 630.0 nm nightglow intensity have been obtained corresponding to the F layer height variations [*Barbier*, 1959], nighttime reversal of the equatorial plasma fountain [e.g. *Sridharan et al.*, 1993], the midnight temperature anomaly [*Herrero and Meriwether*, 1980] and plasma depletions [e.g. *Sobral et al., 1980*; *Mendillo and Baumgardner*, 1982] or enhancements [*Sekar et al.*, 2004] associated with Equatorial Spread F (ESF) events.

It is well known that the equatorial ionospheric electric fields and the F region layer height get altered due to the penetration of IEF into low latitude ionosphere during disturbed geomagnetic conditions. As the OI 630.0 nm airglow emission is anti-correlated with the F region layer height, it is generally expected that the effect of IEF may get registered in airglow intensity fluctuations. However, no direct evidence is available in the literature. This is probably due to broad-band photometers employed by the earlier workers. Furthermore, the relationship between the fluctuating components in airglow intensity and the F region layer height variation is not known. In this chapter, an evidence is provided that the quasi-periodic intensity fluctuations observed in OI 630.0 nm airglow over low latitude on a disturbed day are due to the fluctuations in the IEF.

4.1.1 Observations and Results

Coordinated campaign involving the MST radar and the multiwavelength, narrow band, scanning photometer was conducted during 11-22 February, 2004. Optical observations pertaining to a geomagnetically disturbed night(12 February, 2004; A_P=30) and a quiet night(20 February, 2004; A_P=4) are reported in this section of this chapter.

Photometric and ionosonde measurements on 12 February, 2004

Figure 4.1 consists of three subplots pertaining to the observations on 12 February, 2004. The abscissae for all the subplots are expressed in time in IST (IST = UT + 5.5 hr). The topmost subplot (Figure 4.1A) depicts the OI 630.0 nm nightglow intensity (maximum measurement error in airglow is $\sim\pm$400 counts) over Gadanki and the F layer peak height (h_PF_2) variations (maximum uncertainty in the height measurements is $\sim$5 km) with 15 minutes temporal resolution over SHAR. The large scale airglow intensity variation on this night is characterized by its monotonic increase till $\sim$21:30 IST followed by

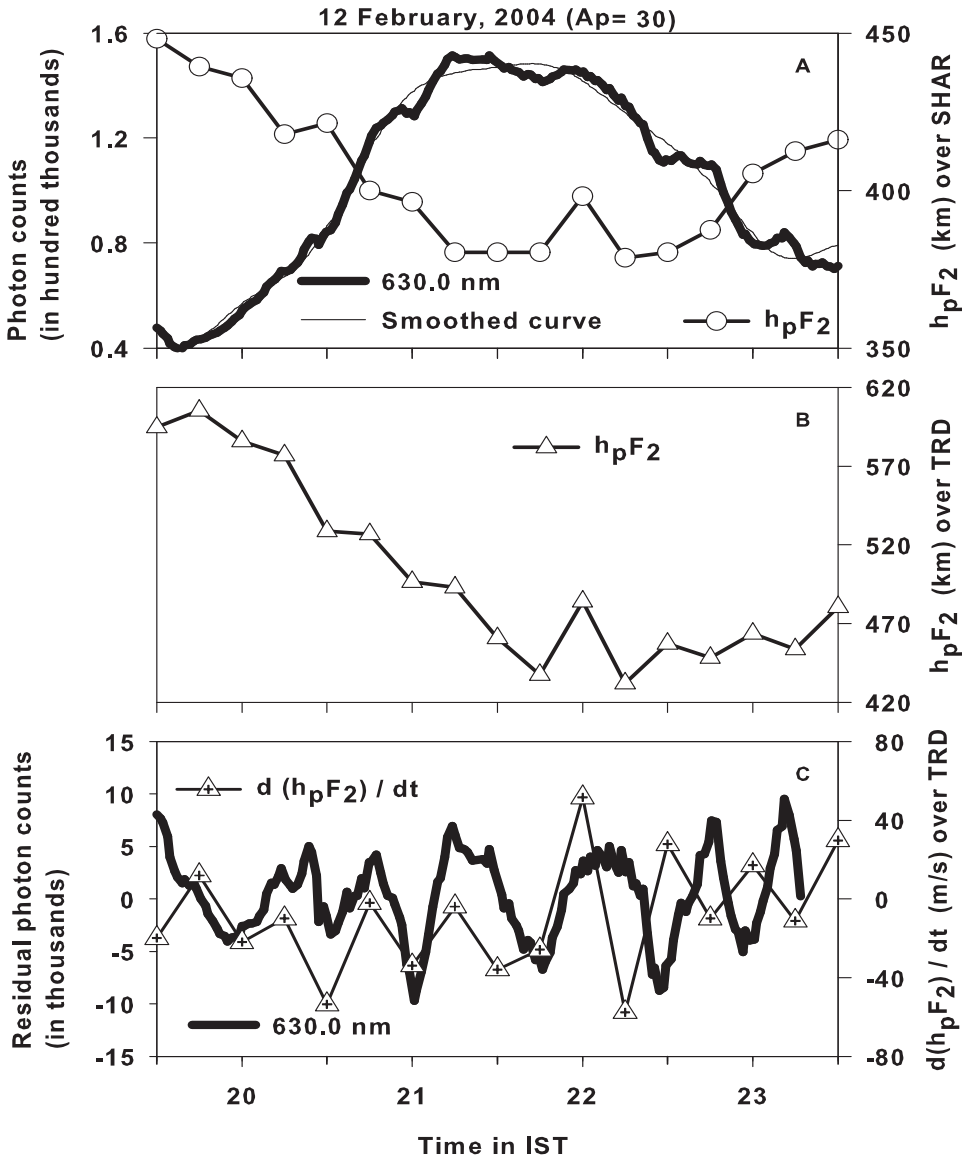

Figure 4.1: (A) 630.0 nm airglow intensity variations over Gadanki along with the h_PF_2 variations over SHAR on a geomagnetically disturbed night (12 February, 2004; A_P=30). The maximum measurement error in airglow is $\sim\pm$400 counts. Note the presence of small scale airglow intensity variations on this night. Notice also the smoothed curve which is generated by taking suitable running average of the data points so that it is devoid of the small-scale intensity fluctuations. This curve is used to extract the intensity residuals. (B) h_PF_2 variations over Trivandrum (TRD) during the same interval. Uncertainty in the height measurements is $\sim$5 km, (C) Residual airglow intensity variation along with the time rate of change of h_PF_2 over TRD. The maximum propagation error in dh_PF_2/dt is $\sim\pm$6 m/s.

gradual decrease till the end of the observation. Small scale (T_s) intensity fluctuations in the range of 0.25 hr$< T_s \leq$ 1.0 hr are discerned to be superimposed on the large scale variation at regular intervals during the period of observation. The peak to peak amplitude of small scale airglow intensity fluctuations varies from 8-10 $\%$ of the background val-

ues which corresponds to 8 to 10 Rayleighs considering a typical value for the nocturnal 630.0 nm airglow intensity to be $\sim$ 100 Rayleighs. In order to unambiguously detect such intensity fluctuations, narrow band photometry is necessary as that curtails the random noise background and, therefore, increase the signal to noise ratio. The h_PF_2 variation over SHAR, on the otherhand, was marked by monotonic decrease till $\sim$21:30 IST followed by steady increase till midnight. The smoothed airglow intensity curve plotted in Figure 4.1A (constructed by taking running average) which is devoid of the small scale intensity fluctuations, is used to filter out the residual smaller scale fluctuations in photon counts which is plotted in Figure 4.1C. The intermediate subplot (Figure 4.1B) depicts the h_PF_2 variations over Trivandrum (TRD)during the same interval. It is noticed that the h_PF_2 variations over SHAR and TRD are, in general, similar on this night barring the rate of increase during 22:30-23:30 IST. Figure 4.1C illustrates the temporal variation of the residual photon counts, obtained after detrending the large scale airglow intensity variation depicted in Figure 4.1A, along with the time rate of changes in h_PF_2 (dh_PF_2/dt) over TRD. It is noticed that the variabilities in dh_PF_2/dt (maximum propagation error in dh_PF_2/dt is $\sim\pm$6 m/s) over TRD during 19:45-23:15 IST do have their counterparts in the temporal variabilities in the residual intensity variations. The time difference between the crests and troughs that appear to be mutually correspondent in the two time series is almost close to zero before $\sim$22:15 IST. However, during 22:15-23:15 IST, oscillations in dh_PF_2/dt over TRD seem to precede the airglow intensity oscillations by $\sim$15 minutes which is of the order of the resolution of the available ionosonde data. Figure 4.1A reveals that the residual airglow intensity fluctuations on this nights are caused by electric field fluctuations.

Photometric and ionosonde measurements on 20 February, 2004

Figure 4.2 comprises of three subplots (similar to those of Figure 4.1) corresponding to 20 February, 2004. Figure 4.2A depicts the airglow intensity variation along with the h_PF_2 variations over SHAR . This subplot also reveals post-evening increase in the airglow intensity (maximum measurement error in airglow is $\sim\pm$450 counts) till $\sim$21:30 IST followed by decrease in the intensity similar to Figure 4.1A. However, small scale intensity fluctuations observed on 12 February are absent on this night. The large scale h_PF_2 variation over SHAR was also marked by the continual descent upto $\sim$21:30 IST followed by slow, gradual ascent similar to Figure 4.1A. However, subplots 4.2A

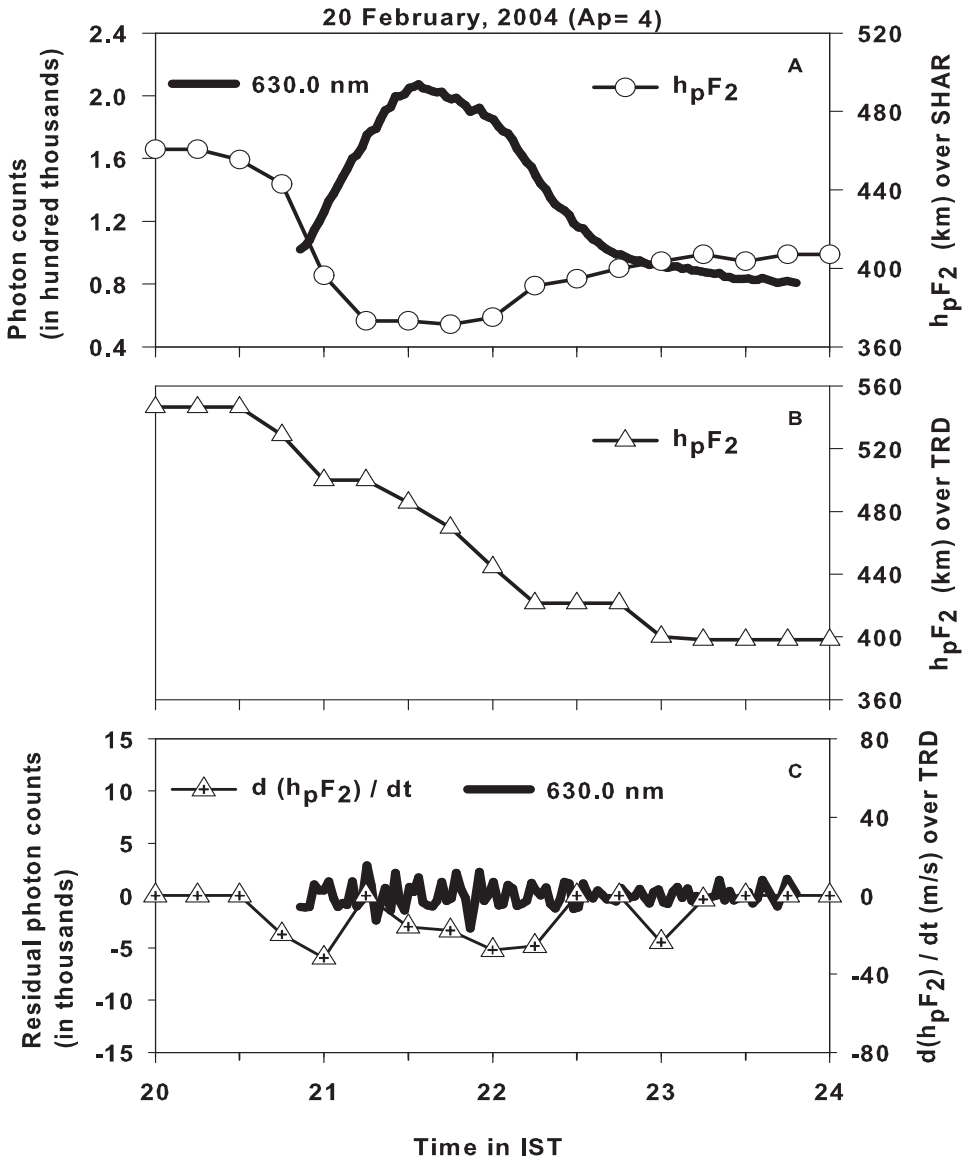

Figure 4.2: (A) 630.0 nm airglow intensity variations over Gadanki along with the h_PF_2 variations over SHAR on a geomagnetically quiet night (20 February, 2004; A_P=4). The maximum measurement error in airglow is $\sim\pm$450 counts. Note the absence of small scale airglow intensity variations on this night, (B) h_PF_2 variations over Trivandrum (TRD) during the same interval, (C) Residual airglow intensity variation along with the time rate of change of h_PF_2 over TRD.

and 4.2B reveal that large scale h_PF_2 variations over SHAR and TRD are different on this night unlike Figure 4.1. Figure 4.2C shows that, unlike in Figure 4.1C, the temporal variations of the residual photon counts (mostly statistical fluctuations) are uncorrelated with dh_PF_2/dt over TRD.

In order to verify that the fluctuations in h_PF_2 and airglow intensity during 19:45-23:15 IST on 12 February, 2005 are due to penetrating disturbance electric field event, the dawn-to-dusk component of IEF was calculated based on the solar wind velocity and interplanetary magnetic field values measured by ACE satellite located at the Libration point

L1($\sim$1.41$\times$10^{6}km from earth). It is also important to calculate reasonably accurately the time delays which separate the satellite and ionospheric observations [for a comprehensive discussion, see *Ridley et al.*, 1998]. In the subsequect section, the methodology that has been adopted in the calculation of propagation lag is discussed.

Time lag between ionospheric and ACE satellite measurements

The time lag between the satellite observations made at L1 point and ionospheric observations, comprises of three components. The travel time of the solar wind from the spacecraft to the subsolar bow shock (t_1), propagation time from the bow shock to the magnetopause (t_2), and the Alfven transit time (t_3) along magnetic field lines from the subsolar magnetopause to the ionosphere. The magnetopause stand-off distance (X_{mp}), for the given period, is calculated based on the simple pressure balance equation between the solar wind dynamic pressure and the magnetospheric pressure [e.g. *Roelof and Sibeck*, 1993] using the proton number density (adjusted for helium content, noting the mass factor of 4) in the solar wind and the solar wind bulk velocity v (during this period, v varied from 645 km/s to 750 km/s). X_{mp} is found to vary between $\sim$10.92R_E (R_E, the radius of the earth, is taken as 6375 Km) to $\sim$9.7R_E during the interval under consideration here. The solar wind advection time t_1 is then calculated using the formula described by *Lester et al.*, [1993].

$$t_1 = \frac{X_{sat} - X_{bs} + L\tan\phi}{v} \tag{4.1}$$

where X_{sat} is the geocentric upstream distance of the spacecraft, X_{bs} is the geocentric distance to the subsolar bow shock and L is the orthogonal distance of the spacecraft from the sun-earth line. This calculation is based on the assumptions that the earth-bound solar wind upstream of the bow shock is not accelerated, the solar wind "phase front" is at angle ϕ (lying within $\pm 45^o$) with the sun-earth line and the "phase front" is linear over scale sizes greater than L and the cross section of the magnetosphere. Using the empirical model of *Peredo et al.* [1995], *Khan and Cowley* [1999] comprehensively analyzed the observed shock locations and found that a typical bow shock distance, X_{bs}, is, in general, 1.46 times the distance of the subsolar magnetopause. Using this multiplicative factor, X_{bs} is found to vary between $\sim$16.59R_E to $\sim$14.56R_E during the interval under consideration. *Khan and Cowley* [1999] also showed that the magnetosheath transit time t_2 can be derived using the gas dynamic model of *Spreiter and Stahara* [1980] as follows.

$$t_2 = \frac{1.66X_{mp}}{(v-72)}\ln\frac{v}{72} \tag{4.2}$$

It is to be noted here that t_2 can also be deduced from the model of *Spreiter and Stahara* [1980] by dividing the magnetosheath thickness with an average magnetosheath velocity (v_{avg}) which is assumed to fall off in an approximately linear fashion from $v_{avg}/4$ at the bow shock to zero at the magnetopause [e.g. see *Lester et al.*, 1993]. It is verified that the values of t_2 obtained by both the methods agree well in the present case.

The average Alfven transit time, t_3, is taken as 2 minutes [*Khan and Cowley*, 1999]. The total time lag from the ACE spacecraft to the ionosphere is thus calculated by adding t_1, t_2 and t_3. Each time value in the IEF time series, derived based on ACE observations, is then shifted by an amount equal to the sum of corresponding t_1, t_2 and t_3. The total time lag, in the present case, is found to range from $\sim$48.7 minutes to $\sim$42.1 minutes during the interval under consideration. The sources of uncertainties involved in this type of calculation is comprehensively discussed by *Ridley et al.* [1998] and *Khan and Cowley* [1999]. It is found that the maximum error in the present calculation is of the order of 5 minutes.

Inter-comparison of the time-delayed IEF$_y$, ionosonde and photometric measurements on 12 February, 2004

Since the average temporal resolution of the airglow data is $\sim$120s in comparison with the ACE data which, in the present case, are obtained at an average resolution of $\sim$64s, the Y-component of IEF, calculated from the ACE data, is first subjected to a 2-point moving average scheme (low pass filtering). Thereafter, each IEF$_y$ datum point is time shifted by the corresponding lag time from L1 to ionosphere. The filtered and time-shifted IEF$_y$ values are then plotted in Figure 4.3A. The variation in IEF$_y$ is subsequently subjected to Fourier domain filtering in which the frequency components less than 0.5 cycles/hr (periods $>$ 2 con) are filtered off. This procedure automatically takes care of the detrending of the IEF$_y$ data. The detrending of IEF$_y$ data prevents leakage of spectral powers from the low frequency components (frequency components less than 0.5 cycles/hr). Since the resolution of the h$_P$F$_2$ data is 15 minutes, frequency components more than 4 cycles/hr (periods $<$ 15 minutes) in IEF$_y$ are also eliminated for useful comparison. The filtered data are subsequently reconstructed in the time domain. The resultant IEF$_y$ residual time series, thus obtained, is compared with the dh$_P$F$_2$/dt variations over Thumba as well as with the residual photon counts in the subplot 4.3B and 4.3C respectively. It is noticed that the IEF$_y$ residuals agree reasonably well with dh$_P$F$_2$/dt variations as well as with

residual counts except mainly $\sim$ 20:45 and $\sim$ 22:00 IST.

As the time series of residual airglow and IEF$_y$ residual are not strictly evenly sampled, a special harmonic analysis [*Schulz and Stattegger*, 1997] which can handle unevenly sampled data is followed to obtain frequency components. The harmonic analyses generate normalized periodograms from the residual (not normalized) time series. The spectral power contained in each spectral element is normalized with respect to the total power contained in all the spectral elements taken together. This procedure makes the relative distribution of the spectral power independent of the spectral windowing (to avoid spectral leakage) used in the algorithm. Both the normalized periodograms are depicted on the same scale in the subplot 4.3D. "Significant" frequency components in both the time series exceed the critical level (marked by dotted lines) determined by Fisher's test. Therefore, subplot 4.3D reveals the relative importance of each "significant" frequency component in the two time series. It is noticed from subplot 4.3D that the residuals of airglow counts and the IEF$_y$ both have "significant" and common frequency components (marked by hatch in figure 4.3D) at $\sim$ 1 cycle/hr (period $\sim$ 1.0 hr) and $\sim$ 2 cycles/hr (period $\sim$ 0.5 hr). Harmonic analysis of the evenly sampled, detrended (allowing the frequency pass-band 4.0-0.5 cycles/hr only) dh$_P$F$_2$/dt time series (shown in figure 4.3B) is also carried out using a standard Fast Fourier Transform (FFT) algorithm and the power spectral densities (PSD, sum squared amplitudes) are shown as an inset of figure 4.3D for comparison. As the number of dh$_P$F$_2$/dt data points are very limited, reliable estimation of the critical level is not possible. Nevertheless, it is clear that the frequency components close to 1 cycle/hr and 2 cycles/hr are also present in the dh$_P$F$_2$/dt time series.

In order to find out whether the residual airglow intensity fluctuations are causally related to the fluctuations in IEF$_y$, a cross spectrum analysis is performed between the two residual time series (plotted and compared in figure 4.3C) using a standard methodology [*Schulz and Stattegger*, 1997]. Cross spectrum analysis generates coherency and phase spectrum from the two residual (not normalized) time series. It is found that substantial coherency between the two time series exist (see figure 4.3E) at frequencies $\sim$3.7 cycles/hr (period $\sim$ 0.27 hr), $\sim$2.8 cycles/hr (period $\sim$ 0.36 hr), $\sim$2 cycles/hr (period $\sim$ 0.5 hr) and $\sim$1 cycle/hr (period $\sim$ 1.0 hr). However, coherency at frequencies $\sim$3.7 cycles/hr, $\sim$2.8 cycles/hr are neglected owing to the absence of simultaneous "significant" spectral peaks in both the time series (see the normalized periodograms in figure 4.3D). High

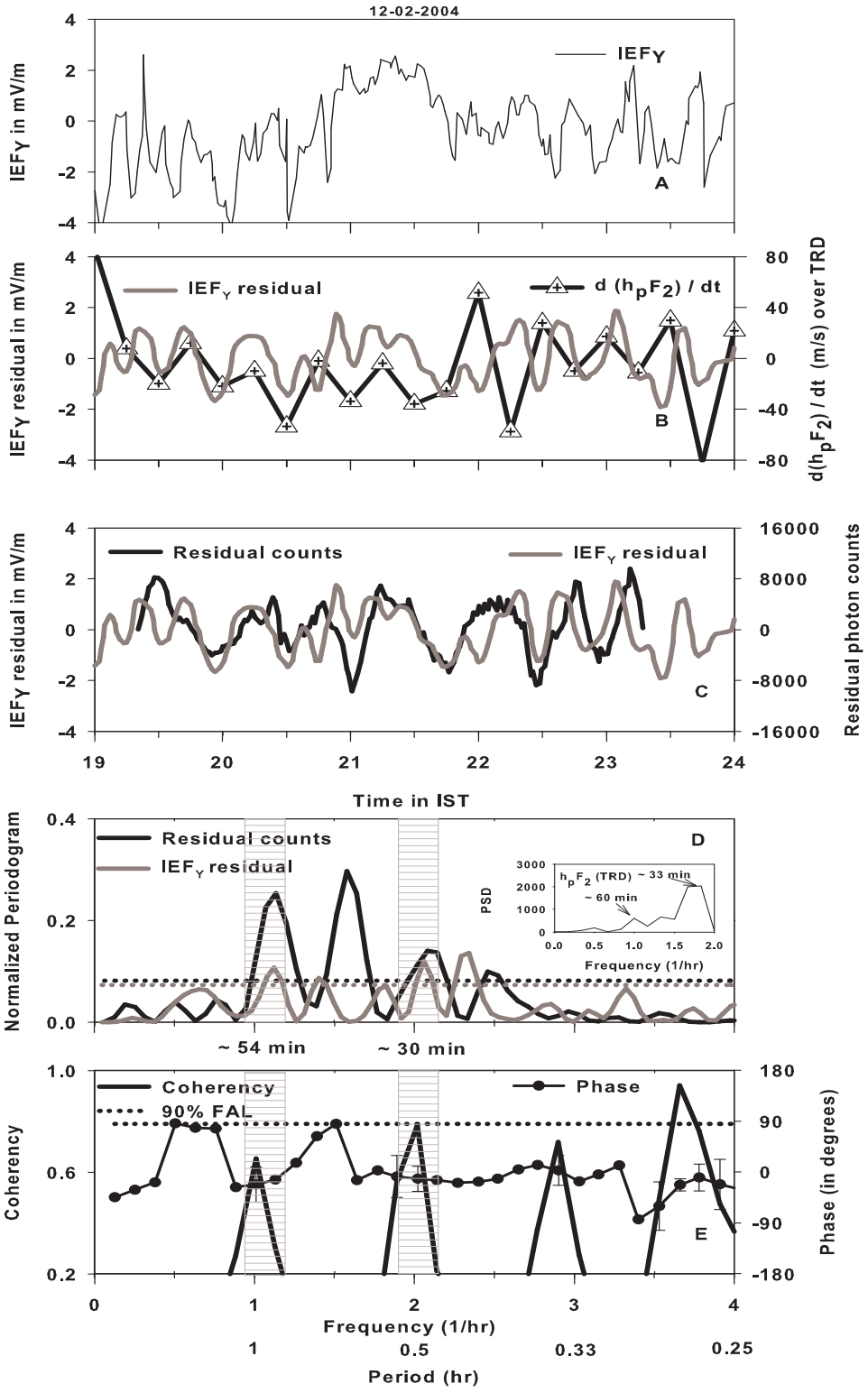

Figure 4.3: (A) The time shifted (by the travel time from the first Lagrangian point of the sun-earth system to ionosphere) variations in the Y component of the Interplanetary Electric Field (thin black line) on 12 February, 2004, (B) comparison between the time rate of change of h_PF_2 over TRD (black line with legends) and the IEF_y residuals (grey line), (C) comparison between the residual airglow intensity variations (black line) and the IEF_y residuals (grey line), (D) harmonic components in the airglow (black line) and the IEF_y residuals (grey line). Superimposed horizontal lines in black and grey denote the critical levels determined by the Fisher's test for the two time

series. The power spectral densities (PSD) of the detrended dh_PF_2/dt variations are also shown as an inset. Notice the simultaneous presence of $\sim$ 2 cycles/hr (period $\sim$0.5 hr) and $\sim$1 cycle/hr (period $\sim$1.0 hr) frequency component in residual IEF_y, airglow (marked by hatch). Note also the presence of the same frequency components in dh_PF_2/dt (marked by arrow) time series, (E) coherency and phase spectrum for the residual IEF_y, airglow time series. Dotted line indicates 90% false alarm level for the coherency spectrum. Note high degree of coherence at frequencies $\sim$3.7 cycles/hr (period $\sim$ 0.27 hr), $\sim$2.8 cycles/hr (period $\sim$ 0.36 hr), $\sim$2 cycles/hr (period $\sim$ 0.5 hr) and $\sim$1 cycle/hr (period $\sim$ 1.0 hr). Coherency at frequencies $\sim$3.7 cycles/hr and $\sim$2.8 cycles/hr are neglected owing to the absence of simultaneous "significant" spectral peaks in both the time series. The frequency components at $\sim$2 cycles/hr and $\sim$1 cycle/hr (marked by hatch) are characterized by high coherency and stable phase relationship.

degree of coherence (close to the false alarm level at 90%) is found (marked in figure 4.3E) especially for the frequency component at $\sim$2 cycles/hr. Coherency at the frequency component $\sim$1 cycle/hr is also found (marked in figure 4.3E) to be substantial (close to the false alarm level at 80% not shown in figure). Further, these two frequency components are simultaneously present and "significant" in both the IEF_y and airglow residual time series (see figure 4.3D). The phase spectrum, which is overlaid on the coherency spectrum in figure 4.3E, does not reveal any sharp changes (stable) around these two frequencies.To buttress the point that the residual airglow intensity fluctuations under investigation are due to electric field effects, horizontal magnetic field (H) measurements at multiple stations over Indian sub-continent are used. The important features of the magnetic field observations are described in the next section.

Horizontal Magnetic field measurements on 12 and 20 February, 2004

Horizontal magnetic field (H) variations during the periods of airglow observations on 12 and 20 February recorded from Tirunelveli (TIR, 8.67^{o}N, 77.82^{o}E, dip angle 1.86^{o}N), Pondicherry (PND, 11.92^{o}N, 79.92^{o}E, dip angle 9.58^{o}N), Visakhapatnam (VSK, 17.67^{o}N, 83.32^{o}E, dip angle 22.6^{o}N) and Hanle (HAN, 32.77^{o}N, 78.96^{o}E, dip angle 50.03^{o}N) are compared in figure 4.4A and 4.4B respectively. It is to be noted here that in the presence of oscillatory features in the temporal variations of H during the given interval on 12 February, 2004, the nighttime representative base value is not subtracted from the instantaneous H values (unlike the method applicable for daytime to find out the ΔH for a given station). The subplot 4.4A, therefore, depicts the temporal evolution of H values

recorded at the four stations on 12 February whereas the subplot 4.4B depicts the same on February 20, 2004. It is apparent from the subplots that magnetic fluctuations with seemingly multiple frequencies are present on 12 February, 2004 during 19:30-23:30 IST whereas 20 February, 2004 is marked by the absence of them. The fluctuations in H are almost similar, simultaneous (without any appreciable time delay) and in phase over all the stations encompassing dip equator to station beyond S_q focus. It is also noticed, by comparing figures 4.4A and 4.1C, that the fluctuations in H are anti-correlated with airglow fluctuations. In order to find the representative spectral components in H, the H variation recorded at TIR (H_{TIR}) is first detrended (by choosing a frequency pass-band 4.0-0.5 cycles/hr similar to IEF_y data with similar technique described earlier). Normalized periodogram is generated for H_{TIR} which is shown in the subplot 4.4C. Multiple frequency components including $\sim$2 cycles/hr and $\sim$1 cycle/hr are found to be present in the H_{TIR} time series. Furthermore, it is also noticed that the frequency component $\sim$1 cycle/hr is more dominant compared to the $\sim$2 cycles/hr component in the H data. This is in contrast with the dh_PF_2/dt time series where the frequency component $\sim$2 cycles/hr is found to be more dominant.

4.1.2 Discussion

It is known that the OI 630.0 nm nocturnal airglow emission arises owing to the dissociative recombination of O_2^+ with ionospheric electrons. Descent/ascent of F layer height causes change in the concentrations of the constituents in the airglow emission altitude and, therefore, enhances / decreases the volume emission rate by creating favourable / unfavourable conditions for the dissociative recombination reaction. It is to be noted that the temporal variabilities in h_PF_2, which is the virtual height at 0.834 of f_oF_2 and a routinely scaled parameter, correspond to the temporal variabilities in the F peak height h_mF_2 and their values are known to agree well with each other [e.g.*Shirke*, 1963] especially during nighttime. Therefore, the large-scale anti-correlation of airglow intensity variation with the h_PF_2 variations over SHAR in both figure 4.1A and figure 4.2A is expected. It is to be noted that the h_PF_2 variations over SHAR are sensitive to both electric field and meridional wind variations whereas over TRD, h_PF_2 responds to only electric field variations [*Krishna Murthy et al.*, 1990]. Therefore, the similarities in the large scale temporal variations of h_PF_2 over SHAR and TRD on 12 February (Figure 4.1A and 4.1B respectively), a geomagnetically disturbed night, are indicative of the active role played by electric field

on that night even over SHAR. The large scale h_PF_2 variations over SHAR on 20

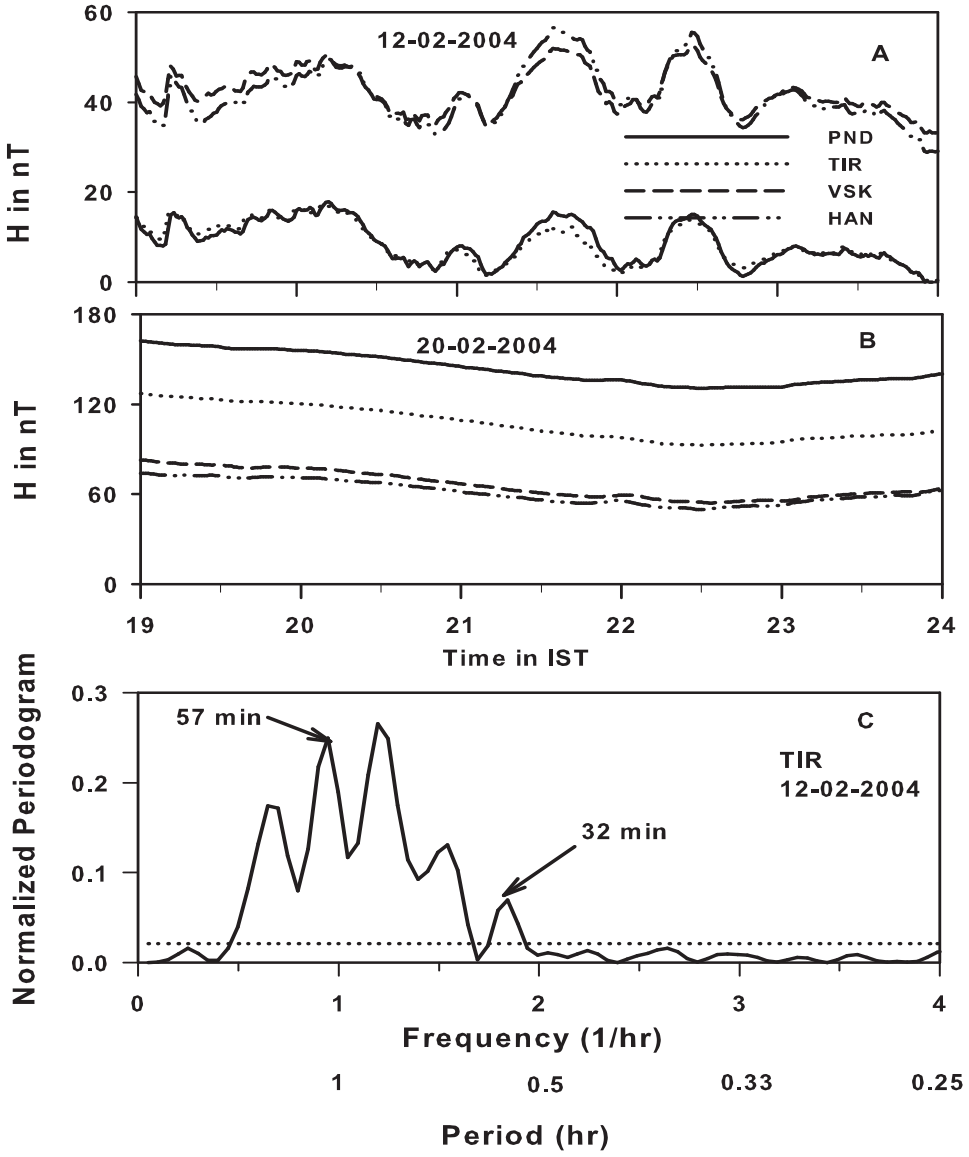

Figure 4.4: Horizontal magnetic field variations (H) recorded at Tirunelveli (TIR), Pondicherry (PND), Visakhapatnam (VSK) and Hanle (HAN) (A) on 12 February, 2004 and on (B) 20 February, 2004. The presence of in-phase, quasi-periodic fluctuations in H on 12 February, 2004 is apparent in contrast with 20 February, 2004, (C) Normalized periodograms for the detrended H variations recorded at Tirunelveli (H_{TIR}). Both the frequency components (marked by arrow) $\sim$1 cycle/hr and $\sim$2 cycles/hr are present in H.

February, an international quiet day, do not exhibit such similarities with the h_PF_2 variations over TRD (Figure 4.2A and 4.2B) bringing out the additional roles played by meridional wind in determining the h_PF_2 variations over SHAR.

In the absence of any direct electric field measurements over Indian zone, dh_PF_2/dt over TRD during nighttime is taken as a "proxy" for the zonal electric field variation

since the apparent vertical drift due to chemical loss process beyond 300 km is negligible [*Bittencourt and Abdu*, 1981; *Krishna Murthy et al.*, 1990]. Since on both 12 February (Figure 4.1) and 20 February (Figure 4.2), during the interval under consideration, the h_PF_2 heights did not go below 300 km, dh_PF_2/dt can be safely considered as a 'proxy" for the zonal electric field variation. It is interesting to note that the small scale variations in the observed airglow intensity and dh_PF_2/dt are directly correlated (Figure 4.1C) except during 22:15-23:15 IST. In order to understand the direct correlation between the airglow intensity and dh_PF_2/dt, the Barbier's relation [*Barbier*, 1959] is differentiated with respect to time. The differentiation provides a relationship between the temporal variation in the nocturnal 630.0 nm airglow intensity with two terms, one containing the changes in the F region peak electron density and the other containing the temporal changes in the peak layer height. The first term gains importance in the presence of large and rapid electron density changes like the plasma depletion events during ESF which is implicitly pointed out, for example, by *Sekar et al.* [2004]. As the observations reported here pertain to non-ESF nights, which are confirmed by the simultaneous Indian MST radar observations, the small scale variations in the airglow intensity are unlikely to be associated with the changes in the electron density. This point is strengthened from the temporal variation of peak electron density (obtained from f_oF_2) on 12 February, 2004 (not shown in figure) wherein no small scale fluctuations are observed. The second term, which is inversely dependent on the exponential variation of the layer height and also directly dependent on the small scale variation of the layer height, gains importance in this case. Therefore, the direct correlation between the small scale variations of layer height and airglow intensities is consistent with the Barbier's relation. The similarities in the temporal variations in the residual airglow intensity and the h_PF_2 over TRD in Figure 4.1C confirm the above proposition and adduce the electric field associated changes in the airglow intensity variations on this night during 19:45-23:15 IST. However, the reason for the time delay between the residual airglow intensity variations and dh_PF_2/dt variations during 22:15-23:15 IST is not clear and this aspect needs further investigation (figure 4.1C).

The overall similarities in the variations of dh_PF_2/dt and residual airglow intensity with residual IEF_y variations (figures 4.3B and 4.3C respectively) suggest that IEF_y acted as a common driver in bringing about the fluctuations in dh_PF_2/dt over TRD and as a consequence, in the residual airglow intensity over Gadanki on 12 February, 2004. Figures 4.3D and 4.3E, in perspective with figures 4.3B and 4.3C, bring out the two frequencies ($\sim$2 cycles/hr and $\sim$1 cycle/hr) at which IEF affects the low latitude ionosphere for the

event under consideration. It is interesting to note that the similarities of IEF_y with residual airglow intensity and dh_PF_2/dt break down during ∼20:45 and 22:00 IST (see figures 4.3B and 4.3C) which are also the times when IEF_y changes its polarity (see figure 4.3A).

It is generally accepted that nighttime ionospheric conductivity is not large enough to support substantial ionospheric currents. As discussed by *Stening and Winch* [1987], the oscillatory features in the instantaneous H variations during nighttime are often caused by modulation in the ring current especially so during disturbed period. In the present case (see figure 4.4), the presence of similar and simultaneous fluctuations in H recorded on 12 February, 2004, at all the four stations spread over a vast latitudinal sector indicates that the magnetic fluctuations are probably caused by magnetospheric currents on this night. Further, the differences in the spectral components in H and dh_PF_2/dt also indirectly indicate that the magnetic fields discussed here have different origin other than ionosphere. *Gonzales et al.* [1979] opined that the accuracy of correlations between nighttime H variations over dip equator, zonal electric field variations and the interplanetary magnetic field (IMF) variations during disturbed geomagnetic conditions, depends on the strength of the ring current. The strength of the ring current was relatively high (∼- 40-50 nT) in the present case. Based on the above discussion, the magnetic fluctuations on 12 February may be attributed to be of magnetospheric origin. However, the anti-correlation between the fluctuations in H and in airglow needs to be investigated further.

The frequency dependence of the shielding between ionosphere and magnetosphere is extensively studied by *Earle and Kelley* [1987]. *Gonzales et al.* [1979] as well as *Earle and Kelley* [1987] investigated the geomagnetic storm event during 17-18 February, 1976. This event is characterized by the significant dominance of ∼ 1.0 hr periodic component in the IMF B_z as well as in the electric fields at auroral and dip equatorial stations. On the other hand, *Sastri et al.*[2000] found periodicities in the range of 25-35 minutes in the F region vertical plasma drift (driven by zonal electric field) variations recorded at the nightside dip equatorial ionosphere which are temporally coherent with the variations in B_z of interplanetary magnetic field as well as with the variations in the geomagnetic components. In the present case, however, both the ∼1.0 hr and ∼0.5 hr periodic components in IEF_y seem to affect the F region of the ionosphere over low-equatorial latitudes.

Keeping in mind the possible dependence of the variations in the integrated airglow emission on other factors (like meridional wind) apart from the electric field variations, the causal relationship between the IEF and airglow intensity in the present case is remarkable.

4.2 Background: Interplanetary electric field and equatorial spread F

It is well-known that the plasma irregularity structures with scale sizes ranging from several hundreds of kilometers to a few centimeters are found in varying degrees in the F region ionosphere over equatorial latitudes during nighttime under favorable circumstances. Equatorial Spread F (ESF) is a generic name used to refer to the spread in the return echoes observed in ionograms in the presence of such plasma irregularity structures. The generalized Rayleigh-Taylor instability process involving gravity, electric field, zonal winds in a tilted ionosphere, and vertical winds is believed to be the causative mechanism for the development of ESF [see *Sekar and Kelley,* 1998 and references therein]. Different variabilities of ESF have been investigated during several decades in the past. Although many aspects of ESF have been reasonably explained based on the past investigations, day-to-day and storm time variabilities of ESF are yet to be understood comprehensively.

The effect of geomagnetic storms on the generation and evolution of ESF is one issue that underwent paradigm shift in the last several decades [see *Martinis et al.,* 2005 and *Becker-Guedes et al.,* 2004 including the references therein]. Both storm and ESF are highly variable events in space and time and, therefore, decoding the inter-connection between these two geophysical events requires favorably placed (both in space and time) simultaneous observations of both events. In recent times, multi-instrumented investigations using both ground-based and space-borne measurements have revealed many critical aspects of the causal relationship between storm and ESF [e.g. *S. Basu et al., 2001*; *Su. Basu et al.,* 2001; *Abdu et al.,* 2003; *Keskinen et al.,* 2006]. The earlier view that a geomagnetic storm suppresses ESF generation is now being replaced by the consensus that storm has apparently different effects on the ESF generation during post-sunset and post-midnight periods [e.g. *Aarons et al.,* 1980; *Rastogi et al.,* 1981; *Alex and Rastogi,* 1986]. The storms are observed to either suppress or trigger the post-sunset ESF and mostly trigger the post-midnight ESF events. It is also suggested that the triggering and inhibition of ESF during post-sunset period depends on the phase of the storm [*Abdu et al.,*1997]. For the generation of ESF, one of the primary effects of storm is to alter the zonal electric field conditions in the equatorial ionosphere.

The zonal electric field in the equatorial ionosphere during daytime is eastward that goes through a phase of pre-reversal enhancement (PRE) during the post-sunset hours in

the presence of rapidly depleting E region ionization environment before turning to the westward direction during nighttime. In the absence of the effects due to magnetic storm, the nighttime electric field in general continues to be westward after reversal [e.g. *Fejer*, 1997]. The occurrence of ESF was shown [e.g. *Fejer et al.*, 1999] to depend on the strength of the PRE. The strength of the PRE has been found to vary from one day to another. This, in turn, is shown to be one of the main reasons for the day to day variability of ESF [*Sekar and Kelley*, 1998]. Morphological investigations over Indian zone by *Krishna Murthy and Hari* [1996] reveal that although the amplitude of PRE varies depending on the solar epoch and season, PRE over Indian zone occurs generally around 19:00 hr IST. Therefore, the onset time of a geomagnetic storm and its effects are important to unmask the effect of perturbation electric fields on the equatorial ionospheric processes like ESF.

The perturbations in the zonal electric field in the low latitude ionosphere are generally brought forth by the ”prompt” penetration (PP) of the interplanetary electric field (IEF) into low latitude ionosphere [e.g. *Nishida*, 1968b; *Reddy et al.*, 1979; *Sastri et al.*, 1992; *Kikuchi et al.*, 2000; *Kelley et al.*, 2003] and by the ionospheric disturbance dynamo (DD) [*Blanc and Richmond*, 1980]. The ionospheric DD is a delayed effect owing to its association with the thermospheric wind circulation during disturbed period [e.g. *Scherliess and Fejer*, 1997]. The other mechanism, i.e. the PP process occurs due to the “sluggish” response of shielding electric field at the inner edge of the ring current opposing the rapid variations in the convection electric field generally during a period of southward turning of the Z-component of interplanetary magnetic field (IMF Bz). The time scale of PP process is generally of the order of an hour or less, depending on the magnetospheric plasma properties (e.g. plasma temperature) and conductivity of the auroral ionosphere [e.g *Vasyliunas*, 1970; *Wolf*, 1970; *Senior and Blanc*, 1984; *Spiro et al.*, 1988] although long duration penetration events are also reported [e.g. *Huang et al.*, 2005]. On the otherhand, during a period of rapid northward turning of IMF Bz from a steady southward configuration, the longer decay time of the shielding electric field gives rise to a residual electric field called “overshielding” electric field. It is shown [e.g. *Peymirat et al.*, 2000] that the overshielding electric field decays significantly within the first 30 minutes.

The local time variation of the effects of PP or overshielding event on the equatorial zonal electric fields depends primarily on the ionospheric conductivity distributions [e.g. *Fejer and Scherliess*, 1997]. Therefore, although the PP and overshielding events can occur during both day and nighttime [e.g *Wolf et al.*, 2001; *Goldstein et al.*, 2002; *Peymirat et al.*, 2000], significant effects are seen in the equatorial ionosphere during nighttime and

especially during post-midnight hours [e.g. *Fejer and Scherliess*, 1997; *Fejer*, 1997]. In the present investigation, an interesting case study involving a PP, overshielding processes and an ESF event is presented. The investigation reveals that the ionospheric conditions were not conducive on this night for ESF to occur till the PP event took place facilitating the identification of the contribution of PP in the triggering of the ESF event. In addition to that, it is indicated that an overshielding condition was generated in the inner magnetosphere during pre-midnight hours and probably triggered a plume event.

4.2.1 Data from multiple techniques

For the present investigation, data obtained from Indian MST radar (operated in ionospheric mode), the airglow photometer, ACE satellite as well as ionosondes at Thumba and SHAR are used. The propagation lag calculation is based on the methodology described previously in this chapter. In the present case, the propagation lag during the interval of interest varies from a minimum of $\sim$ 51 min to a maximum of $\sim$ 63 min. In addition to the above dataset, SYM-H index is also used to describe the development of geomagnetic storm on 7 January, 2005. SYM-H is a high resolution (1 min) geomagnetic index [*Iyemori and Rao*, 1996] which represents the magnetospheric ring current variations fairly well.

4.2.2 Results

Figure 4.5a depicts the variation in IEF$_y$ during 19:00-24:00 IST on 7 January, 2005. The variation in IEFy during this period comprises of two major polarity reversals that came after an international quiet day (January 6, 2005) and also after a quiet daytime of January 7, 2005 (as revealed by geomagnetic activity indices like Kp and Dst). IEF$_y$ changed its polarity at $\sim$ 19:30 IST corresponding to the southward turning of IMF Bz. IEF$_y$ changed from $\sim$-5 mV/m to $\sim$+ 5 mV/m in about an hour. Henceforth, this reversal of IEF$_y$ (turning to the dawn-to-dusk direction from a dusk-to-dawn orientation) corresponding to the north to southward reversal of IMF Bz will be denoted by R_{NS}. Afterwards, a wave-like variation in IEF$_y$ is observed for $\sim$ 90 min with a peak-to-peak amplitude change of $\sim$ 2 mV/m. At $\sim$ 21:30 IST, IEF$_y$ reversed its direction again, quite abruptly so, in response to a northward turning of IMF Bz. Henceforth, this reversal of IEF$_y$ (turning to dusk-to-dawn direction again from a dawn-to-dusk orientation) corresponding to the south to northward reversal of IMF Bz will be denoted as R_{SN}. In fact, IEF$_y$ changed

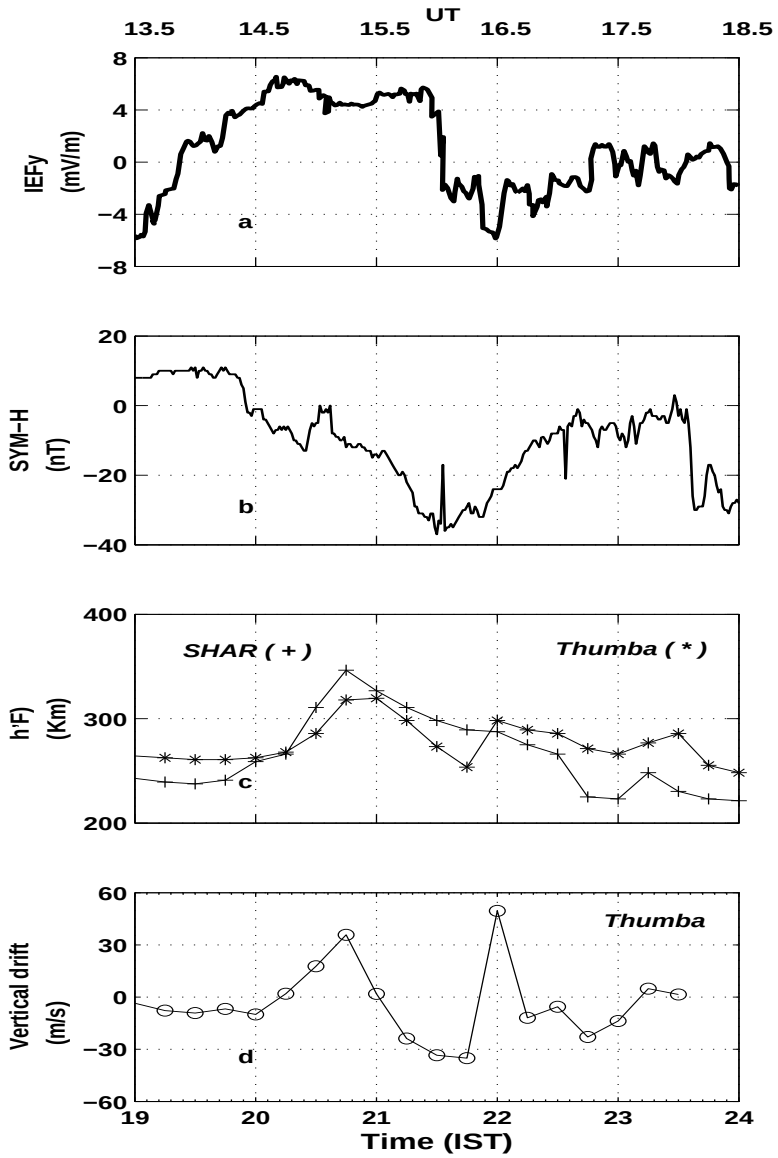

Figure 4.5: (a) Temporal variation in the Y-component of Interplanetary Electric Field (IEF$_y$) on the night of January 7, 2005 (Ap=40) from 19:00 IST to midnight. Corresponding UT is also given in the upper X-axis of this subplot. Note the conspicuous change in polarity of IEF$_y$ at $\sim$ 19:45 IST and $\sim$ 21:30 IST. (b) SYM-H variation during the given interval that shows the onset of the main and the recovery phases are concomitant with the IEF$_y$ polarity reversals. (c) The temporal variation of the bottomside of the F-layer (h'F) over Thumba and SHAR during the interval under consideration. Uncertainty in the height measurements are $\sim\pm$5 km. (d) Temporal variation of the vertical plasma drift corresponding to zonal electric field variation over Thumba on this night. Uncertainty in the vertical drift is $\sim\pm$ 6 m/s.

from $\sim$+5.5 mV/m to $\sim$-3 mV/m within 13 min in the case of R_{SN}. The value of IEF$_y$ plunged further to $\sim$ -6mV/m at $\sim$ 22:00 IST. After 22:00 IST, IEF$_y$ started recovering to values close to zero in an oscillatory manner. In order to find out the effects of IEFy variation on the evolution of the magnetospheric ring current, SYM-H index during the

same interval is plotted in Figure 4.5b. This Figure reveals that the strength of the ring current starts increasing with R_{NS} initiating the growth phase and start decreasing with R_{SN} triggering the recovery phase. With an aim to deciphering the effects of IEFy on the F region ionosphere over low latitude stations in the Indian zone, the variation of the base of the F layer (h'F) over Thumba and SHAR are presented in Figure 4.5c. Interestingly, the h'F variations over both Thumba and SHAR are similar during the interval under consideration except mainly during 21:45-22:00 IST. The base of the F-layer starts rising over both the places in response to R_{NS}. The ascent of the base of the F layer continued till 20:45 IST. Afterwards, h'F over both the places started descending. However, h'F over Thumba again registered a rapid ascent starting at $\sim$ 21:45 IST for a brief interval of $\sim$ 15 min. This ephemeral ascent of h'F over Thumba took place $\sim$ 15 min after the occurrence of R_{SN}. The h'F variation over Shar did not reveal any substantial ascent during this time. Based on the variation of the base of the F layer over Thumba, the vertical drift (V_d) over Thumba corresponding to zonal electric field is calculated. Figure 4.5d elicits the variation of vertical drift over Thumba during the interval under consideration here. The Figure reveals that V_d was already downward till 20:00 IST. However, an upward drift was found to get triggered by R_{NS} till $\sim$ 20:45 IST. The polarity of the drift eventually reversed (downward) after 21:00 IST and remained downward during 21:00-21:45 IST. Interestingly, an ephemeral upward drift was observed at 22:00 IST. Thereafter, the vertical drift became oscillatory and remained predominantly downward during the rest of the interval reported here. Thus, Figure 4.5 reveals the control of IEF$_y$ on the evolution of ring current and subsequently, in the zonal electric field over the dip-equator in the pre-midnight hours on January 7, 2005.

The equatorial zonal electric field is known to control the development of ESF structures in a significant way. Therefore, to facilitate the comparison of the zonal electric field and the ESF structures, Figure 4.5d is depicted again as Figure 4.6a. Figure 4.6b depicts the range-time-intensity (RTI) map obtained from the VHF radar at Gadanki during the interval under consideration. This Figure reveals that ESF got triggered $\sim$ 10 minutes after the plasma drift over Thumba reached a value of $\sim$40 m/s. The bottom envelope of the RTI plot during the time interval 2030-2230 resembles the variation in the vertical drift over Thumba at the same duration. High resolution RTI plot also reveals that the ESF structures were confined initially till 21:15 IST followed by a plume-like structure at $\sim$ 21:30 IST the growth of which was inhibited. However, $\sim$ 30 min after the onset of the sudden upward plasma drift at $\sim$21:45 IST, a vertically elongated plume structure

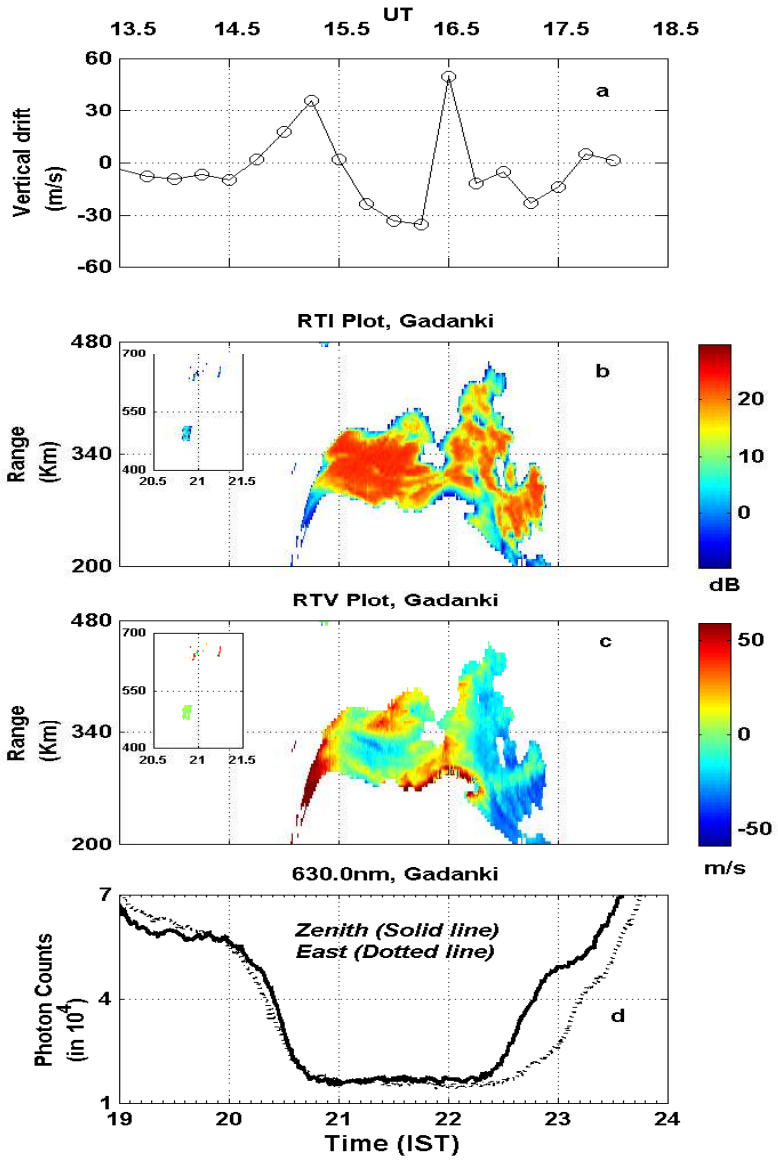

Figure 4.6: (a) Same as Figure 4.5d. (b) The Range-Time-Intensity (RTI) plot obtained using VHF radar at Gadanki revealing the development of ESF structure on January 7, 2005. The inset shows the isolated patches of irregularities at higher altitudes during this event. (c) The Range-Time-Velocity (RTV) map showing dynamics of the structures. The inset shows the velocity distributions inside the isolated patches at higher altitudes. (d) Temporal variation of the OI 630.0 nm airglow intensity corresponding to zenith and eastern direction (at 45^o elevation). The maximum measurement error is $\sim$ 220 counts during 20:35-22:45 IST when ESF structures are present.

was observed. Apart from the above-mentioned features, the RTI plot also reveals the presence of isolated patches of plasma irregularity structures at $\sim$ 500 km and also $\sim$ 650 km (see inset of Figure 4.6b) at $\sim$ 20:45 and $\sim$ 21:00 IST respectively. The generation mechanism of these isolated patches needs to be understood and will not be addressed in the present thesis. The range-time-velocity (RTV) plot, presented in Figure 4.6c, discloses the plasma velocity distribution inside the ESF structure elicited by the RTI map.

This Figure reveals that the velocities are upward at the initial phase of the growth of ESF structure and inside the plume-like structure with inhibited growth at $\sim$ 21:30 IST. More interestingly, velocities are found to be upward at the bottomside during $\sim$ 21:40-22:20 IST and also inside the vertically elongated structure as reported earlier. However, downward plasma velocities are noticed after $\sim$ 22:20 IST. The RTV plot also brings out the velocity distribution inside the isolated patches of irregularity structures (see inset of Figure 4.6c) which will not be addressed here.

In order to compare the plasma irregularity structures and dynamics revealed by the VHF radar maps with the OI 630.0 nm airglow observations, the airglow intensities over zenith as well as in eastern direction during the same interval are shown in Figure 4.6d. The intensities over zenith and in the eastern direction decreased sharply corresponding to steep h'F ascent (see Figure 4.5c) starting at $\sim$ 20:15 IST. However, the step-like increase in the intensity level after $\sim$ 22:30 IST is concomitant with the presence of plasma irregularity structures moving downward (see Figure 4.6c) and also with the h'F decrease over SHAR (see Figure 4.5c). In between these two steep descending and ascending intensity variations, the airglow intensity registered a low-amplitude undulation which is in opposite phase with bottomside undulation in the ESF structure revealed by the RTI (or RTV plot). By comparing the identifiable points of mutual correspondence, it is noted that the intensity variation corresponding to the eastern direction precedes the intensity over zenith during 20:00-20:30 IST (note the cross-over point at 20:00 IST). However, the intensity variation over zenith precedes the intensity variation corresponding to eastern direction after $\sim$ 22:20 IST. It is difficult to make such analysis based on these curves in Figure 4.6d during the interval 20:30-22:20 IST. The connections among different subplots reported in this section will be discussed in the following section.

4.2.3 Discussion

It is generally accepted that h'F variation during nighttime can be used as a reliable parameter to infer the vertical plasma drift over the dip equator [e.g *Rastogi et al.*, 1991] and this is true even during spread-F conditions [e.g. *de Paula et al.*, 2004] when corrected for the chemical loss below 300 km (shown in Figure 4.5d). The F-region vertical plasma drift over the magnetic dip equator depends mainly on the zonal electric field variations. However, for a low latitude station with a finite magnetic dip angle (in the present case, SHAR and Gadanki), the vertical plasma drift is also controlled by the meridional wind

in addition to the electric field. Therefore, similarities (Figure 4.5c) in the h'F variations over a dip equatorial station and a low latitude station indicate towards a possible dominance of electric field effect on the ionospheric height variation on this particular night. The additional effect of meridional wind over SHAR probably caused the less-pronounced similarity during 21:45-22:00 IST in the variation of the base of the F layer over Thumba and SHAR.

It is shown [e.g *Sekar and Kelley*, 1998; *Fejer et al.*, 1999] that pre-reversal enhancement (PRE) of the zonal electric field, that manifests in the form of post-sunset F-layer height rise, controls the day-to-day variabilities of ESF occurrence and often large PRE is a necessary condition for the ESF occurrence. Further, the onset of post-sunset ESF generally occurs at and around the reversal time of the zonal electric field [e.g. *Fejer et al.*, 1999]. Morphological study over Indian region by *Subbarao and Krishna Murthy* [1994] reveals that the PRE over Thumba occurs at $\sim$ 19:00 IST in the winter months during both solar maximum and minimum years. However, Figure 4.5d (or Figure 4.6a) suggests that the zonal electric field was already westward during 19:00 to 20:00 IST. This westward zonal electric field is unlikely to be associated with the pre-conditioning of the equatorial ionosphere by the DD process as the period before the onset of the storm was geomagnetically quiet. As the background electric field condition over Thumba was westward, the ESF structures were not developed to be recorded by the ionosonde at 19:00 IST. Therefore, it is unlikely that the ESF structures recorded by the VHF radar got generated west of the radar site and drifted towards it. As a consequence, the ESF irregularities observed by VHF radar at $\sim$ 20:40 IST are believed to be triggered simultaneously over the longitude zones of Thumba and SHAR. Furthermore, the upward drift (caused by the eastward zonal electric field) at $\sim$ 20:15 IST is different on this night from the general pattern. In addition to that, the upward drift at 20:15 IST got triggered during the interval when R_{NS} was operative indicating that the penetration electric field associated with R_{NS} is responsible for the upward drift. R_{NS} also triggered the onset of the growth phase of a storm which is evident from Figure 4.5b. Therefore, it appears that R_{NS} flagged off the penetration of IEF_y into the dip-equatorial ionosphere that eventually led to the ESF event. In order to confirm this, the growth rate of generalized Rayleigh-Taylor (RT) instability, known to be the causative mechanism of ESF, is calculated based on linear analysis by including the effects due to the zonal electric field induced by IEF_y. Neglecting neutral

wind effect, the growth rate (γ) can be expressed as follows

$$\gamma = \frac{1}{L}\left[\frac{g}{\nu_{in}} + \frac{E}{B}\right] \tag{4.3}$$

where g, ν_{in}, L, E and B are acceleration due to gravity, ion-neutral collision frequency, plasma scale length, zonal electric field (positive eastward) and the strength of the Earth's magnetic field. In order to examine the generation of the irregular structure observed by the MST radar after 20:40 IST, the linear growth rates are calculated at two different time zones (19:30 and 20:30 IST) to cover well and just before the appearance of irregularity on the RTI plot. The corresponding ionograms from Thumba are reduced to estimate the bottomside plasma scale lengths at these time zones on this night. The bottomside plasma scale lengths turn out to be ~ 30 km and ~ 20 km at 1930 and 20:30 IST, respectively. The decrease in plasma scale length is believed to be caused by the change in the polarity of zonal electric field from westward to eastward owing to the penetration of interplanetary electric field. The average values of ν_{in} and g in the altitude region of 250 to 325 km are taken to be equal to 1 s^{-1} and 9.0 ms^{-2}. Based on Figure 4.5d, the plasma drift (E/B) values due to zonal electric field are taken to be -10 ms^{-1} and 30 ms^{-1} at the two time zones. The growth rate turns out to be slightly negative ($\sim$- 0.3×10^{-4} s^{-1}) at 19:30 IST that explains the absence of the irregularity at that time. However, at 20:30, the growth time for the development of irregularity at 325 km is ~ 9 minutes (corresponding to a growth rate of $\sim 1.95\times10^{-3}$ s^{-1}). Thus, the appearance of irregularity at $\sim$ 20:40 IST is believed to be triggered by changes induced by the penetration of storm time electric field. Therefore, the electric field associated with the PP event not only changed the bottomside plasma scale length (L) but also contributed through the electric field term (E) in equation 4.3 for the generation of ESF structure.

The ESF structure that got triggered by R_{NS} remained confined to the bottomside of the F layer and no vertically elongated plume structures were seen to be developed till 21:45 IST. *Sekar and Kelley* [1998], on the basis of a non-linear numerical simulation model, found that longer wavelength ESF structures can get confined in the bottomside F region with the combined effects of shear in the zonal plasma drift and a nighttime westward electric field. It is to be noted that the zonal electric field, after the initiation of ESF on this night, turned westward again after $\sim$ 21:00 IST and remained westward till 21:45 IST. Further, as discussed in chapter 3, by comparing the eastward and zenith observations of OI 630.0 nm airglow intensity variations during and just before the onset of ESF, the polarity of the zonal velocity of plasma was obtained. The polarity of zonal velocity

at the airglow emitting altitude ($\sim$ 250 km) was westward during 20:00-20:30 IST and was eastward after $\sim$ 22:20 IST (Figure 4.6d). As the polarity of the zonal plasma drift above 300 km is generally eastward, a strong shear can be expected to be present during the initial hours. The confinement of ESF structures till 21:15 IST and inhibition towards the growth of a plume-like (note the upward velocity revealed by the RTV map in Figure 4.6c) structure at $\sim$ 21:30 IST can be attributed to the presence of strong shear in the zonal plasma drift and the westward electric field. As the shear strength is found to reduce with time after the onset of ESF, the possibility of development of vertically erected plume structure increases.

A conducive situation for the development of plume structure arose after R_{SN} took place at 21:45 IST. Thereafter, the vertical drift over Thumba responded to R_{SN} by abruptly becoming upward at 22:00 IST. Interestingly, at this time, the RTI plot (Figure 4.6b) shows a discernible crest in the bottomside envelope. The RTV plot (Figure 4.6c) reveals that the velocities are upward at this crest region and in the region of vertically elongated plume structure. Taking into consideration a typical growth time of a plume, the vertically elongated plume structure is found to occur after $\sim$30 minutes of reversals in IEF_y and zonal electric field over dip equator. This plume structure appears to be due to the eastward electric field arising out of the overshielding condition at the inner edge of the ring current. As the development of plasma plume involves non-linear growth, a detailed simulation study is being carried out to understand the occurrence and growth of this plume structure. This non-linear simulation study will be discussed in the next chapter.

Overshielding condition ensues after IMF Bz takes a sudden northward turn from a southward configuration that persisted for some time. *Rastogi and Patel* [1975] observed the F region electric field perturbations over dip equator in response to northward reversal of IMF Bz. Later, *Kelley et al.* [1979] invoked the concept of overshielding and explained the causal relationship between the F region electric field fluctuations over dip equator and the sudden northward turning of IMF Bz. The effects of overshielding electric field on plasmasphere are being studied in great detail in recent times [e.g. *Burch et al.*, 2001; *Goldstein et al.,* 2002] and it is considered [e.g. *Toffoletto et al.,* 2003] as an important player in setting off plasma irregularity processes over dip equatorial regions during ESF events. *Ebihara et al.* [2004] recently found that overshielding condition is produced when the auroral conductivity decreases abruptly near the end of the growth phase of the ring current (Dst minimum), triggering off the decay phase. In the present case also, it

is seen (see Figures 4.5a and 4.5b) that R_{SN} coincides with the onset of the decay of the ring current (minimum SYM-H). Overshielding electric field is generally found to play an active role in the low latitude ionosphere during post-midnight hours. In the present case, interestingly, the evolution of a plasma plume seems to be affected by the overshielding electric field in the pre-midnight hours.

Regarding the OI 630.0 nm airglow intensity variation during the ESF period, it is noticed that the intensity variation during 20:30-22:30 IST corroborated well (anti-correlation) with the bottomside envelope of the ESF structure revealed by the RTI (or RTV) plot. Before 20:30 IST, the airglow intensity variation was found to decrease corresponding to the increase in the base of the F layer height over SHAR (Figure 4.5c). This decrease in intensity was also nominally assisted at a later stage by the presence of an upward moving ESF structure seen in Figure 4.6c. Further, the step-like increase in the airglow intensity after 22:30 IST was mainly due to the presence of the altitudinally decreasing feature in the bottom envelope of the ESF structure in addition to the presence of vertically elongated structures having downward velocities.

Therefore, the temporal history of the space weather event on this night along with the other supporting measurements and with the present day understanding of the development of ESF suggest that the ESF event on this night appears to be driven by IEF. Although the influence of IEF on the equatorial electrodynamics is not uncommon, the effects of IEF on this particular ESF event came out rather conspicuously owing to the several factors like the westward zonal electric field condition before the onset of the PP and the ESF events, the altitudinal confinement of the ESF structures after the onset that made the resurrection of the plume structure under the influence of overshielding electric field sufficiently prominent. In addition to that, the overshielding event took place during the pre-midnight hours in the present case. Considering the enormous spatial and temporal variabilities associated with ESF and space weather events, the present investigation provides important clues to the future researches on the equatorial ionosphere influenced by space weather events.

4.3 Summary

The present chapter elicits the signatures of the solar wind electric field in the OI 630.0 nm airglow recorded at a low latitude station during a geomagnetic storm event based on the remarkable conformity of small scale airglow intensity fluctuations with the mea-

surements by three independent (satellite, ionosonde and magnetometer) techniques. It is found that the periodicities $\sim$0.5 hr and $\sim$1.0 hr in the airglow intensity variations on 12 February, 2004 are caused by interplanetary electric field. Furthermore, this chapter also brings out a case in which ESF is triggered by the effects of the interplanetary electric field when the background ionospheric conditions over Indian zone was not conducive for ESF generation before the onset of a prompt penetration event. Numerical calculation based on the linear growth rate of plasma irregularities is presented to buttress the role of the electric field associated with the prompt penetration in the triggering of the ESF event on this night. The investigation also unravels the effects of an eastward overshielding electric field on the dip equatorial ionosphere in the pre-midnight hours and it is indicated that the generation of a plasma plume structure is associated with this electric field.

Chapter 5

Numerical simulation model investigation of storm-time plasma irregularities

5.1 Background

In general, the geomagnetic storms alter various parameters of ionosphere-thermosphere system (ITS). Comprehensive reviews on the effects of geomagnetic storm on ITS are available in literature [e.g. *Schunk and Sojka*, 1996; *Abdu*, 1997; *Buonsanto*, 1999]. The present investigation deals with the changes in the electric field and its effects as a consequence of geomagnetic storms. It is rather well known that the electric field conditions over low and equatorial latitudes get altered as a consequence of geo-effective space weather events associated with geomagnetic storm.

In particular, the equatorial electric fields are modulated by three ways. The alteration of electric field associated with the storm sudden commencement [e.g. *Sastri et al.*, 1993] is transient and cannot contribute for process involving a few hours. The electric fields also get altered by prompt penetration of interplanetary electric fields and/or by the action due to disturbed dynamo associated with altered wind system. The time scale of the former is generally considered to be less than 2.0 hr while the latter process takes several hours after the magnetic activity, to affect the low latitude ionospheric electric fields [*Blanc and Richmond*, 1980]. Based on the Jicamarca radar measurements from magnetic equator, an empirical model [*Fejer and Scherliess*, 1997] of storm-time equatorial zonal electric field was developed. For the present problem, the storm time modification of the

equatorial zonal electric field during nighttime is considered. In this regard, *Fejer and Scherliess* [1995] concluded that the zonal electric fields in the evening sector over Jicamarca tend to enhance during prompt penetration events while the long-lived disturbance dynamo electric fields tend to reduce equatorial zonal electric fields. Previous research works [*Sekar and Kelley*, 1998; *Fejer et al.*, 1999] revealed the importance of temporal patterns of zonal electric field during post sunset hours in addition to other parameters in connection with the day-to-day variability of plasma instability process leading to the occurrence of equatorial spread F (ESF).

A large number of correlation studies between the geomagnetic storms and the occurrences of ESF are available in the literature [e.g *Martinis et al.*, 2005 and the references therein]. However, a conclusive relationship is not yet reached at because of enormous variabilities in both storm and ESF events. It was initially believed that the occurrence of ESF is inhibited during magnetic storm [*Lyon et al.*, 1960]. By considering the occurrence of ESF at post-sunset and post-midnight hours separately, later analysis revealed that the post-midnight ESF events are triggered by storm events [*Aarons et al.*, 1980]. On the other hand, the occurrence of post-sunset ESF events are triggered by the geomagnetic storms on some occasions particularly during non-ESF season [e.g. *Aarons et al.*, 1980; *Rastogi et al.*, 1981] and not so on a few other occasions [e.g. *Alex and Rastogi*, 1986]. It was suggested that the triggering or inhibition of ESF depends on the phase of the storm [*Abdu*, 1997]. In this chapter, two case studies [*Chakrabarty et al.*, 2005, 2006] exhibiting variabilities in the occurrence of ESF and plume events during two "prompt penetration" (of interplanetary electric field into low latitude ionosphere) events, discussed in the previous chapter, are reproduced to address the requirements for the development of plasma plume induced by storm-time electric field.

Figure 5.1 depicts a sequence of observations for two cases obtained on geomagnetically disturbed nights. The left panel corresponds to case 1 observed on 12 February, 2004 when the A_P index was 30. The temporal variations of IEFy, deduced from the ACE satellite measurements and suitably time delayed for each point as described in Chapter 4, are depicted in a subplot (L1). The temporal variations of the plasma drifts corresponding to the zonal electric fields deduced from ionosonde over Thumba are depicted in a subplot (L2). As there is a definite correlation between ionospheric layer movement and airglow intensity, the high temporal resolution ($\sim$2 min) observations of OI 630.0 nm airglow emission intensity variations support the continuous variations in the zonal electric field in both cases. The variations in the zonal electric fields over magnetic equator

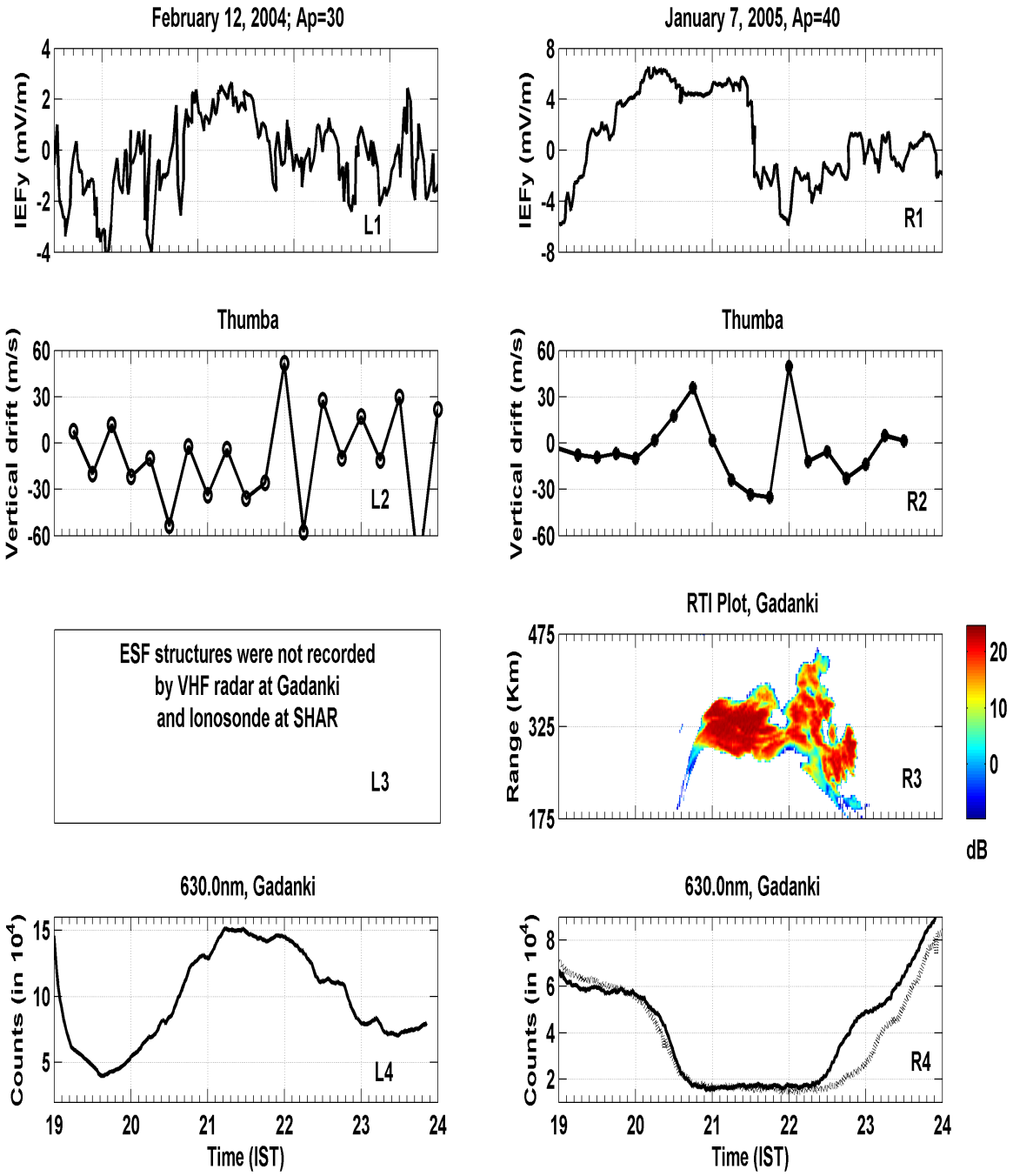

Figure 5.1: A vertical sequence of temporal variation of interplanetary electric fields and vertical drift over magnetic equator corresponding to zonal electric fields during the two magnetic storm events on February 12, 2004 (subplots L1 and L2 respectively) and January 7, 2005 (subplots R1 and R2 respectively). The ESF irregularities on January 7, 2005 as observed by VHF radar in the form of Range-Time-Intensity map is depicted at the bottom of the right hand side panel (R3). The color code represents the strength of irregularities. Subplot L4 represents OI 630.0 nm airglow intensity variations in vertical direction on February 12, 2004. Subplot R4 represents airglow intensity variations in both vertical and eastward directions on January 7, 2005. These Figures are based on the publications by *Chakrabarty et al.*, 2005 and *Chakrabarty et al.*, 2006.

correspond to IEFy fluctuations and a reversal just after 21:45 IST in the polarity of the electric field is found. Corresponding fluctuations in 630.0 nm airglow intensity are shown in subplot (L4). The details of this observation and its consequence on airglow emissions are discussed in the previous chapter. Though the VHF radar at Gadanki was operated in ionospheric mode, ESF was found to be absent during 19:15 hr IST to midnight on this night conforming to the ionosonde observation from SHAR, a location 100 km east of the radar site. The right panel of Figure 5.1 corresponds to case 2 observed on 7 January, 2005 when the A_P index was 40. Similar to the left panel, the temporal variations of IEFy and the plasma drifts on this night are depicted in subplots (R1 and R2) respectively. It is to be noted that since the scattering of radio waves, in general, occurs above the base of the F layer, temporal variations in h'F can be used to derive plasma drifts even during ESF condition as followed by many researchers [e.g. *Subbarao and Krishnamurty*, 1994; *Becker-Guedes et al.*, 2004]. Reversals from downward to upward plasma drifts corresponding to the zonal electric fields are observed just after 2000 and 21:45 IST. The Range-Time-Intensity (RTI) plot of 3m irregularities associated with ESF as observed by the Indian MST radar is depicted in the subplot (R3). The colour code corresponds to the intensity (strength) of the return echoes. It is found that the ESF activity started at $\sim$20:40 IST and a vertically rising plume is observed during 22:00-22:30 IST.

The occurrences of ESF for case 2, as observed by ionosondes located at Thumba and SHAR ($\sim$400 km zonally separated sites) are nearly simultaneous. Further, bidirectional (zenith and 45^o east) photometric observations of 630.0 nm airglow emission from MST radar site, depicted in subplot R4 in Figure 5.1, revealed almost simultaneous airglow intensity decrease starting from 20:40 IST, the time of the onset of ESF. The decrease seen in 630.0 nm intensity after 20:40 IST in spite of downward movement of ambient F region plasma is essentially due to ESF structures. In addition, the airglow signatures observed over vertical direction corroborate well with the bottomside structures. This fact along with the impulsive followed by a continuous nature of the development of ESF structure and the corresponding optical observations indicates that the development of ESF in this case was triggered by an external agency simultaneously in vertical and zonal directions. Moreover, the bottomside structure is confined to localized altitude region where zonal plasma drift changes its polarity and thus, it is close to zero. The above evidences suggest that the ESF structures revealed by the VHF radar in this particular case are unlikely to have drifted from a zonally separated location to the radar observation site at a later time. Optical observations and the effects of undershielding electric field associated with IEFy

in the triggering of an ESF event and subsequent development of a plasma plume under the influence of overshielding electric field are described in detail in the previous chapter.

It is to be noted that the magnitude of the eastward electric field, the time of occurrence of the second reversal (just after 21:45 IST) and the duration of the reversed conditions (0.5 hr) remain nearly the same for both the cases. The important difference between the two cases is the polarity reversal of the zonal electric field to eastward just after 20:00 hr. on 7 January, 2005 and the subsequent generation of ESF. On the other hand, though the penetration of certain periodic components (periodicities $\sim$0.5 hr and 1.0 hr) of interplanetary electric field was observed on 12 Feb., 2004, significant eastward excursion of the ionospheric electric field during 19:00 - 21:30 IST was not observed. Thus the occurrence of ESF was inhibited on this night. *Chakrabarty et al.* [2006] brought out, through linear growth rate calculation, the importance of this eastward electric field on 7 January, 2005 in terms of the contributions through E $\times$ B instability and decrease in the plasma scale length. However, the ionospheric eastward electric field on this night (7 January, 2005) returned to the usual nighttime westward condition after 21:00 IST. A second reversal to eastward condition took place just after 21:45 IST and a plasma plume was observed after around half an hour.

It is well-known that the linear analysis describes the zero order conditions for the initiation of ESF irregularities. However, nonlinear analysis is needed to describe the evolution of plasma bubble structures which penetrate to F region peak altitudes and manifest as plasma plumes. The earlier nonlinear analyses [*Ossakow et al.*, 1979; *Ossakow*, 1981] revealed that the formations of plasma bubbles are not conducive within half an hour under the background condition when the F layer peak altitude lie around 350 km. Recently, *Keskinen et al.* [2006] investigated the alteration in the development of plasma bubble owing to the storm-time electric field. However, that investigation pertains to post-sunset hours only as the storm-time perturbation of electric field took place during that time. The penetration-induced development of plasma bubble during nighttime conditions is yet to be comprehensively understood. In the present chapter, it is examined under what conditions the development of plasma bubbles is feasible with a time scale of around 2000 s when the above background ionospheric conditions pertaining to pre-midnight hours as discussed in the previous paragraph, are imposed. The possible consequence of E-region conductivity is also discussed.

5.2 Numerical Simulation Model

The nighttime development of plasma bubble is investigated by means of numerical simulation model of ESF [*Sekar et al.*, 1994], the nuances of which are already discussed in chapter 2. The effects of the E region conductivities are considered to be less during nighttime. In addition to that, since the development of irregularities is field-aligned (z axis), a two-dimensional model perpendicular to the geomagnetic plane is used for this investigation. The basic plasma fluid equations, under F region approximations, were reduced to the following two coupled partial differential equations.

$$\nabla.(\nu_{in} N \nabla\phi) = B\Big[-g + W_y \nu_{in} + (E_{xo}/B)\nu_{in}\Big]\frac{\partial N}{\partial x} \tag{5.1}$$

$$\frac{\partial N}{\partial t} - \frac{\partial}{\partial x}\Big[(N/B)(E_{yo} + \frac{\partial\phi}{\partial y})\Big] + \frac{\partial}{\partial y}\Big[(N/B)(-E_{xo} + \frac{\partial\phi}{\partial x})\Big] = -\nu_R N \tag{5.2}$$

Here N and ϕ represent the electron number density and the perturbation potential respectively. The symbols g, ν_{in}, ν_R and B correspond to acceleration due gravity, ion-neutral collision frequency, recombination rate and the strength of Earth's magnetic field respectively. E_{xo}, E_{yo} and W_y are the background electric field components in zonal (+x westward) and vertical (+y upward) directions and vertical wind respectively. Equation 1 brings out the spatial distribution of the perturbation potential generated by the generalized Rayleigh-Taylor (GRT) instability in a slab geometry. The temporal evolution of plasma density is described by equation 2. Numerical solutions of these coupled partial differential equations are obtained over a plane orthogonal to Earth's magnetic field over dip equator. The computations are made over a region of $\pm$ 200 km in the zonal direction and from 182 km to 534 km in vertical directions. The region is divided into 200 (zonal)$\times$ 176 (altitude) grid points with grid sizes of Δx = 2 km and Δy = 2 km. Periodic boundary condition in zonal direction is imposed for N and ϕ. In the vertical direction, transmittive and Neumann boundary conditions are imposed on N and ϕ respectively. As discussed in chapter 2, numerical methods including flux corrected transport algorithm to limit numerical diffusion, are adopted for the present investigation.

5.2.1 Inputs to the model

One of the important inputs for the present investigation is the altitude profile of electron density characteristic of pre-midnight hours (21:30-20:00 IST). Since ESF was present, the ionograms could not be used to deduce the altitude profile. The morphological

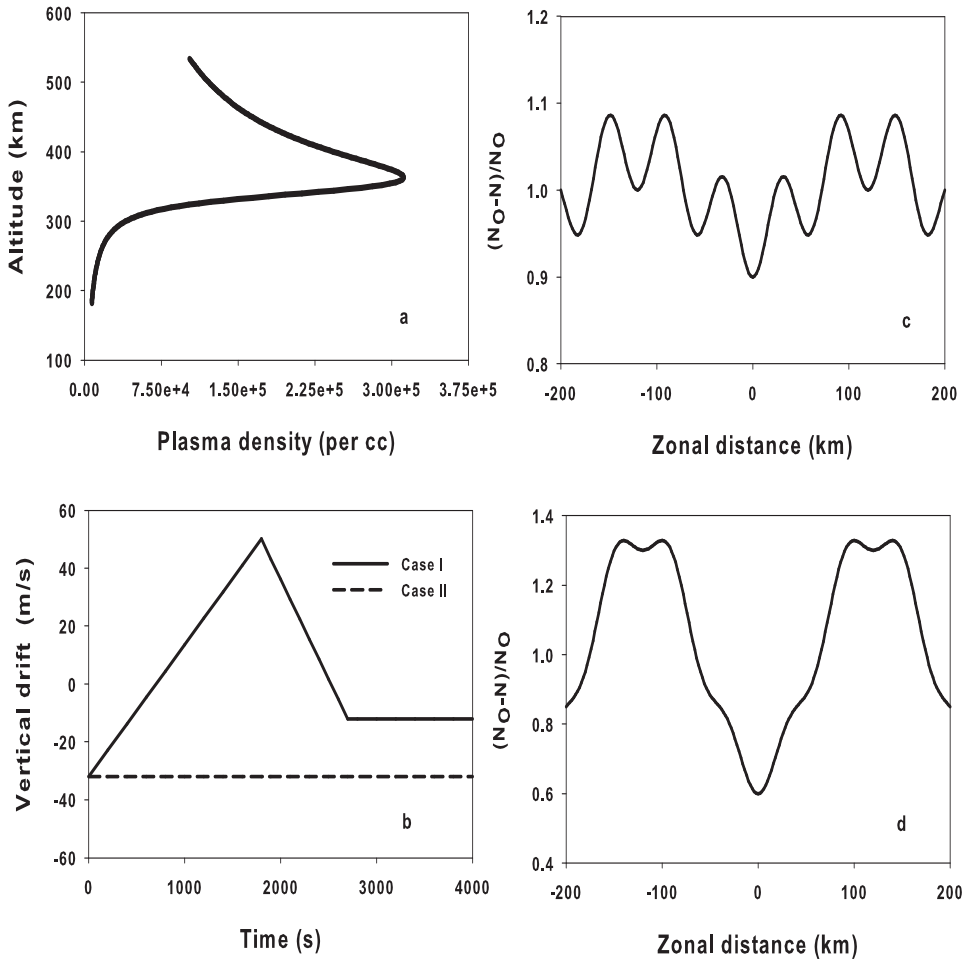

Figure 5.2: (a) A typical altitude profile of electron density during pre-midnight hours used in the simulation model, (b) temporal patterns of vertical drift corresponding to the zonal electric fields used in the model. These patterns are chosen to represent the storm-time reversal of the zonal electric field and the absence of it during pre-midnight hours, (c) and (d) normalized amplitudes of initial perturbation along zonal direction for superposition of two modes employed at different altitude regions.

studies over Indian region [*Chandra et al.*, 1973] based on the true height analyses revealed that the peak altitude of F region over Thumba during 21:30-22:00 hr IST, depending on low and high sunspot values, varies from 300-370 km. Therefore, a set of profiles with different peak altitudes ranging from 330 km to 370 km with three different sets of plasma scale lengths ranging from 20 to 30 km are used to investigate the required seed perturbation for the evolution of plasma bubble during pre-midnight hours. These variations are introduced to understand the occurrence variability in the development of storm-time plasma plume during pre-midnight hours. In order to describe the development of plasma bubble over a bottomside structure, more than one wavelength mode is needed as seed perturbation [*Sekar et al.*, 2001]. A nearly identical intensity variations

in the airglow intensity over zenith and around 250km east of radar site, suggest that the upper cut-off in wavelength can be taken $\sim$250 km. Thus initial perturbation with superposition of two modes in the form of

$$N(x,y) = N_0(y)\Big[1 - \Big[a_1 \cos\Big(\frac{2\pi}{\lambda_1}x\Big) + a_2 \cos\Big(\frac{2\pi}{\lambda_2}x\Big)\Big]\Big] \tag{5.3}$$

is introduced in the model. A larger wavelength (λ_1) mode of 240 km and another mode with wavelength (λ_2) of 60 km without any phase difference between them are used in the present investigation. The amplitude of the second wavelength mode (a_2) is chosen to be around 5% of background electron density and remains constant over an entire altitude region. However, the amplitude of the longer wavelength mode (a_1) is varied over a limited altitude region where steep gradient exists to support the presence of large scale irregularities developed during post-sunset hours. The reason for such an altitude variation in initial perturbation is discussed later. In the remaining altitude regions, the amplitudes are kept constant and similar to that of the second wavelength mode with a value of 5% of background electron density value. Further, as the neutral wind system is not expected to get altered within two hours similar to that of the electric field due to the effects of storm in the main phase, the neutral wind contribution is not taken into account in the present investigation.

In general, in order to understand the occurrence variability, the parameters of the electron density profiles are varied as described above. However, to understand the particular case study described in the right hand side of Figure 5.1, the inputs as depicted in Figure 5.2 are introduced in the model. The altitude profile of electron density is depicted in Figure 5.2a. The peak altitude of the F region was chosen to be around 360 km with a plasma scale length of 25 km. Noting the eastward excursion of the zonal electric field on January 7, 2005 around 20:00-21:00 IST and also considering the altitude extent arising due to the magnetic field mapping of the plasma irregularities at the base of the F region ($\sim$280 km) from an off-equatorial observational site (Gadanki) to magnetic dip equator, the altitude of the F layer peak height is chosen to be around 360 km with a minimum plasma scale length of 25 km.

In order to represent the equatorial zonal electric field conditions during 21:45-22:30 hr during disturbed nights as shown in Figure 5.1, the vertical plasma velocity as depicted in Figure 5.2b is used as input to the model. On the other hand, to investigate the development of ESF in the absence of penetration of disturbance electric field, case-II of Figure 5.2b is used in the model. As described in the previous paragraph, the initial perturba-

tions in plasma densities at two altitude regions are depicted in Figures 5.2c and 5.2d. Note that the penetration described in Figure 5.2d is used only to demonstrate that perturbations with large amplitudes in a limited altitude region are needed for the development of late-night plumes in addition to electric field reversal. The details are discussed later.

5.3 Results

Figure 5.3 depicts iso-electron density contours in zonal-vertical plane 2000 s after the initiation of the instability process. This result is a case study with the input in Figure 5.2a and with a_1 = 5% and a_2 = 5% over the entire altitude region along with driving agencies gravity and the vertical velocity corresponding to zonal electric field as depicted in case-I of Figure 5.2b. The growth of the irregularities is seen without the development of plume penetrating up to an altitude of 450 km. Further, the irregularities are yet to get into the non-linear development for the formation of plasma plume event. This result will be discussed later in the context of the need for pre-seed for the development of plasma plume during pre-midnight hours.

In order to quantify the amount of seed perturbation in long-wavelength mode for the development of plasma plume within 2000 s during pre-midnight hours, the perturbation amplitude a_1 was varied keeping second wavelength perturbation a_2 constant. A trial and error analysis was carried out by varying a_1 and comparing the results with the late night plume observation (Figure 4.6b or 5.1R3) on 7 January, 2005 during 22:00-22:30 IST. The result obtained with a_1 = 35% and a_2 = 5% in the altitude region of 280-360 km and 5% perturbation in both the modes in the remaining altitude region is depicted as figure 5.4. The driving agencies used for this simulation are gravity and electric field as shown in case-I of Figure 5.2b. This simulation result reveals the development of large scale plasma bubble which acts as a seat for the generation of plume event in 3 m irregularities during late night hours similar to the observation on 7 January, 2005. In order to find out the role of eastward overshielding electric field, as discussed in the previous chapter, a simulation is carried out with the electric field condition as described in case-II of Figure 5.2b. This is a hypothetical case wherein the equatorial ionospheric electric field would have continued to be westward without the effect of the overshielding electric field. The other inputs are the same as in previous simulation output at 2000 s described in Figure 5.4. The simulation output at 2000 s is depicted in Figure 5.5. This result reveals that the perturbations are stabilized by the strong westward electric field. This happens in

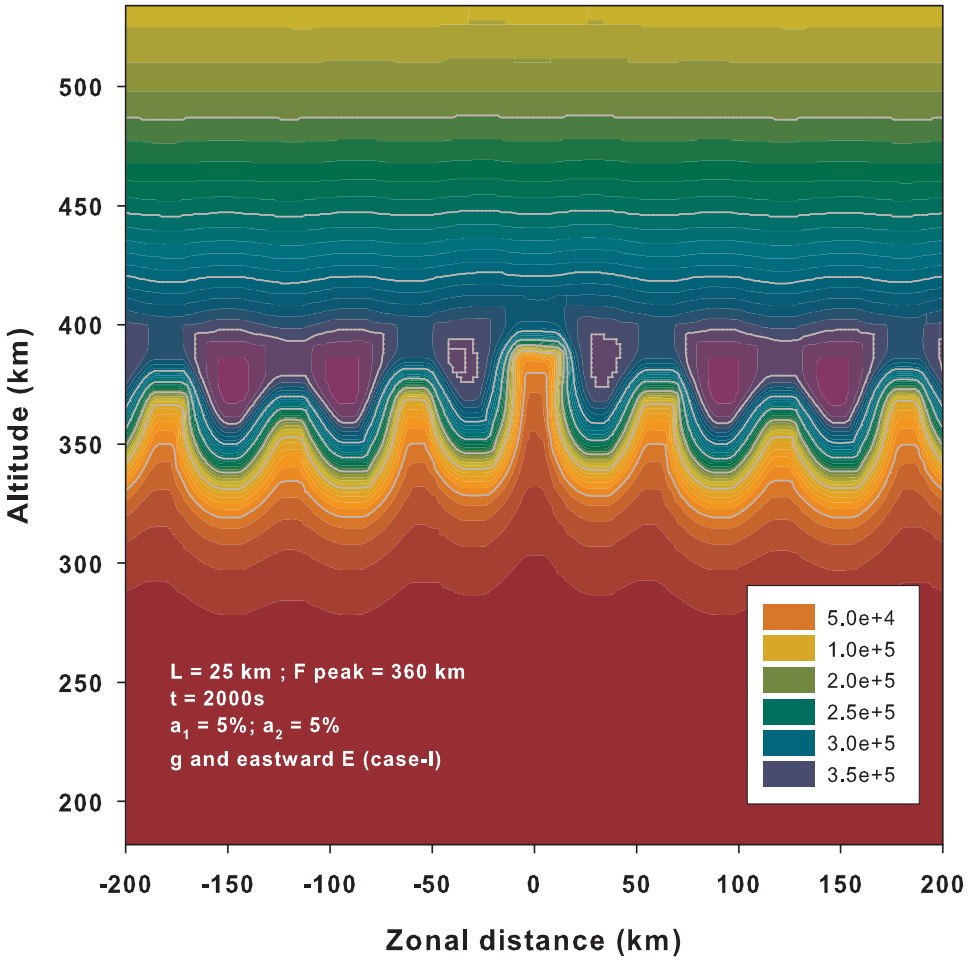

Figure 5.3: Isoelectron density contours at 2000 s (after the initiation of the instability processes) over the zonal and vertical plane. Gravity and vertical drift corresponding to zonal electric field as depicted in Case-I of Figure 2b are used as driving agencies. The initial perturbations in all the altitude regions are taken as described in Figure 2c. Plume is yet to develop.

spite of strong initial perturbation (35%) in the altitude region 280-360 km. This result reveals the need for the eastward electric field for the generation of plumes during pre-midnight hours.

In order to understand the development of plume event during other storm time case such as the case obtained in right side of Figure 5.1, various simulations are carried out using different electron density profiles with peak altitude ranging from 330 km to 370 km in steps of 10 km and minimum plasma scale lengths varying from 20 to 30 km in steps of 5 km. The required initial perturbation at the base altitude region for each case for the development of plasma plume events during pre-midnight hours (after $\sim$ 21:45 IST) which reach upto 450 km, are determined and given in Table 5.1. All the investigations were carried out with a typical eastward electric field conditions shown in case-I of Figure 5.2b. These investigations reveal that the required initial perturbations are in the range of

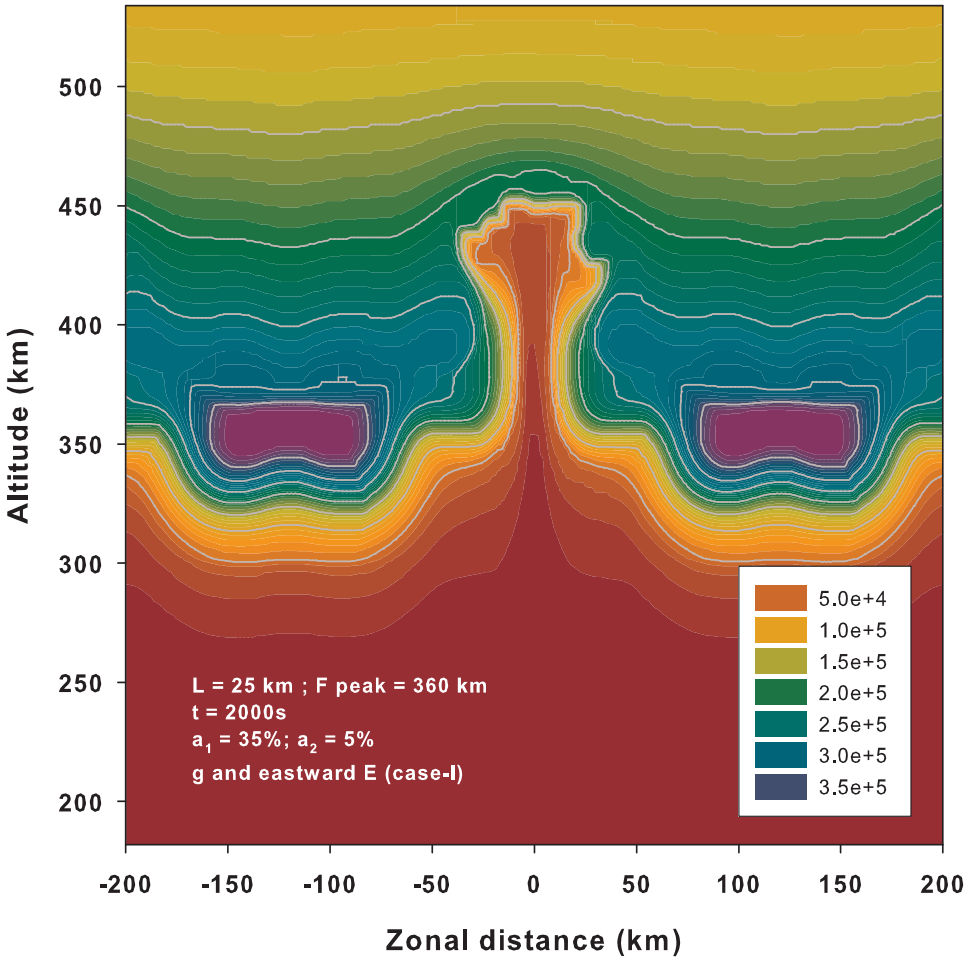

Figure 5.4: Same as Figure 5.3 except the initial perturbations in the altitude range of 280-360 km employed in the model are shown in Figure 2d and in the rest of the altitude regions as shown in Figure 2c. A developed plume is seen at the center.

15-75% of the ambient electron density depending upon the background F region peak altitude and minimum plasma scale length.

5.4 Discussion

It is well known that the seed perturbation is needed [e.g. *Ossakow*, 1981, and *Sekar et al.*, 1995] for the development of plasma bubble that manifests as plasma plumes in the VHF radar maps. Most of the earlier simulations [e.g. *Ossakow*, 1981; *Sekar et al.*, 1994; *Keskinen*, 2006] carried out during post-sunset hours where background ionospheric conditions such as the peak height of F layer and plasma scale length are found to be suitable for the generation of plasma bubble with the introduction of seed perturbation amplitude of about 5% of background electron density. However, Figure 5.3 reveals that such (5%) seed perturbation is not adequate for the generation of plume within

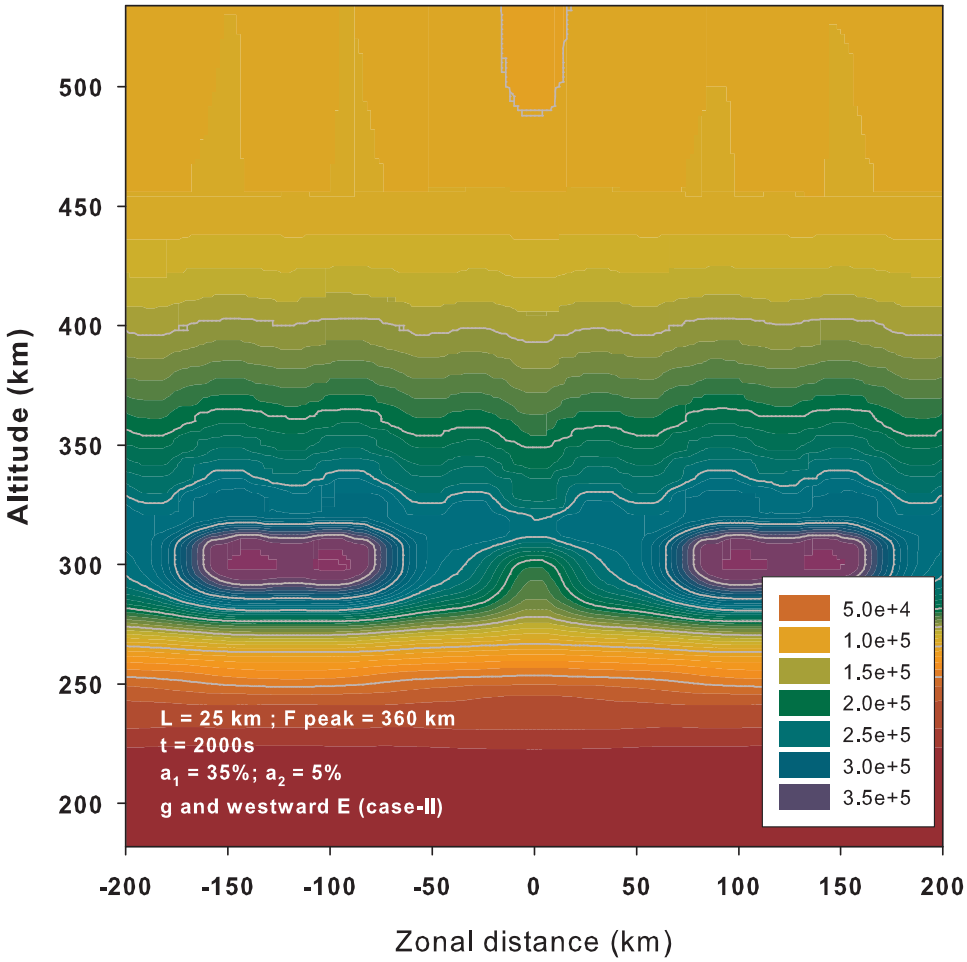

Figure 5.5: Same as Figure 5.4 except the vertical drift corresponding to zonal electric field is given as in Case-II of Figure 5.2b.

2000 s during pre-midnight hours. This is essentially due to the low peak height of the F region owing to the downward movement of the F layer during nighttime coupled with high value of plasma scale length. Even the inclusion of the reversal of the zonal electric field from westward to eastward during the overshielding event as in case-I of Figure 5.2b, is found to be insufficient for the development of plasma plume as revealed by Figure 5.3. However, the development of plasma plume was observed during pre-midnight hours on 7 January, 2005 after the reversal of the zonal electric field. Therefore, the required seed perturbation has to be more than 5% for the development of pre-midnight plume events. As indicated earlier, the amplitude of the seed perturbation was gradually varied to match with observation on 7 January, 2005. It was found that the development of plasma plume during pre-midnight hours matches with observation if the seed perturbation for the longer wavelength mode is 35% for an electron density profile with characteristic plasma scale length of 25 km. It is to be noted that peak height of the F layer is already taken to be on the higher side, i.e. 360 km. Therefore, it is apparent that the

required seed perturbation is large enough to be present in the ambient ionosphere. Under this circumstance, the presence of ESF irregularities developed during evening hours can provide such seed for the development of pre-midnight plume event. It is important to note that such irregularities are more often observed over a limited altitude region (where zonal plasma drift changes its polarity) similar to the present case in the altitude region of ($\sim$ 280-360 km) during 20:45-21:45 on 7 January, 2005. Therefore, the simulation presented in Figure 5.4 indicates that the pre-existing plasma irregularities developed in the evening hours can pre-seed the development of pre-midnight plume event. However, plasma density gradient and the reversal of the ionospheric electric field to eastward direction are also important conditions for the development of plume events. The reversal of ionospheric electric field appears to be a necessary condition as it helps in increasing the F layer height also contributing to the development through E$\times$B instability. However, by comparing the reversal of vertical drift corresponding to zonal electric field on ESF and non-ESF events presented in Figure 5.1, it is clear that the reversal of electric field alone is not a sufficient condition as evidenced by the simulation presented in Figure 5.5. The requirement of pre-seed in the form of presence of plasma irregularities even in a limited altitude region which matches with the base of the nighttime electron density profile as well as a suitable plasma density gradient are needed in addition to the electric field reversal for the development of pre-midnight plume event.

In the presence of storm time eastward electric field, the occurrence variability of plume events at pre-midnight hours appears to depend on the availability of large amplitude seed perturbation and also the background ionospheric conditions (refer Table 5.1) at the pre-midnight hours. The availability of large amplitude seed perturbation appears to largely depend on the generation of plasma irregularities during post-sunset hours. The amount of seed perturbation is essentially decided by the background ionospheric conditions at pre-midnight hours. Wide range of values (15-75$\%$) of pre-seed perturbation depending on background ionospheric conditions (Table 5.1) are needed for the formation of late night plume event. This condition may not be satisfied on all the nights particularly when the development of ESF is not conducive during post-sunset hours. Thus the absence of late night plasma plume event on February 12, 2004 described on the left hand side of Figure 5.1 is probably due to the absence of large amount of seed perturbation during late night hours as ESF was not triggered during post-sunset hours on that night. This is owing to the absence of significant eastward excursion of vertical drift associated with zonal electric field on February 12, 2004 while the vertical drift on January

7, 2005 was significantly upward after 20:15 IST which triggered [*Chakrabarty et al.*, 2006] the development of ESF at 20:40 IST. Thus the large difference in the vertical drift patterns on these two nights is largely responsible for the variations in the pre-seed during pre-midnight hours. However, unfavorable plasma density gradient during pre-midnight hours might also additionally inhibit the generation of pre-midnight plasma plume event on February 12, 2004.

In order to understand the development of late night plume event over Jicamarca magnetically disturbed night, an attempt was made by earlier simulation [*Sekar and Kelley*, 1998]. In that investigation, emphasis was given to understand the the confinement of structures and their day-to-day variabilities in terms of the combined effects of shears in the zonal plasma drift and different temporal zonal electric field patterns during post-sunset hours. The resurrection of plume event from the confined structures was also demonstrated in that investigation. As this investigation required initialization of the problem during post-sunset hours, it was difficult to quantify the pre-seed perturbation for resurrected plume event during post-midnight hours. In the present work, however, initialization is suitably done to quantify the development of plasma plume event during pre-midnight hours.

The importance of magnetic field integrated parameters is emphasized by the earlier investigations [*Sultan*, 1994; *Rappaport*, 1998]. Recent investigation using three-dimensional model [*Keskinen et al.*, 2003] reveals that the parallel conductivity effects slow down both linear and non-linear bubble evolution compared to two dimensional evolution. Thus, the limitation in the present investigation is that the simulations are performed in two dimensional plane. Therefore, the latitudinal distribution of ionospheric and thermospheric parameters are neglected in the present study. This limitation is likely to affect the results when the storm time effects are associated with disturbance dynamo which occurs with a larger time scale. However, when the storm time events are associated with overshielding effects with a time scale of $\sim$2000 s like the case discussed in the present study, the limitation imposes minimal corrections. Non-inclusion of the off-equatorial E region conductivities in the numerical model can, in principle, introduce uncertainty in quantifying the amount of pre-seed perturbation. However, since the present investigation pertains to pre-midnight hours (after 21:45 IST), the non-inclusion of E-region conductivity is not expected to largely underestimate the present quantification. In order to assess this, temporal variation of coupling factor between E and F regions is needed. One such calculation [*Sultan*, 1994] reveals that the coupling factor is more than

0.9 above 300 km altitude region after 21:30 LT. As the altitude of interest in the present investigation for the development of plume is well above 300 km, the required initial perturbation will be more by $\sim$10% in the presence of E-region conductivities. Further, in the presence of ESF pre-seed structures, the initial electron densities with altitudinal structures have to be introduced. However, average values in plasma scale length used in the present simulation are essentially to address large scale plasma plume development. In order to understand small scale structures, initial electron density with altitudinal structures needs to be introduced in future investigation. It may be noted that the observation did not reveal presence of bifurcations in the plume structure (see Figure 5.1R3). In order to study bifurcation of plume, if any, special techniques involving adequate grid size and control of numerical diffusion, as discussed in *Huba and Joyce* [2007], are needed.

5.5 Summary

Based on the observations of two storm-time electric field penetration events, a nonlinear numerical simulation model investigation reveals that the storm-induced eastward electric field during nighttime over dip-equatorial region is a necessary but not a sufficient condition for the development of pre-midnight plume structure. Pre-seeding in a localized altitude region is proposed to be a prime necessity for the development of pre-midnight plume event within half an hour of the eastward excursion of storm-time electric field. The confined ESF irregularities developed in the post-evening hours are suggested to provide such pre-seed. Wide range of values (15-75%) of pre-seed perturbation depending on the background ionospheric conditions are needed for the formation of plume events. This is suggested to account for the occurrence variability of storm-time plume events during pre-midnight hours.

Table 5.1: The amplitudes of perturbation needed for different combinations of scale lengths and F layer peak heights to generate a plasma plume that rises to ∼450 km within 2000 s under the influence of eastward overshielding electric field during pre-midnight hours

P lasma scale length in km (L)	Peak height of F layer (in km) during pre-midnight hours (during 21:30-22:00 IST)	Altitude region (km) where perturbation is applied	Required amplitude of Perturbation (in %)
20	330	250-330	65
	340	260-340	50
	350	270-350	40
	360	280-360	30
	370	290-370	15
25	330	250-330	70
	340	260-340	60
	350	270-350	50
	360	280-360	35
	370	290-370	25
30	330	250-330	75
	340	260-340	65
	350	270-350	55
	360	280-360	45
	370	290-370	30

P. S. Note that the limited altitude regions and the amplitudes correspond to large scale size (240 km) perturbation. In addition to this, 5% perturbation with a scale size of 60 km is applied in the entire altitude region.

Chapter 6

On the dependence of 777.4 nm airglow on ionospheric parameters

6.1 Background

The airglow lines of 630.0 nm and 777.4 nm have been extensively used to infer various parameters of thermosphere-ionosphere system. Over low latitudes, photometric observations [e.g *Kulkarni and Rao*, 1972; *Chandra et al.*, 1973s] are being used, in general, to deduce the ionospheric modulations caused by the equatorial plasma fountain and associated processes while the spectrometric Doppler observations [e.g. *Sahai et al.*, 1992 a, b; *Sridharan et al.*, 1994] particularly in 630.0 nm emission line have been used to derive thermospheric temperatures and winds. The imaging observations on these lines [e.g. *Weber et al.*,1978; *Mendillo et al.*, 1997; *Tinsley et al.*, 1997] are being extensively used to infer plasma depletions associated with equatorial spread F phenomenon. It is, therefore, necessary to understand the association of the ionospheric parameters with the nocturnal variations of thermospheric airglow emission lines.

The nocturnal variations of 630.0 nm airglow emission line intensity is fairly well-understood because of the wealth of observations. As mentioned in chapter 1, this emission line, during nighttime, is due to the dissociative recombination of O_2^+ with ambient electrons and thus the emission intensity is proportional to electron density. Further, it is well-established [*Barbier*, 1959] that the variations in the F region layer height are anti-correlated with the nocturnal variations of 630.0 nm emission line intensity. On the otherhand, barring a few observations by *Sahai et al.* [1981], the observations on 777.4 nm emission line intensity are not extensively compared with 630.0 nm observations.

The 777.4 nm emission line arises due to the radiative recombination of O^+ [*Tinsley et al.*, 1973] with ionospheric electrons and thus, this emission line intensity is proportional to the square of electron density as in the F region, the number densities of O^+ ions and electrons are approximately equal. The emission rate is believed to be independent of the F region layer height [e.g. *Tinsley et al.*, 1997; *Mendillo et al.*, 1985] and the intensity is proportional only to the peak electron concentration (N_{max}). *Mendillo et al.* [1985], while simulating the airglow signatures of plasma depletion, commented that, "to the first order, the vertical redistribution of plasma does not affect the total 777.4 nm emission while downward/upward motions enhance/reduce 630.0 nm emission intensity". Theoretical study involving equatorial ionospheric processes [*Bittencourt and Tinsley*, 1976] was carried out to understand the role of various physical parameters on the emission intensity of 135.6 nm which is also an outcome of radiative recombination. Extending the arguments to 777.4 nm emission intensity, *Tinsley et al.* [1997] concluded that the plasma diffusion associated with the plasma fountain effect and the trans-equatorial winds provide second order effects in the variation of N_{max} and thus, in the 777.4 nm intensity variations. Simultaneous observations of 777.4 nm and 630.0 nm emission lines [*Sahai et al.*, 1981] and the ionospheric parameters confirmed the earlier prediction of *Tinsley and Bittencourt* [1975]. In this study, *Sahai et al.*[1981] had related the intensity ratio $[(J_{777.4})^{1/2}/J_{630.0}]$ with F region layer height using the observations from tropical region. However, direct correlative study between the F region layer height variation and the nocturnal variations of 777.4 nm emission intensity is not attempted critically particularly from the region close to the dip equator. With an aim to exploring the possible dependence/independence of 777.4 nm intensity variation on the F layer height variation over India, airglow intensity variations at 630.0 nm and 777.4 nm recorded from Gadanki are scrutinized for a few cases and some selected, representative examples revealing mutual similarities/dissimilarities between 630.0 nm and 777.4 nm airglow intensity variations are presented. Occasional correspondences of 777.4 nm airglow emission intensity with F layer height variations are also pointed out.

6.2 Observations

Figure 6.1 depicts 630.0 nm and 777.4 nm airglow intensity variations over zenith recorded by the airglow photometer on 14th February, 2004. The horizontal axes for all the subplots correspond to time in IST. The vertical axes in the upper two subplots correspond

to photon counts which are proportional to the corresponding airglow emission intensities. The nocturnal intensity variation at 777.4 nm and 630.0 nm airglow emission lines are depicted respectively in the subplots 6.1A and 6.1B of figure 6.1. The emission intensities of both the emission lines decrease monotonically during the initial phase until 19:45 IST. Afterwards, the intensity gradually increases until a plateau region which starts around 22:00 IST. A sharp increase is observed in both the emission lines around 22:30 IST which persisted upto 23:00 IST. It is to be noted here that the typical airglow intensity at 777.4 nm is much less compared to that at 630.0 nm. This is owing to the fact that the radiative recombination (responsible for 777.4 nm emission) rate is orders of magnitude smaller than the dissociative recombination (responsible for 630.0 nm emission) rate. In addition to that, the detector is less sensitive at 777.4 nm compared to 630.0 nm. Thus, the statistical fluctuations in the 777.4 nm airglow intensity are more at 777.4 nm compared to 630.0 nm. The temporal variation of the observed F region peak altitudes (h_PF_2) from SHAR are denoted by solid squares in the subplot 6.1C of figure 6.1. The continuous curve in the subplot 6.1C corresponds to the fourth order polynominal fit of the discrete h_PF_2 values. Increase in h_PF_2 associated with the post-sunset enhancement is observed before 20:00 IST after which the layer decreases essentially due to westward electric field. A slight increase in F layer is also observed after 23:00 IST. It is to be noted here that during the descent of the average (fitted curve) F layer peak height by $\sim$ 160 km (from $\sim$ 540 km to $\sim$ 380 km during the interval 20:00-23:00 hr IST), 777.4 nm intensity increases by $\sim$5500 (from $\sim$ 3000 to 8500).

Figure 6.2 depicts a similar set of subplots for another night (27 March, 2003) from the same station wherein the increase in the 777.4 nm emission intensities is moderate compared to the previous case referred in figure 6.1. 777.4 nm airglow intensity, in this case, increases by $\sim$600 (from $\sim$ 2800 to 3400) corresponding to a h_PF_2 decrease of $\sim$180 km ($\sim$530 - 350 km during 19:30-21:30 hr IST). Furthermore, 777.4 nm airglow intensity decreases by $\sim$650 (from $\sim$3250 to 2600) during the interval 21:30-23:00 hr IST when average h_PF_2 increases by $\sim$70 km (from $\sim$350-420 km). However, the rate of increase in 630.0 nm emission intensity is large compared to the case in figure 6.1. Further, in this case, both increase and decrease of emission intensities are observed during the observational time.

Another interesting case (12 March, 2004), wherein the increase in 777.4 nm intensity (intensity changes from $\sim$ 2100 to 2500) is nominal (by 400 counts) in spite of a considerable descent in the layer height (from $\sim$ 500-320 km), is depicted in figure 6.3.

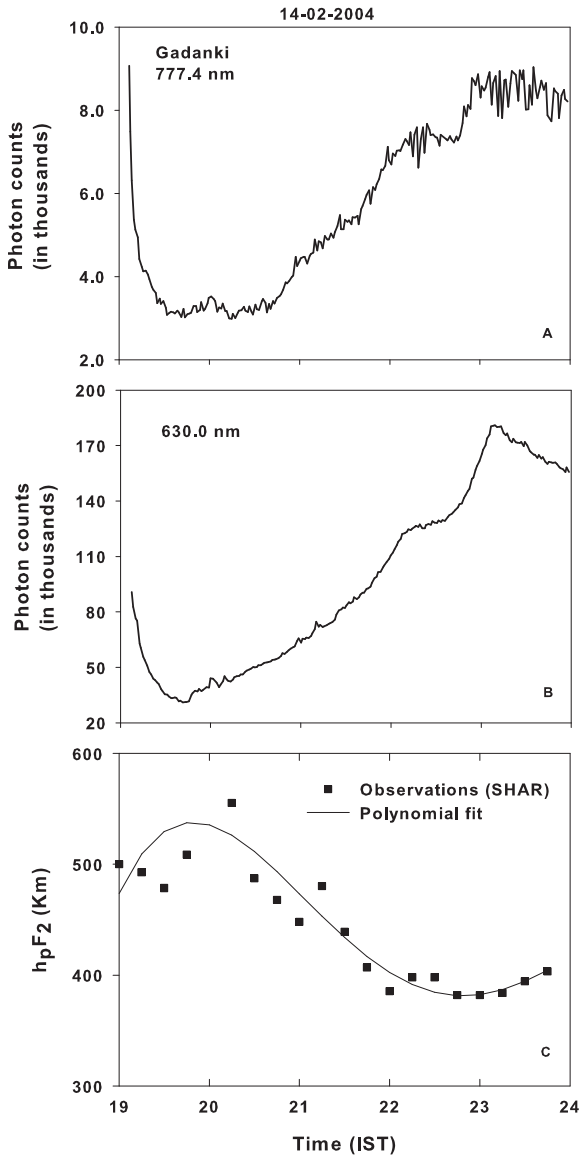

Figure 6.1: The nocturnal intensity variations in terms of photon counts of 777.4 nm and 630.0 nm airglow emissions over Gadanki on 14 February, 2004. The temporal variation of F region layer height over SHAR, a station 100 km east of Gadanki on the same night. The intensity variations at both the wavelengths are similar including the plateau region observed $\sim$ 22:30 IST.

The fourth case, shown in figure 6.4, reveals that the intensity variations of 630.0 nm and 777.4 nm emission lines on 15 March, 2004 are not similar unlike the previous cases. Further, when the F layer descends during 20:00-21:30 IST, a corresponding increase in 630.0 nm airglow intensity is observed. No such increasing trend is observed in 777.4 nm intensity during that interval.

The subplots are depicted in a similar way as that of the previous figures. The increase in the emission intensity of 630.0 nm after 21:00 - 24:00 IST is considerable while the increase in 777.4 nm intensity during that time period is not substantial and barely detectable by narrow band (0.3 nm) photometer.

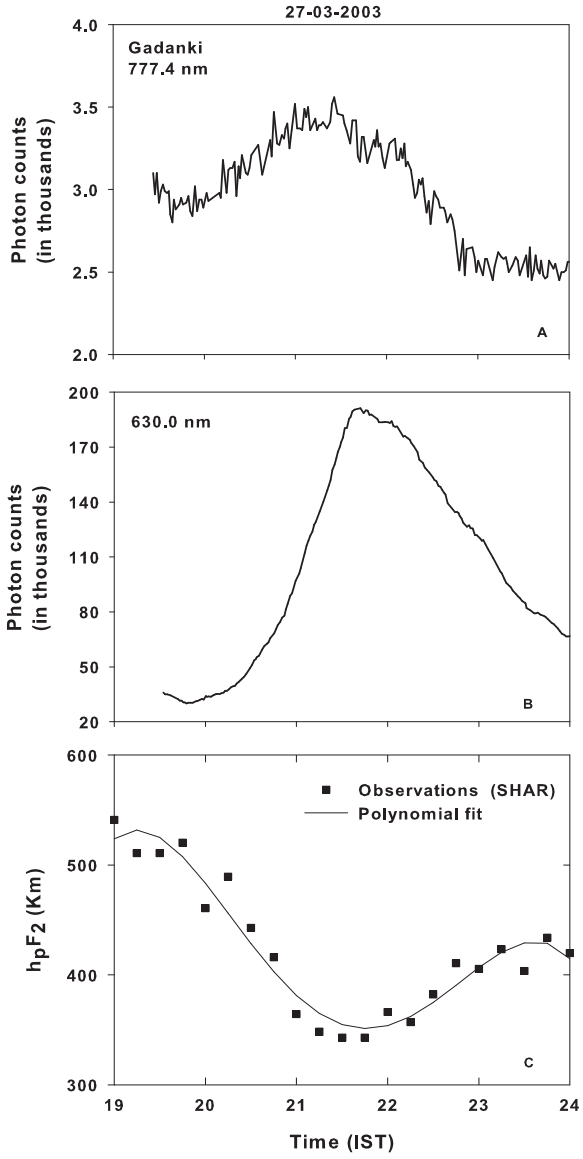

Figure 6.2: Similar to figure 6.1 but on 27 March, 2003. Note the similar responses in both the wavelengths during the ascending and descending phases of the F layer height.

Besides these four examples, a few other cases are obtained on non-ESF nights during the experimental campaigns. However, those cases fall under the four distinct categories brought out by figures 6.1 to 6.4.

6.3 Discussion

It is rather well-known that the nocturnal variation of 630.0 nm emission intensity increases/decreases with the decrease/increase of the F region layer height, e.g. h_PF_2. It is to be noted here that h_PF_2 is the virtual height at 0.834 of f_oF_2 and a routinely scaled

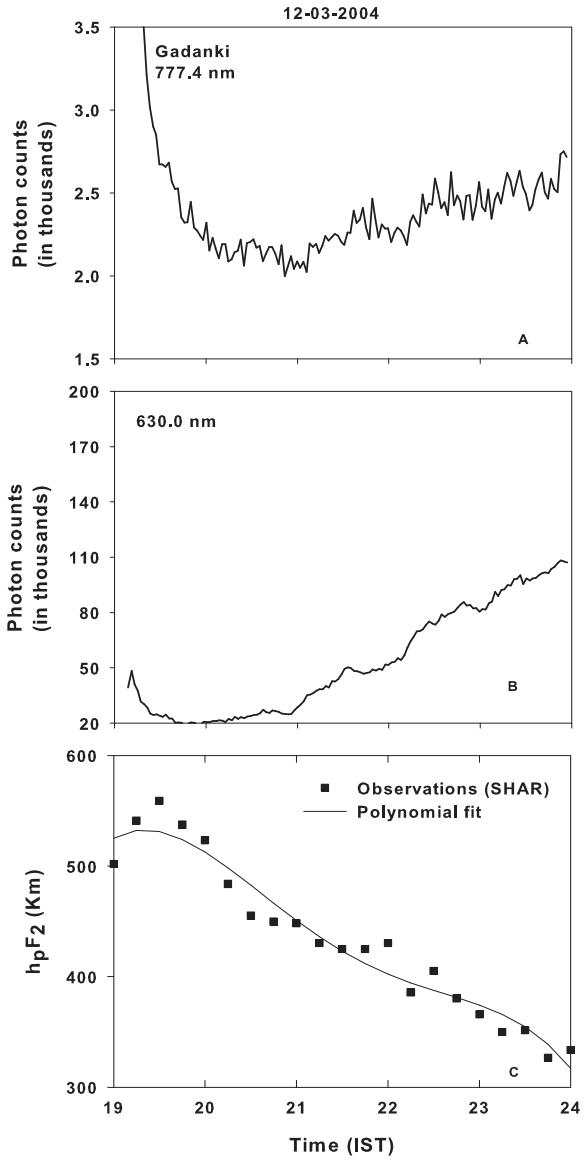

Figure 6.3: Similar to figures 6.1 and 6.2 but on 12 March, 2004. Note the increasing trend in both the wavelengths corresponding to the descent of the F layer height. However, the change in 777.4 nm airglow intensity is nominal on this occasion.

parameter. It corresponds to the temporal variabilities in the F peak height h_mF_2 and their values are known to agree well with each other [e.g.*Shirke*, 1963] especially during nighttime. It is clear from figures 6.1 and 6.2 that the nocturnal variations of 630.0 nm and 777.4 nm emission intensities are reasonably similar to one another on some occasions if the absolute values of the respective airglow intensities are ignored. This implies that the variations in 777.4 nm emission intensity are likely to depend on the layer height variations on some occasions similar to that of 630.0 nm emission line. Further, the observations of (i) a plateau region in figure 6.1 when the observed layer height remained nearly stationary and the (ii) decreasing trend in emission intensity when

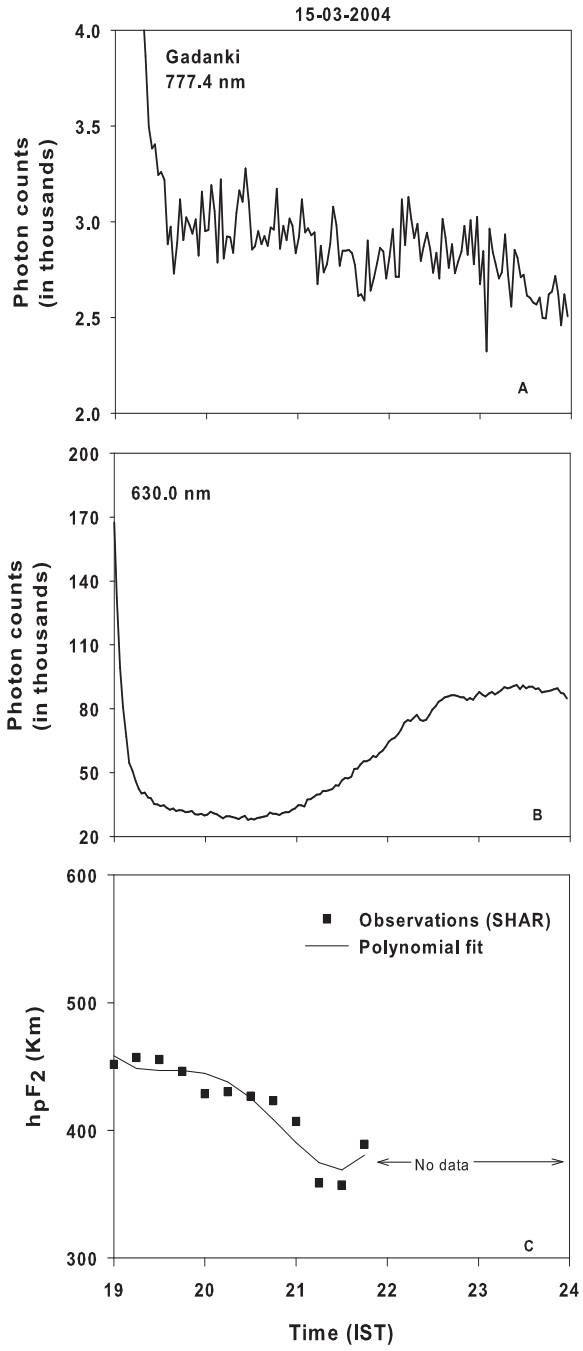

Figure 6.4: Similar to figures 6.1, 6.2, and 6.3 but on 15 March, 2004. Note the dissimilarities between the intensity variations at both the wavelengths.

the layer height increases (in figure 6.2) with time, suggest that the emission intensities may not be totally independent of the layer height variation. However, it is clear from figure 6.3 that the variation of 777.4 nm emission intensity is not substantial in spite of a large variation in the layer height. Further, from figure 6.4, no discernible relation between F layer height variation and 777.4 nm airglow intensity is obtained. Therefore, it can be assumed that temporal variation of 777.4 nm emission intensity may follow layer height variation conspicuously, on certain occasions when certain geophysical conditions

are presumably met. The conditions that suit for such dependence is discussed in the light of the electrodynamical control of the low latitude ionosphere.

The ground-based observations give rise to column- integrated intensities and thus the emission intensities are proportional to total electron content over an observing column. Let us assume a cylindrical vertical column for the present discussion. The variation of the F region height, which can represent the vertical plasma drift, is not expected to alter vertical column integrated intensity only when plasma flux movement is restricted in other two directions (namely zonal and meridional directions). However, the flux movement of plasma in other two directions is not restricted in general and in particular during ESF condition. The plasma bubble (depletion) during ESF is an outcome of nonlinear increase in vertical polarization drift resulting in the reduction of plasma concentration by displacing the plasma in zonal direction [*Ossakow*, 1981; *Sekar et al.*, 1994]. The fact, that the airglow emission intensities in 777.4 nm record the plasma depletion [*Tinsley et al.*, 1997] in the equatorial ionosphere, indicates the airglow emission lines responds to the changes in vertical plasma drift and, in turn, the variation in F region height. However, on the nights when the occurrence of ESF is inhibited the changes in the plasma flux along the zonal direction need not be drastic. Nevertheless, the plasma flux can be transported to the zonal direction in the presence of tilt (zonal gradient) in the ionosphere associated with the post sunset effects in the vertical drift [*Kelley et al.*, 1981]. This tilt is variable from day-to-day and depends on the post sunset variation in the vertical plasma drifts. During midnight, such tilts [e.g. *Iyer*, 1976] are expected to cause variation in the plasma drift. Most importantly, the aspect that plasma movement can take place along the magnetic flux tube assisted by the meridional wind should be considered in addressing the issue like the systematic relationship between 777.4 nm airglow intensity and variation of the peak height of F layer on certain occasions similar to 630.0 nm. Meridional wind can alter the plasma density at F region peak altitude which further triggers changes in the plasma density gradient and alters the plasma density concentration at F-region peak due to change in the vertical transport associated with nighttime westward electric field. In fact, the secondary maximum in N_{max} during nighttime (particularly more pronounced over Asian sector) was attributed [*Anderson*, 1971, 1973] to the combined effect of meridional wind and downward drift associated with the nighttime westward electric field. Thus the plasma density changes depend on the variability of these parameters. Therefore, the 777.4 nm airglow emission intensities, which essentially depend on the F-region plasma density, get affected by these processes. Thus the variabilities in the

transport of the plasma flux from the meridional direction may generate condition when the the primary assumption that vertical plasma drift does not change the total electron concentration along a vertical column does not hold any longer. Under that circumstance, 777.4 intensity may depend on the F-layer height variation in varying degrees depending upon the strength of the meridional wind system. The dependence of 777.4 nm airglow emission on the variabilities of the meridional plasma transport was attributed not to be of "first order" by earlier workers [*Mendillo et al.*, 1985; *Tinsley and Bittencourt*, 1975]. However, in view of the observations presented here, it can be inferred that the contributions from the above channels resulting in the variations of F layer height may not be "insignificant" on some occasions especially when strong meridional winds are present particularly during magnetically disturbed period.

In this context, it is relevant to discuss the variability observed in f_oF_2 at different longitudinal sectors [*Rastogi and Sanatani*, 1963; *Rao*, 1963]. More pronounced secondary maximum ~23:00 hr is observed over Indian longitude compared to American longitude. The observation of 777.4 nm intensity on 27 March, 2003 could as well be due to the pronounced secondary maximum in f_oF_2 which was shown by *Anderson et al.* [1971,1973] to be due to the combined effects of equatorward wind and westward electric field. In addition to that, most of the previous observations verifying the relationship between 777.4 nm airglow emission and the F layer height variations [e.g. *Sahai et al.*, 1981; *Tinsley et al.*, 1997] have been carried out from the tropical region in the American sector while the present measurement site is close to equatorial region in the Indian zone. Therefore, it is not clear whether the above-mentioned relationship will be equally valid for all longitudes. It requires more observations from different latitudinal sectors to establish such relationship on a firm footing.

Therefore, whether the varying degree of dependence between the F layer height and the 777.4 nm emission intensities on some occasions are due to meridional wind or longitudinal/latitudinal variabilities of electron concentration at F peak or a combination of both the factors needs to be understood. Further simultaneous experimental studies from different longitudinal and latitudinal sectors as well as theoretical investigations pertinent to Indian zone are needed to resolve this issue.

6.4 Summary

Nocturnal variation of airglow intensities of 630.0 nm and 777.4 nm line emission for a few cases from a low latitude station are presented and compared with F region layer height. On a few nights, the large scale intensity variations in 777.4 nm are remarkably similar to the intensity variation of 630.0 nm and seem to be anti-correlated with F layer height variation with varying degree. Thus, the apparently second order control of F region height variation on the intensity variation of 777.4 nm may become significant on occasions.

Bibliography

[1] Aarons, J., J. P. Mullen, J. P. Koster, R. F. daSilva, J. R. Medeiros, R. T. Medeiros, A. Bushby, J. Pantoja, J. Lanat and M. R. Paulson, Seasonal and geomagnetic control of equatorial scintillations in two longitudinal sectors, *J. Atmos. Terr. Phys.*, 42, 861, 1980

[2] Abdu, M., Major phenomena of the equatorial ionosphere-thermosphere system under disturbed conditions, *J. Atmos. Sol. Terr. Phys.*, 59, 1505, 1997

[3] Abdu, M. A., J. H. Sastri, J. MacDougall, I. S. Batista, J. H. A. Sobral, Equatorial disturbance dynamo electric field longitudinal structure and spread F: A case study from GUARA/EITS campaigns, *Geophys. Res. Lett.*, 24, 13, 1707, 1997

[4] Abdu, M. A., I. S. Batista, H. Takahashi, J. MacDougall, J. H. Sobral, A. F. Medeiros, and N. B. Trivedi, Magnetospheric disturbance induced equatorial plasma bubble development and dynamics: A case study in Brazilian sector, *J. Geophys. Res.*, 108(A12), 1449, doi:10.1029/2002JA009721, 2003

[5] Abdu, M. A., Equatorial ionosphere-thermosphere system: Electrodynamics and irregularities, *Adv. Space Res.*, 35, 771, 2005

[6] Abdu, M. A., K. N. Iyer, R. T. de Medeiros, I. S. Batista, and J. H. A. Sobral, Thermospheric meridional wind control of equatorial spread F and evening prereversal electric field, *Geophys. Res. Lett.*, 33, L07106, doi:10.1029/ 2005GL024835, 2006

[7] Alex, S., and R. Rastogi, Geomagnetic disturbance effect on equatorial spread-F, *Ann. Geophysicae*, 5A, 83, 1986

[8] Anderson, D. N., Daily variation of the ionospheric F_2 equatorial anomaly in the American Asian sectors, *Ph. D thesis* (submitted to University of Colorado), pp-108, 1971

[9] Anderson, D. N., A theoretical study of the ionospheric F-region equatorial anomaly, I, Theory, *Planet space. Sci.*, 21, 409, 1973a

[10] Anderson, D. N., A theoretical study of the ionospheric F-region equatorial anomaly, II, Results in the American and Asian sectors, *Planet space. Sci.*, 21, 421, 1973b

[11] Anderson, D. N., and D. W. Rusch, Composition of the night-time ionospheric F1-region near the magnetic equator, *J. Geophys. Res.*, 85, 569, 1980

[12] Anderson, D. N., A. Anghel, K. Yumoto, M. Ishitsuka, and E. Kudeki, Estimating daytime vertical E $\times$ B drift velocities in the equatorial F-region using ground-based magnetometer observations, *Geophys. Res. Lett.*, 29, 12, 1596, 10.1029/2001GL014562, 2002

[13] Anghel, A. et al., Interplanetary electric fields and their relationship to low-latitude electric fields under disturbed conditions, *J. Atmos. Sol-Terr. Phys.*, doi: 10.1016/j.jastp.2006.08.018, 2007

[14] Appleton, E. V., Two anomalies in the ionosphere, *Nature*, 157, 691, 1946

[15] Argo, P. E.,and M. C. Kelley, Digital ionosonde observations during equatorial spread-F, *J. Geophys. Res.*, 91, 5539, 1986

[16] Barbier, D.: 'Recherches Sur la raie 6300 de la luminescence atmospherique nocturne', *Ann. Geophysicae*, 15, 179, 1959.

[17] Basu, S., Su. Basu, K. M. Groves, H.-C. Yeh, S.-Y. Su, F. J. Rich, P. J. Sultan, and M. J. Keskinen, Response of the equatorial ionosphere in the South Atlantic region to the great magnetic storm of July 15, 2000, *Geophys. Res. Lett.*, 28, 3577, 2001

[18] Basu, Sunanda, Santimay Basu, C. E. Valladares, H. -C. Yeh, S. -Y. Su, E. MacKenzie, P. J. Sultan, J. Aarons, F. J. Rich, P. Doherty, K. M. Groves, and T. W. Bullett, Ionospheric effects of major magnetic storms during the International Space Weather Period of September and October 1999: GPS observations, VHF/UHF scintillations, and in situ density structures at middle and equatorial latitudes, *J. Geophys. Res.*, 106, 30389, 2001

[19] Becker-Guedes, F., Y. Sahai, P. R. Fagundes, W. L. C. Lima, V. G. Pillat, J. R. Abalde, and J. A. Bittencourt, Geomagnetic storm and equatorial spread-F, *Ann. Geophysicae*, 22: 3231, 2004

[20] Bertin, F., L. Kersley, P. R. Rees and J. Testud, Meteorological jet stream as source of medium scale gravity-waves in thermosphere - an experimental study, *J. Atmos. Terr. Phys.*, 40, 1161, 1978

[21] Biondi, M. A., and J. W. Meriwether, Jr., Measured response of the equatorial thermospheric temperature to geomagnetic activity and solar flux changes, *Geophys. Res. Lett.*, 12, 267, 1985

[22] Biondi, M. A., and D. P. Sipler, Horizontal and vertical winds and temperatures in the equatorial thermosphere: Measurements from Natal, Brazil during August-September, *Planet. Space Sci.*, 33, 817, 1985

[23] Bittencourt, J. A., and B. A. Tinsley, Tropical F region winds from OI 1356 A^o and [OI] 6330 A^o emissions: 1 Theory, *J. Geophys. Res.*, 81, 3781, 1976

[24] Bittencourt, J. A., and M. A. Abdu, A theoretical comparison between apparent and real vertical ionization drift velocities in the equatorial F region, *J. Geophys. Res.*, 86, A4, 2451, 1981

[25] Blanc, M., and A. D. Richmond, The ionospheric disturbance dynamo, *J. Geophys. Res.*, 85, 1669, 1980

[26] Book, D. L., J. P. Boris, and K. Hain, Flux-corrected transport, II: Generalizations of the method, *J. Comput. Phys.*, 18, 248, 1975

[27] Boris, J. P., and D. L. Book, Flux-corrected transport, I: SHASTA, a fluid transport algorithm that works, *J. Comput. Phys.*, 11, 38, 1973

[28] Boris, J. P., and D. L. Book, Flux-corrected transport, III: Minimal-error FCT algorithms, *J. Comput. Phys.*, 20, 397, 1976

[29] Brice, N. M., Bulk motion of the magnetosphere, *J. Geophys. Res.*, 72, 5193, 1967.

[30] Buonsanto, M. J., Ionospheric storms - a review, *Space Sci. Rev.*, 88, 563, 1999

[31] Burch, J. L., S. B. Mende, D. G. Mitchell, T. E. Moore, C. J. Pollock, B. W. Reinisch, B. R. Sandel, S. A. Fuselier, D. L. Gallagher, J. L. Green, J. D. Perez, P. H. Reiff, Views of Earth's magnetosphere with the IMAGE satellite, *Science*, 291, 619, 2001

[32] Burch., J. L., J. Goldstein, B. R. Sandel, Cause of plasmasphere corotation lag, *Geophys. Res. Lett.*, 31, L05802, doi:10.1029/2003GL019164, 2004

[33] Burch, J. L., Magnetospheric imaging: Promise to reality, *Rev. Geophys.*, 43, RG/3001, 2004RG000160, 2005

[34] Burke, W.J., N. C. Maynard, M. P. Hagan, R. A. Wolf, G. R. Wilson, L. C. Gentile, M. S. Gussenhoven, C. Y. Huang, T. W. Garner, F. J. Rich, Electrodynamics of the inner magnetosphere observed in the dusk sector by CRRES and DMSP during the magnetic storm of June 46, 1991. *J. Geophys. Res.* 103, 29399, 1998

[35] Burke, W.J., Penetration electric fields: A VollandStern approach, *J. Atmos. Sol-Terr. Phys.*, doi:10.1016/j.jastp.2006.09.013, 2007

[36] Burke, W. J., C. Y. Huang, F. A. Marcos, and J. O. Wise, Interplaneatry control of thermospheric densities during large magnetic storms, *J. Atmos. Sol-Terr. Phys.*, 69, 279, 2007

[37] Carpenter, D. L., and C. G. Park, On what ionosphere workers should know about the plasmapause-plasmasphere, *Rev. Geophys. Space Phys.*, 11: 133, 1973

[38] Chakrabarty, D., R. Sekar, R. Narayanan, T. K. Pant, and K. Niranjan, Thermospheric gravity wave modes over low and equatorial latitudes during daytime, J. Geophys. Res., 109, A12309, doi:10.1029/2003JA010169, 2004

[39] Chakrabarty, D., R. Sekar, R. Narayanan, C.V. Devasia and B.M. Patan, Evidence for the interplanetary electric field effect on the OI 630.0nm airglow over latitude, *J. Geophys. Res.*, 110, A11301,doi10.1029/2005JA011221, 2005

[40] Chakrabarty, D., R. Sekar, R. Narayanan, A. K. Patra, and C. V. Devasia, Effects of interplanetary electric field in the development of an equatorial spread F event, *J. Geophys. Res.*, 111, A12316, doi: 10.1029/2006JA011884, 2006

[41] Chandra, S., E. I. Reed, B. E. Troy, Jr., and J. E. Blamont, Equatorial airglow and ionospheric geomagnetic anomaly, *J. Geophys. Res.*, 78, 4630, 1973s

[42] Chandra, H, Girija Rajaram, and R. G. Rastogi, Electron density distribution over the magnetic equator, *Ind. J. Radio Space Phys.*, 2, 243, 1973

[43] Daglis, I. A., and R. M .Thorne, The terrestrail ring current : Origin, formation, and decay, *Rev. Geophys.*, 37, 4, 1999

[44] Daglis, I. A., Ring current dynamics, *Space Sci. Rev.*, 124: 183, 2006

[45] De Michelis, P., I. A. Daglis, G. Consolini, Average terrestrial ring current derived from AMPTE/CCE-CHEM measurements, *J. Geophys. Res.*, 102(A7), 14103, 10.1029/96JA03743, 1997

[46] de Paula, E. R., K. N. Iyer, D. L. Hysell, F. S. Rodrigues, E. A. Kherani, A. C. Jardim, L. F. C. Rezende, S. G. Dutra, and N. B. Trivedi, Multi-technique investigations of storm-time ionospheric irregularities over the São Luís equatorial station in Brazil, *Ann. Geophysicae*, 22, 3513, 2004

[47] Dessler, A. J., and E. N. Parker, Hydromagnetic theory of geomagnetic storms, *J. Geophys. Res.*, 64, 2239, 1959

[48] Devasia, C. V., N. Jyoti, K. S. V. Subbarao, K. S. Viswanathan, Diwakar Tiwari, R. Sridharan, On the plausible linkage of thermospheric meridional winds with the equatorial spread F, *J. Atmos. Sol-Terr. Phys.*, 64, 1, 2002

[49] Earle, G. D., and M. C. Kelley, Spectral studies of the sources of ionospheric electric fields, *J. Geophys. Res.*, 92, 213, 1987

[50] Ebihara, Y., M. -C. Fok, R. A. Wolf, T. J. Immel, and T. E. Moore, Influence of ionospheric conductivity on the ring current, *J. Geophys. Res.*, 109, A08205, doi:10.1029/2003JA010351, 2004

[51] Emmert, J. T., B. G. Fejer, C. G. Fesen, G. G. Shepherd, and B. H. Solheim, Climatology of middle- and low-latitude daytime F region disturbance neutral winds measured by Wind Imaging Interferometer (WINDII), *J. Geophys. Res.*, 106(A11), 24701, 2001

[52] Farley, D. T., A theory of electrostatic fields in a horizontally stratified ionosphere subject to a vertical magnetic field, *J. Geophys. Res.*, 64, 1225, 1959

[53] Farley, D. T., A theory of electrostatic fields in the ionosphere at nonpolar geomagnetic latitudes, *J. Geophys. Res.*, 65, 869, 1960

[54] Fejer, B. G., D. T. Farley, R. F. Woodman, and C. Calderon, Dependence of equatorial F-region vertical drifts on season and solar cycle, *J. Geophys. Res.*, 84, 5792, 1979

[55] Fejer, B. G., C. A. Gonzales, D. T. Farley, M. C. Kelley, and R. F. Woodman, Equatorial electric fields during magnetically disturbed conditions 1. The effect of the interplanetary magnetic field, *J. Geophys. Res.*, 84, A10, 5797,1979

[56] Fejer, B. G., D. T. Farley, C. A. Gonzales, R. F. Woodman, and C. Calderon, F region east-west drifts at Jicamarca, *J. Geophys. Res.*, 86, 215, 1981

[57] Fejer, B. G., M. F. Larsen, and D. T. Farley, Equatorial disturbance dynamo electric fields, *Geophys. Res. Lett.*, 10, 537, 1983

[58] Fejer, B. G., R. W. Spiro, R. A. Wolf, and J. C. Foster, Latitudinal variation of perturbation electric fields during magnetically disturbed periods: 1986 SUNDIAL observation and model results, *Ann. Geophys.*, 8, 441, 1990

[59] Fejer, B. G., E. R. de Paula, S. A. Gonzalez, and R. F. Woodman, Average vertical and zonal F region plasma drifts over Jicamarca, *J. Geophys. Res.*, 96, 13901, 1991

[60] Fejer, B. G., E. R. de Paula, R. A. Heelis, and W. B. Hanson, Global equatorial ionospheric vertical plasma drifts measured by the AE-E satellite, *J. Geophys. Res.*, 100, 5769, 1995

[61] Fejer, B. G., The electrodynamics of the low latitude ionosphere: Recent results and future challenges, *J. Atmos. Sol-Terr. Phys.*, 59, 1465, 1997

[62] Fejer, B. G., and L. Scherliess, Time Dependent Response of Equatorial Ionospheric Electric Fields to Magnetospheric Disturbances, *Geophys. Res. Lett.*, 22, 851, 1995

[63] Fejer, B. G., and L. Scherliess, Empirical models of storm-time equatorial zonal electric fields, *J. Geophys. Res.*, 102, 24047, 1997

[64] Fejer, B., L. Scherliess, and E. R. de Paula, Effects of the vertical plasma drift velocity on the generation and evolution of equatorial spread F, *J. Geophys. Res.*, 104, 19859, 1999

[65] Fejer, B. G., L. Scherliess, Mid- and low-latitude prompt-penetration ionospheric zonal plasma drifts, *Geophys. Res. Lett.*, 25(16), 3071, 10.1029/98GL02325, 1998

[66] Fejer B. G.,and J. T. Emmert, Low-latitude ionospheric disturbance electric field effects during the recovery phase of the 1921 October 1998 magnetic storm, *J. Geophys. Res.*, 108 (A12), 1454, doi:10.1029/2003JA010190, 2003

[67] Fejer, B. G., J. de Souza, A. S. Santos, and A. E. Costa Perreira, Climatology of F Region zonal plasma drifts over Jicamarca, *J. Geophys. Res.*, 110, A12310, doi:10.1029/2005JA011324, 2005

[68] Fok, M., Y. Ebihara, and T. E. Moore, Inner magnetospheric plasma interactions and coupling with the ionosphere, *Adv. Polar Upper Atmos. Res.*, 19, 106, 2005

[69] Fox, N. J., M. Peredo, and B. J. Thompson, Cradle to grave tracking of the January 6-11, 1997 Sun-Earth connection event, *Geophys. Res. Lett.*, 25, 2461, 1998

[70] Friedel, R. H., H. Korth, M. G. Henderson, M. F. Thompsen, and J. D. Scudder, Plasma sheet access to the inner magnetosphere, *J. Geophys. Res.*, 106, A4, 5845, 2001

[71] Goldstein, J., R.W. Spiro, P.H. Reiff, R.A. Wolf, B.R. Sandel, J. W. Freeman, R. L. Lambour, IMF-driven overshielding electric field and the origin of the plasmaspheric shoulder of May 24, 2000. *Geophys. Res. Lett.* 29, 1819, 2002

[72] Goldstein, J., Inner magnetospheric shielding, penetration electric field, and the plasmasphere, *Web resource*, JEM (Student)tutorial, June 23, 2002web

[73] Goldstein, J., B. R. Sandel, M. R. Hairston, and P. H. Reiff, Control of plasmaspheric dynamics by both convection and sub-auroral polarization stream, *Geophys. Res. Lett.*, 30(24), 2243, doi:10.1029/2003GL018390, 2003

[74] Goldstein, J., J. L. Burch, and B. R. Sandel, Magnetospheric model of subauroral polarization stream, *J. Geophys. Res.*, 110(A9), A09222, doi:10.1029/2005JA011135, 2005

[75] Goldstein, J., Plasmasphere response: Tutorial and review of recent imaging results, *Space Sci. Rev.*, 124: 203, 2006

[76] Gonzales, C. A., M. C. Kelley, B. G. Fejer, J. F. Vickrey, and R. F. Woodman, Equatorial electric fields during magnetically disturbed conditions 2. Implications of simultaneoues auroral and equatorial mesurements, *J. Geophys. Res.*, 84, A10, 5803,1979

[77] Gosling J. T., The solar flare myth, *J. Geophys. Res.*, 98, 18949, 1993

[78] Gouin, P. and P. N. Mayaud, A propos de lexistence possible dun contre electrojet aux latitudes magnetiques equatoriales, *Ann. Geophys.*, 23, 41, 1967

[79] Grebowsky, J. M., Model study of plasmapause motion, *J. Geophys. Res.*, 75, 4329, 1970

[80] Gurubaran, S., Investigation of low latitude thermosphere-ionosphere system, *Ph. D. thesis*, Gujarat Univ., 1993

[81] Gurubaran, S., The equatorial counter-electrojet: Part of a world-wide current system?, *Geophys. Res. Lett.*, 29, 9, 1337, 10.1029/2001GL014519, 2002

[82] Haerendel, G., Theory of equatorial spread F, *Report: Max-Planck Inst. Fur Phys. and Astrophys., Garching, Germany*, 1974

[83] Hanson, W. B., and R. J. Moffett, Ionization transport effects in the equatorial F-region, *J. Geophys. Res.*, 71, 5559, 1966

[84] Herraro, F. A., and J. W. Meriwether, The 630nm MIG and the vertical neutral wind in the nighttime thermosphere at low latitude, *Geophys. Res. Lett.*, 21, 97, 1994

[85] Herrero, F. A., and J. W. Meriwether Jr., 6300A Airglow meridional intensity gradients, *J. Geophys. Res.*, 85, 4191, 1980

[86] Hines, C. O., Internal atmospheric gravity waves at ionospheric heights, *Can. J. Phys.*,38, 1441-1481, 1960

[87] Hines, C. O., Dynamical heating of the upper atmosphere. J. Geophys. Res., 70, 177, 1965.

[88] Hocke, K. and K. Schlegel, A review of atmospheric gravity waves and travelling ionospheric disturbances: 1982-1995, *Ann. Geophysicae*, 14, 917, 1996

[89] Huang, C. S., and M. C. Kelley, Nonlinear evolution of equatorial spread F, 2. Gravity wave seeding of Rayleigh-Taylor instability, *J. Geophys. Res.*, 101, 293, 1996

[90] Huang, C.-S., J. C. Foster, and M. C. Kelley, Long-duration penetration of the interplanetary electric field to the low-latitude ionosphere during the main phase of magnetic storms, *J. Geophys. Res.*, 110, A11309, doi:10.1029/2005JA011202, 2005

[91] Huang, C.-S., et al., Penetration electric fields: Efficiency and characteristic time scale, *J. Atmos. Sol-Terr. Phys.*, doi:10.1016/j.jastp.2006.08.016, 2007

[92] Huba, J. D., and S. L. Ossakow, On the generation of 3-m irregularities during equatorial spread F by low frequency drift waves, *J. Geophys. Res.*, 84, 6697, 1979

[93] Huba, J. D., and G. Joyce, Equatorial spread F modeling: Multiple bifurcated structures, secondary instabilities, large density bite-outs, and supersonic flows, *Geophys. Res. Lett.*, 34, L07105, doi:10.1029/2006GL028519, 2007

[94] Iijima, T., and T. A. Potemra, Large-scale characteristic of field-aligned currents at northern high latititudes observed by Triad, J. Geophys. Res., 83, 599, 1978

[95] Immel, T. J., E. Sagawa, S. L. England, S. B. Henderson, M. E. Hagan, S. B. Mende, H. U. Frey, C. M. Swenson, and L. J. Paxton, Control of equatorial ionospheric morphology by atmospheric tides, *Geophys. Res. Lett.*, 33, L15108, doi:10.1029/2006GL026161, 2006

[96] Iyemori, T., and D. R. K. Rao, Decay of the Dst field of geomagnetic disturbance after substorm onset and its implication to storm-substorm relation, *Ann. Geophys.*, 14, 618, 1996

[97] Iyer, K. N., R. M. Jadav, A. K. Jadeja, P. K. Manoharan, Som Sharma and Hari Om Vats, Space weather effects of coronal mass ejections, *J. Astrophys. Astr.*, 27, 219, 2006

[98] Iyer, K. N., Studies of geomagnetism and ionosphere at low latitudes, *Ph. D. thesis*, Gujarat Univ., 1976

[99] Jaggi, R. K., and R. A. Wolf, Self-consistent calculation of the motion of a sheet of ions in the magnetosphere, *J. Geophys. Res.*, 78, 2852, 1973

[100] Kahler S. W., Solar flares and coronal mass ejections, *Ann. Rev. Astr. Ap.*, 30, 113, 1992

[101] Kamide, Y., et al., Current understanding of magnetic storms: Storm-substorm relationships, *J. Geophys. Res.*, 103, 17705, 1998

[102] Kane, R. P., Global evolution of F2-region storms, *J. Atmos. Terr. Phys.*, 35, 1953, 1973a

[103] Kane, R. P., Global evolution of the DS component during geomagnetic storms, *J. Geophys. Res.*, 78, 5585, 1973b

[104] Kavanagh, L. D. J., J.W. Freeman, and A.J. Chen, Plasma flow in the magnetosphere, *J. Geophys. Res.*, 73, 5511, 1968

[105] Kelley, M. C., B. G. Fejer, and C. A. Gonzales, An explanation for anomalous equatorial ionospheric electric fields associated with a northward turning of the interplanetary magnetic field, *Geophys. Res. Lett.*, 6, 4, 301, 1979

[106] Kelley, M. C., M. F. Larsen, C. A. LaHoz and J. P. McClure, Gravity wave initiation of equatorial spread F: A case study, *J. Geophys. Res.*, 86, 9087, 1981

[107] Kelley, M. C. et al., The Condor equatorial spread F Campaign: Overview of results of the large-scale measurements, *J. Geophys. Res.*, 91, 5487, 1986

[108] Kelley, M. C., The Earths Ionosphere, *Int. Geophys. Ser., Academic Press, San Diego, California*, 43, 1989

[109] Kelley, M. C., J. J. Makela, J. L. Chau, and M. J. Nicolls, Penetration of the solar wind electric field into the magnetosphere/ionosphere system, *Geophys. Res. Lett.*, 30, 4, 1158, doi:10.1029/2002GL016321, 2003

[110] Kelley, M.C., et al., Multi-longitude case studies comparing the interplanetary and equatorial ionospheric electric fields using an empirical model, *J. Atmos. Sol-Terr. Phys.*, doi:10.1016/j.jastp.2006.08.014, 2007

[111] Keskinen, M. J., S. L. Ossakow, and B. G. Fejer, Three-dimensional nonlinear evolution equatorial ionospheric spread-F bubbles, *Geophys. Res. Lett.*, 30(16), 1855, doi:10.1029/2003GL017418, 2003

[112] Keskinen, M. J., S. L. Ossakow, B. G. Fejer, and John Emmert, Evolution of equatorial ionospheric bubbles during a large auroral electrojet index increase in the recovery phase of a magnetic storm, *J. Geophys. Res.*, 111, A02303, doi:10.1029/2005JA011352, 2006

[113] Khan, H., and S. W. H. Cowley, Observations of the response time of high latitude ionospheric convection to variations in the interplanetary magnetic field using EISCAT and IMP-8 data, *Ann. Geophys.*, 17, 1306, 1999

[114] Kikuchi, T., H. Lühr, T. Kitamura, O. Saka, and K. Schlegel, Direct penetration of the polar electric field to the equator during a DP 2 event as detected by the auroral and equatorial magnetometer chains and the EISCAT radar, *J. Geophys. Res.*, 101, 17161, 1996

[115] Kikuchi, T., H. Lühr, K. Schlegel, H. Tachihara, M. Shinohara, and T.-I. Kitamura, Penetration of auroral electric fields to the equator during a substorm, *J. Geophys. Res.*, 105, 23251, 2000

[116] Kikuchi, T., K. K. Hashimoto, T. -I. Kitamura, H. Tachihara, and B. Fejer, Equatorial counterelectrojets during substorms, *J. Geophys. Res.*, 108(A11), 1406, doi:10.1029/2003JA009915, 2003

[117] Killeen, T. L., Energetics and dynamics of the earths thermosphere, *Rev. Geophys. Space Phys.*, 25, 433, 1987

[118] Killeen, T. L. and R. M. Johnson, Upper atmospheric waves, turbulence and winds : importance for mesospheric and thermospheric studies, *Rev. Geophys. And Space Phys.*, July, 737-743, 1995

[119] Kivelson, M. G., and C. T. Russell (eds.), *Introduction to Space Physics*, Cambridge University Press, Cambridge, 1995

[120] Koskinen, H. E. J., and K. E. J. Huttunen, Geoeffectivity of coronal mass ejections, *Space Sci. Rev.*, 124: 169, 2006

[121] Krishna Murthy, B. V., S. S. Hari, and V. V. Somayajulu, Nighttime equatorial thermospheric meridional winds from ionospheric h′F data, *J. Geophys. Res.*, 95, A4, 4307, 1990

[122] Krishna Murthy, B. V., and S. S. Hari, Electric fields in the low latitude F-region, *Adv. Space Res.*, 18, 93, 1996

[123] Kulkarni, P. V., and V. R. Rao, 6300 ^{o}A night airglow emission over the magnetic equator, *Ann. Geophys.*, 28, 475, 1972

[124] Laakso, H., T. L. Aggson, R. F. Pfaff, and W. B. Hanson, Downdrafting plasma flow in equatorial bubbles, *J. Geophys. Res.*, 99, 11507, 1994

[125] Le Huy, M., and C. Amory-Mazaudier, Magnetic signature of the ionospheric disturbcance dynamo at equatorial latitudes: "D_{dyn}", *J. Geophys. Res.*, 110, A10301, doi: 10.1029/2004JA010578, 2005

[126] Lester, M., O. de la Beaujardiere, J. C. Foster, M. P. Freeman, H. Luhr, J. M. Ruohoniemi, and W. Swider, The response of the large scale ionospheric convection pattern to changes in the IMF and substorms: Results from the SUNDIAL 1987 campaign, *Ann. Geophys.*, 11, 556, 1993

[127] Liu, H., H. Lühr, S. Watanabe, W. Köhler, V. Henize, and P. Visser, Zonal winds in the equatorial upper thermosphere: Decomposing the solar flux, geomagnetic activity, and seasonal dependencies, *J. Geophys. Res.*, 111, A07307, doi:10.1029/2005JA011415, 2006

[128] Lui, A. T. Y., R. W. McEntire, and S. M. Krimigis, Evolution of ring current during two geomagnetic storms, *J. Geophys. Res.*, 92, 7459, 1987

[129] Lyon, A., N. Skinner, and R. Wright, The belt of equatorial spread-F, *J. Atmos. Terr. Phys.*, 19, 145, 1960

[130] Martinis, C. R., M. J. Mendillo and J. Aarons, Toward a synthesis of equatorial spread F onset and suppression during geomagnetic storms, *J. Geophys. Res.*, 110, A07306, doi:10.1029/2003JA010362, 2005

[131] Maruyama, N., A. D. Richmond, T. J. Fuller-Rowell, M. V. Codrescu, S. Sazykin, F. R. Toffoletto, R. W. Spiro, and G. H. Millward, Interaction between direct penetration and disturbance dynamo electric fields in the storm-time equatorial ionosphere, *Geophys. Res. Lett.*, 32, L17105, doi:10.1029/2005GL023763, 2005

[132] Mayaud, P. N., Derivation, meaning and use of geomagnetic indices, *Geophysical Monograph*, 22, AGU, 1980

[133] Maynard, N.C., A. J. Chen, Isolated cold plasma regions: observations and their relation to possible production mechanisms, *J. Geophys. Res.* 80, 1009, 1975

[134] McFarland, M., D. L. Albritton, F. C. Fehsenfeld, E. E. Ferguson, and A. L. Schmeltekopf, Flow-drift technique for ion mobility and ion-molecular reaction rate coefficient measurements. II., Positive ion reactions of N^+, O^+, and $N_2{}^+$ with O_2 and O^+ with N_2 from thermal to 2 eV, *J. Chem. Phys.*, 59, 6620, 1973

[135] Mendillo M., and Baumgardner J., Airglow characteristics of equatorial plasma depletions, *J. Geophys. Res.*, 87, 7641, 1982

[136] Mendillo, M., H. Spence, and S. T. Zalesak, Simulation studies of ionospheric airglow signatures of plasma depletions at the equator, *J. Atmos. Terr. Phys.*, 47, 885, 1985

[137] Mendillo, M., J. Baumgardner, M. Colerico, and D. Nottingham, Imaging Science Contribution to equatorial aeronomy: initial results from the MISETA Program, *J. Atmos. Sol. Terr. Phys.*, 59, 1587, 1997

[138] Meriwether, J. W., J. W. Moody, M. A. Biondi, and R. G. Roble, Optical interferometric measurements of nighttime equatorial thermospheric winds at Arequipa, Peru, *J. Geophys. Res.*, 91, 5547, 1986

[139] Meriwether, J. W., J. L. Mirick, M. A. Biondi, F. A. Herrero and C.G. Fesen, Evidence for orographic wave heating in the equatorial thermosphere at solar maximum, *Geophys. Res. Lett.*, 23, 2177, 1996

[140] Mullan, D. J., and C. W. Smith, Solar wind statistics at 1 AU: Alfven speed and plasma beta, *Sol. Phys.*, 234: 325, 2006

[141] Nicolls, M. J., and M. C. Kelley, Strong evidence for gravity wave seeding of an ionospheric plasma instability, *Geophys. Res. Lett.*, 32, L05108, doi:10.1029/2004GL020737, 2005

[142] Nishida, A, Formation of plasmapause, or magnetospheric plasma knee, by the combined action of magnetospheric convection and plasma escape from the tail, *J. Geophys. Res.*, 71, 5669, 1966

[143] Nishida, A., Geomagnetic D_p 2 fluctuations and associated magnetospheric phenomena, *J. Geophys. Res.*, 73, 1795, 1968a

[144] Nishida, A., Coherence of geomagnetic DP 2 fluctuations with interplanetary magnetic variations, *J. Geophys. Res.*, 73(17), 5549, 1968b

[145] Oliver, W. L., Y. Otsuka, M. Sato, T. Takami and S. Fukao, A climatology of F region gravity wave propagation over the middle and upper atmospheric radar, *J. Geophys. Res.*, 102, 14499, 1997

[146] Ossakow, S. L ., S. T. Zalesak, B. E. McDonald, and P. K. Chaturvedi, Dependence of altitude of F peak and bottomside background electron density gradient scale length, *J. Geophys. Res.*, 84, 17, 1979

[147] Ossakow, S. L., Spread F theories: A review, *J. Atmos. Terr. Phys.*, 43, 437, 1981

[148] Pallam Raju, D., Studies of daytime upper atmospheric phenomena using ground-based optical techniques, *Ph. D. thesis*, Devi Ahilya Vishwa Vidyalaya, 1996

[149] Pant, Tarun Kumar, Study of the thermosphere ionosphere coupling under varying geophysical conditions, *Ph. D. thesis*, Gujarat Univ., 1998

[150] Parker, E. N., Dynamics of the interplaneatry gas and magnetic fields, *Astrophys. J.*, 128, 664, 1958

[151] Patra, A. K., V. K. Ananadan, P. B. Rao, and A. R. Jain, First observations of equatorial spread F from Indian MST radar, *Radio Sci.*, 30, 1159, 1995

[152] Patra, Amit Kumar, A study of the low-latitude ionospheric irregularities using VHF coherent backscatter radar, *Ph. D. Thesis*, S. V. University, Tirupati, India, 1997

[153] Patra, A. K., P. B. Rao, V. K. Anandan, and A. R. Jain, Radar observations of 2.8 m equatorial Spread F irregularities, *J. Atmos. Sol. Terr. Phys.*, 59, 1633, 1997

[154] Peredo, M., J. A. Slavin, E. Majur,and S. A. Curtis, Three dimensional position and shape of the bow shock and their variation with the Alfvenic, sonic and magnetosonic Mach numbers and interplanetary magnetic field orientation, *J. Geophys. Res.*, 100, 7907, 1995

[155] Peterson, V. L., and T. E. VanZandt, and R. B. Norton, F-Region nightglow emissions of atomic oxygen, 1. Theory, *J. Geophys. Res.*, 71, 2255, 1966

[156] Peymirat, C., A. D. Richmond, and A. T. Kobea, Electrodynamic coupling of high and low latitudes: Simulations of shielding/overshielding effects, *J. Geophys. Res.*, 105, 22,991, 2000

[157] Phillips, K. J. H., Feldman, U., Harra, L. K., X-ray observations of long-duration flares, *Astrophys. J.*, 634: 641, 2005

[158] Priedhorsky, W. C., Contrast and signal-to-noise ratio in long-distance starlight imaging, *Appl. Opt.*, 35, 21, 4173, 1996

[159] Prolss, G. W., Perturbation of the low-latitude upper atmosphere during magnetic substorm activity, *J. Geophys. Res.*, 87, 5260, 1982

[160] Raghavarao, R., P. Sharma, and M. R. Sivaraman, Correlation of ionization anomaly with the intensity of the elctrojet, *Space Res.*, XVIII, 277, 1978

[161] Raghavarao, R. and B. G. Anandarao, Vertical winds as a plausible cause for equatorial counter-electrojet, *Geophys. Res. Lett.*, 7, 357, 1980

[162] Raghavarao, R., S. P. Gupta, R. Sekar, R. Narayanan, J. N. Desai, R. Sridharan, V. V. Babu, and R. Sudhakar, *In situ* measurements of winds, electric fields and electron densities at the onset of equatorial spread-F, *J. Atmos. Terr. Phys.*, 49, 485, 1987

[163] Raghavarao, R., S. P. Gupta, , R. Sekar, R. Narayanan, J. N. Desai, R. Sridharan, V. V. Babu, and V. Sudhakar, *In-situ* measurements of winds, electric fields and electron densities at the onset of equatorial Spread F, *J. Atmos. Terr. Phys.*, 49, 485, 1987

[164] Raghavarao, R., R. Sridharan, J. H. Sastri, V. V. Agashe, B. C. N. Rao, P. B. Rao, and V. V. Somayajulu, The equatorial ionosphere, *World Ionosphere/Thermosphere Study in WITS handbook*, Edited by C. H. Liu, and B. Edwards, B., 1, 48, 1988.

[165] Raghavarao, R., L. E. Wharton, N. W. Spencer, and W. R. Hoegy, Neutral temperature anomaly in the equatorial thermosphere - A source of vertical winds, *Geophys. Res. Lett.*, 20, 1023, 1993

[166] Rao, B. C. N., Some characteristic features of the equatorial ionosphere and the location of the F region equator, *J. Geophys. Res.*, 68, 2541, 1963

[167] Rao, P. B., A. R. Jain, P. Kishore, P. Balmuralidhar, S. H. Damle, and G. Vishwanathan, Indian MST radar, 1, System description and sample vector wind measurements in ST mode, *Radio Sci.*, 30, 1125, 1995

[168] Rao, P. B., A. K. Patra, T. V. Chandrasekhar Sarma, B. V. Krishnamurthy, K. S. V. Subbarao, and S. S. Hari, Radar observation of updrafting and downdrafting plasma depletions associated with equatorial Spread F, *Radio Sci.*, 32, 1215, 1997

[169] Rappaport, H. L., Localized modes with zonal neutral wind, diffusion, and shear in equatorial spread F, *J. Geophys. Res.*, 103, A12, 29137, 1998

[170] Rastogi, R. G., and S. Sanatani, Longitudinal effects in the equatorial F_2-region of the ionosphere, *J. Atmos. Terr. Phys.*, 25, 739, 1963

[171] Rastogi, R. G., and V. L. Patel, Effect of interplanetary magnetic field on ionosphere over the magnetic equator, *Proc. Indian Acad Sci.*, 82A, 4, 121, 1975

[172] Rastogi, R., J. Mullen, and E. MacKenzie, Effect of geomagnetic activity on equatorial radio VHF scintillations and spread F, *J. Geophys. Res.*, 86, 3661, 1981

[173] Rastogi, R. G., A. Patil, and S. Alex, Post-sunset uplifting of the equatorial F layer of the ionosphere and vertical plasma drift velocities, *J. Geomag. Geoelec.*, 43, 607, 1991

[174] Rastogi, R. G., h. Chandra, D. Chakrabarty, K. Kitamura, and K. Yumoto, Day-to-day correlation of equatorial electrojet at two stations separated by 2000 km, *Ann. Geophys.*, 25, 875, 2007

[175] Reames V. D., Magnetic topology of impulsive and gradual solar energetic particle events, *Astrophys. J.*, 571, L63, 2002

[176] Reddy, C. A., V. V. Somayajulu, and C. V. Devasia, Global scale electrodynamic coupling of the auroral and equatorial dynamo regions, *J. Atmos. Terr. Phys.*, 41, 189, 1979

[177] Reinisch, B. W., The ionosphere and global electrodynamics of the atmosphere, *Lecture notes*, Workshop on Atmospheric Interactions: Downward and Upward Coupling of the Middle and Upper Atmosphere, ICTP, Trieste, Italy, 5-16 February, 1996

[178] Ridley, A. J., Gang Lu, C. R. Clauer, and V. O. Papitashvili, A statistical study of the ionospheric convection response to changing interplanetary magnetic field conditions using the assimilative mapping of ionospheric electrodynamics technique, *J. Geophys. Res*, 103, A3, 4023, 1998

[179] Ridley, A.J., and M. W. Liemohn, A model-derived storm time asymmetric ring current driven electric field description. Journal of Geophysical Research 107(A8), 2002

[180] Rishbeth, H., Polarization fields produced by winds in the equatorial F-region, *Planet. Space Sci.*, 19, 357, 1971

[181] Rishbeth, H, Dynamics of the equatorial F-region, *J. Atmos. Terr. Phys.*, 39, 1159, 1977

[182] Rishbeth, H, The ionospheric E-layer and F-layer dynamos - a tutorial review, *J. Atmos. Sol-Terr. Phys.*, 59, 15, 1873, 1997

[183] Rishbeth, H, How the thermospheric circulation affects the ionospheric F2-layer, *J. Atmos. Sol-Terr. Phys.*, 60, 1385, 1998

[184] Robbins, D. E., A. J. Hundhausen, and S. J. Bame, Helium in the solar wind, *J. Geophys. Res.*, 75, 1178, 1970

[185] Roelof, E. C., and D. G. Sibeck, Magnetopause shape as a bivariate function of interplanetary magnetic field B_z and solar wind dynamic pressure, *J. Geophys. Res.*, 98, 21421, 1993

[186] Sahai, Y., J. A. Bittencourt, N. R. Teixeira, and H. Takahashi, Simultaneous observations of OI 7774 ^{o}A and [OI] 6300 ^{o}A emissions and correlative study with ionospheric parameters, *J. Geophys. Res.*, 86, 3657, 1981

[187] Sahai et al., Observations of thermospheric neutral winds at 23^{o}S, *Planet. Space Sci.*, 40, 767, 1992a

[188] Sahai et al., Observations of thermospheric temperature at 23^o S, *Planet. Space Sci.*, 40, 1545, 1992b

[189] Sahai, Y., J. Aarons, M. Mendillo, J. Baumgardner, J. A. Bittencourt, and H. Takahashi, OI 630.0 nm imaging observations of equatorial plasma depletions at 16^oS latitude, *J. Atmos. Terr. Phys.*, 56, 1461, 1994

[190] Sandel, B. R., J. Goldstein, D. L. Gallagher, and M. Spasojevic, Extreme ultraviolet imager observations of the structure and dynamics of plasmasphere, *Space Sci. Rev.*, 109: 25, 2003

[191] Sastri, J. H., Equatorial electric fields of ionospsheric disturbance dynamo origin, *Ann. Geophys.*, 6, 635, 1988

[192] Sastri, J. H., H. N. R. Rao, and K. B. Ramesh, Response of Equatorial Ionosphere to the Transit of Interplanetary Magnetic Cloud of January 1315, 1967. Transient Disturbance in F Region, *Planet. Space Sci.* 40, 519, 1992

[193] Sastri, J. H., K. B. Ramesh, and D. Karunakaran, On the nature of substorm-related transient electric field disturbances in the equatorial ionosphere, *Planet. Space Sci.*, 40, 95, 1992

[194] Sastri, J. H., J. V. S. V. Rao and K. B. Ramesh, Penetration of polar electric fields to the night side dip equator at times of geomagnetic sudden commencements, *J. Geophys. Res.*, 98, 17517, 1993

[195] Sastri, J. H., H. Luhr, H. Tachihara, T. I. Kitamura, and J. V. S. V. Rao, Electric field fluctuations (25-35 min) in the midnight dip equatorial ionosphere, *Ann. Geophys.*, 18, 252, 2000

[196] Sastri, J. H., J.V.S. Rao, D. R. K. Rao, and B. M. Pathan, Daytime equatorial geomagnetic H field response to the growth and expansion phase onset of isolated substorms: Case studies and their implications, *J. Geophys. Res.*, 106, 29925, 2001

[197] Sastri, J. H., Penetration electric fields at the nightside dip equator associated with the main impulse of the storm sudden commencement of 8 July, 1991, *J. Geophys. Res.*, 107, A12, 1448, doi:10.1029/2002JA009453, 2002

[198] Sastri, J. H., Y. Kamide, and K. Yumoto, Signatures for magnetospheric substroms in the geomagnetic field of dayside equatorial region: Origin of the ionospheric component, *J. Geophy. Res.*, 108, 1375, doi: 10.1029/2003JA009962, 2003

[199] Scherliess, L., and B. G. Fejer, Storm time dependence of equatorial disturbance dynamo zonal electric fields, *J. Geophys. Res.*, 102(A11), 24037, 1997

[200] Scherliess, L., and B. G. Fejer, Satellite studies of mid- and low-latitude ionospheric disturbance zonal plasma drifts, *Geophys. Res. Lett.*, 25, 1503, 1998

[201] Scherliess, L., and B. G. Fejer, Radar and satellite global equatorial F-region vertical drift model, *J. Geophys. Res.*, 104, 6829, 1999

[202] Schield, M. A., Pressure balance between solar wind and magnetosphere, *J. Geophys. Res.*, 74, 1275, 1969

[203] Schulz, M., and K. Stattegger, Spectrum: Spectral analysis of unevenly spaced paleoclimatic time series, *Computers and Geosciences*, 23, 9, 929, 1997

[204] Schunk, R. W. and J. J. Sojka, Ionosphere-thermosphere space weather issues, *J. Atmos. Terr. Phys.*, 58, 1527, 1996

[205] Sckopke, N., A general relation between the energy of trapped particles and the disturbance field over the Earth, *J. Geophys. Res.*, 71, 3125, 1966

[206] Sekar, R., R. Raghavarao, Role of vertical winds on the RayleighTaylor instabilities of the night time equatorial ionosphere, *J. Atmos. Terr. Phys.*, 49, 981985, 1987

[207] Sekar, R., Plasma instabilities and the dynamics of the equatorial F-region, *Ph. D. Thesis*, Gujarat University, India, 1990

[208] Sekar, R., S. Gurubaran, and R. Sridharan, All sky imaging Fabry- Perot Spectrometer for optical investigation of the upper atmosphere, *Indian J. of Radio & Space Phys.*, 22,197, 1993

[209] Sekar, R., R. Suhasini, and R. Raghavarao, Effects of vertical winds and electric fields in the nonlinear evolution of equatorial spread F, *J. Geophys. Res.*, 99, 2205, 1994

[210] Sekar, R., R. Suhasisni, and R. Raghavarao, Evolution of plasma bubbles in the equatorial F region with different seeding conditions, *Geophys. Res. Lett.*, 22, 885, 1995

[211] Sekar, R, and M. C. Kelley, On the combined effects of vertical shear and zonal electric field patterns on nonlinear equatorial spread F evolution, *J. Geophys. Res.*, 103, 20735, 1998

[212] Sekar, R., E. A. Kherani, P. B. Rao, and A. K. Patra, Interaction of two long-wavelength modes in the nonlinear numerical simulation model of equatorial Spread F, *J. Geophys. Res.*, 106, 24, 765, 2001

[213] Sekar, R., D. Chakrabarty, R. Narayanan, S. Sripathy, A. K. Patra, and K. S. V. Subbarao, Characterizations of VHF radar observations associated with equatorial Spread F by narrow-band optical measurements, *Ann. Geophys.*, 22, 3129, 2004

[214] Senior, C., and M. Blanc, On the control of magnetospheric convection by the spatial distribution of ionospheric conductivities, *J. Geophys. Res.*, 89, 261, 1984

[215] Shirke, J. S., A comparison of electron density profiles over Ahmedabad in year of low and high solar activity, *J. Atmos. Terr. Phys.*, 25, 429, 1963

[216] Sibeck, D. G., R. E. Lopez, and E. C. Roelof, Solar wind control of the magnetopause shape, location, and motion, *J. Geophys. Res.*, 96(A4), 5489, 1991

[217] Sinha, H. S. S., R. N. Misra, H. Chandra, Shikha Raizada, N. Dutt, and G. D. Vyas, Multi-wavelength optical imaging of ionospheric plasma depletions, *Indian J. Radio & Space Phys.*, 25, 44, 1996

[218] Sipler, D. P., and M. A. Biondi, Equatorial F-region neutral winds from nightglow OI 630 nm Doppler shifts, *Geophys. Res. Lett.*, 5, 373, 1978

[219] Sipler, D. P., M. A. Biondi,and R. D. Hake Jr., Studies of the motion of equatorial 630.0 nm airglow depletions, *Planet. Space Sci.*, 29, 1267, 1981

[220] Smith, R. W., Vertical winds: a tutorial, *J. Atmos. Sol-Terr. Phys.*, 60, 1425, 1998

[221] Sobral, J. H. A., M. A. Abdu, C. J. Zamlutti, and I. S. Batista, Association between plasma bubble irregularities and airglow disturbances over Brazilian low latitudes, *Geophys. Res. Lett.*, 7, 11, 980, 1980

[222] Somayajulu, V.V., C. A. Reddy, and K. S. Viswanathan, Simultaneous electric field changes in the equatorial electrojet in phase with polar cusp latitude changes during a magnetic storm. Geophysical Research Letters 12, 7, 473, 1985

[223] Somayajulu, V. V., L. Cherian, K. Rajeev, G. Rajkumar, and C. R. Reddi, Mean wind and tidal components during counter electrojet events, *Geophys. Res. Lett.*, 20(14), 1443, 1993

[224] Somayajulu, V. V., C. A. Reddy, and K. S. Viswanathan, Penetration of magnetospheric electric field to equatorial ionosphere during the sub storm of March 22, 1979, *Geophys. Res. Lett.*, 14, 876879, 1987

[225] Sonnerup, B. U. $\ddot{O}$, Magnetopause reconnection rate, *J. Geophys. Res.*, 81, 1546, 1974

[226] Southwood, D. J., The Role of Hot Plasma in Magnetospheric Convection, *J. Geophys. Res.* 82, 5512, 1977

[227] Spiro, R. W., R. A. Wolf, and B. G. Fejer, Penetration of high latitude electric field effects to low latitudes during SUNDIAL 1984, *Ann. Geophys.*, 6, 39. 1988

[228] Spreiter, J. R., A. L. Summers, and A. Y. Alksne, Hydrodnamic flow around the magnetosphere, *Planet. Space Sci.*, 14, 223, 1966

[229] Spreiter, J. R., and S. S. Stahara, A new predictive model for determining solar wind-terrestrial planet interactions,*J. Geophys. Res.*, 85, A12, 6769, 1980

[230] Sridharan, R., R. Sekar, and S. Gurubaran, Two-dimensional high- resolution imaging of the equatorial plasma fountain, *J. Atmos. Terr. Phys.*, 55, 1661, 1993

[231] Sridharan R., D. Pallam Raju, R. Raghava Rao, and P. V. S. Rama Rao, Precursor to equatorial spread-F on OI 630.0 nm dayglow, *Geophys. Res. Lett.*, 21, 2797, 1994

[232] Sridharan, R. et al., Ionization Hole campaign - a coordinated rocket and ground-based study at the onset of equatorial Spread F : First results, *J. Atmos. Sol. Terr. Phys.*, 59, 2051, 1997

[233] Srivastava Nandita, and P. Venkatakrishnan, Relationship between CME speed and geomagnetic storm intensity, *Geophys. Res. Lett.*, 29, 9, 1287, 10.1029/2001GL013597, 2002

[234] Stening, R. J., and D. E. Winch, Night-time geomagnetic variations at low latitudes, *Planet. Space Sci.*, 35, 12, 1523, 1987

[235] Stening, R. J., C. E. Meek, and A. H. Manson, Upper atmosphere wind systems during reverse equatorial electrojet events., *Geophys. Res. Lett.*, 23(22), 3243, 1996

[236] Sterling, D. L., W. B. Hanson, R. J. Moffett, and R. G. Baxter, Influence of electromagnetic drift and neutral air winds on some features of the F2-region, *Radio sci.*, 4, 1005, 1969

[237] Stern, D.P., The motion of a proton in the equatorial magnetosphere, *J. Geophys. Res.* 80, 595, 1975

[238] Stolarski, R. S., P. B. Hays, and R. G. Roble, Atmospheric heating by solar EUV radiation, *J. Geophys. Res.*, 80, 2266, 1975

[239] Stolarski, R. S., Energetics of the midlatitude thermosphere, *J. Atmos. Terr. Phys.*, 38, 863, 1976

[240] Subbarao, K. S. V., and B. V. K. Krishna Murthy, Seasonal variations of equatorial spread-F, *Ann. Geophys.*, 12, 33, 1994

[241] Sultan, P. J., Chemical release experiments to induce F region ionospheric plasma irregularities at the magnetic equator, Ph.D. Dissertation, Boston Univ., Boston, Mass, 1994

[242] Sutton, E. K., J. M. Forbes, R. S. Nerem, and T. N. Woods, Neutral density response to the solar flares of October and November, 2003, *Geophys. Res. Lett.*, 33, L22101, doi:10.1029/2006GL027737, 2006

[243] Szuszezewicz, E. P., R. T. Tsunoda, R. Narcisi, and J. C. Holmes, Coincident radar and rocket observations of equatorial spread F, *Geophys. Res. Lett.*, 7, 537, 1980

[244] Takahashi, H., Y. Sahai, B. R. Clemesha, D. Simonich, N. R. Teixeira, R. M. Lobo, and A. Eras,, Equatorial mesospheric and F region airglow emissions observed from 4^o south, *Planet. Space Sci.*, 37, 649, 1989

[245] Tinsley, B. A., A. B. Cristenson, J. A. Bittencourt, H. Gouveia, P.D. Angreji, and H. Takahashi, Excitation of oxygen permitted line emissions in the tropical nightglow, *J. Geophys. Res.*, 78, 1174, 1973

[246] Tinsley, B. A., and J. A. Bittencourt, Determination of F region height and peak electron density at night using airglow emissions from atomic oxygen, *J. Geophys. Res.*, 80, 2333, 1975

[247] Tinsley, B. A., R. P., Rohrbaugh, W. B. Hanson, and A. L. Broadfoot, Images of transequatorial F region bubbles in 630 and 777.4 nm emissions compared with satellite measurements,*J. Geophys. Res.*, 102, 2057, 1997

[248] Toffoletto, F., S. Sazykin, R. Spiro, and R. Wolf, Inner magnetospheric modeling with the Rice Convection Model, *Space Sci. Rev.*, 197, 175, 2003

[249] Tsunoda, R. T., and D. M. Towle, On the spatial relationship of 1-meter equatorial Spread F irregularities and depletions in total electron content, *Geophys. Res. Lett.*,6, 873, 1979

[250] Tsunoda, R. T., Magnetic field-aligned characteristic of plasma bubbles in the night time equatorial ionosphere, *J. Atmos. Terr. Phys.*, 42, 743, 1980

[251] Titheridge, J. E. , Bulletin No. 62, *Ionosonde Network Advisory Group (INAG)* under the auspices of Commission G, Working Group G 1 of the International Union of Radio Science (URSI), January, 1998

[252] Toffoletto, F., S. Sazykin, R. Spiro, and R. Wolf, Inner magnetospheric modeling with the Rice Convection Model, *Space Sci. Rev.*, 197, 175, 2003

[253] Torr, M. R., and D. G. Torr, The role of metastable species in the thermosphere, *Rev. Geophys. Space Phys.*, 20, 91, 1982

[254] Tsurutani, B. T., et al., The October 28, 2003 extreme EUV solar flare and resultant extreme ionospheric effects: Comparison to other Halloween events and the Bastille Day event, Geophys. Res. Lett., 32, L03S09, doi:10.1029/2004GL021475, 2005

[255] Vasyliunas, V. M., Mathematical models of magnetospheric convection and its coupling to the ionosphere, in *Particles and Fields in the Magnetosphere*, edited by B. M. McCormac, pp. 60, D. Reidel, Norwell, Mass, 1970

[256] Vasyliunas, V., The interrelationship of magnetospheric processes, in *Earths Magnetospheric Processes*, edited by B. M. McCormac, pp. 29, Springer, New York, 1972

[257] Volland, H., A semiempirical model of large-scale magnetospheric electric fields, *J. Geophys. Res.* 78, 171, 1973

[258] Weber, E. J., J. Buchau, R. H. Eather, and S. B. Mende, North-South aligned equatorial airglow depletions, *J. Geophys. Res.*, 83, 712, 1978

[259] Wolf, R. A., Effects of ionospheric conductivity on covective flow of plasma in the magnetosphere, *J. Geophys. Res.*, 75, 4677, 1970

[260] Wolf, R.A., Calculations of magnetospheric electric fields. In: McCormac, B.M. (Ed.), *Magnetospheric Physics*, D. Reidel, Dordrecht, Holland pp. 167, 1974

[261] Wolf, R. A., T. W. Garner, J. Goldstein, S. Sazykin, R. W. Spiro, Storm-time magnetospheric effects on electric fields in the subauroral ionosphere, *AGU Fall Meeting, 2001*, 2001AGUFMSA21A..12W, 2001

[262] Wolf, R. A., R. W. Spiro, S. Sazykin, and F. R. Toffoletto, How the Earth's inner magnetosphere works: An evolving picture, *J. Atmos. Sol-Terr. Phys.*, 69, 288, 2007

[263] Woodman, R. F., and C. La Hoz, Radar observations of F region equatorial irregularities, *J. Geophys. Res.*, 81, 5447, 1976

[264] Zalesak, S. T., Fully multidimensional flux-corrected transport algorithms for fluids, *J. Comput. Phys.*, 31, 335, 1979

Scope of the thesis

Certain scientific issues, which are envisaged during the course of this work and are beyond the scope of the present thesis, can be addressed in future investigations. They are listed as follows.

- It is observed that 630.0 nm airglow intensity falls off rapidly during twilight hours. This is owing to the combined effects of decreasing solar radiation as well as due to the ascent of F layer during post-sunset hours under the influence of pre-reversal enhancement (PRE) of zonal electric field. In order to delineate the contribution of the F layer height variation from the decreasing solar radiation effect, airglow data after the F region local sunset should be critically scrutinized. The relationship between the rate of fall of the airglow intensity after F region sunset and F layer height rise can be explored to reveal the signatures of PRE in airglow and its association with day-to-day occurrence of equatorial spread F (ESF) events.

- "Fossil bubbles" are plasma bubbles at non-evolutionary phases of ESF. Investigations on fossil bubbles will help to understand the decay phase of ESF. Based on simultaneous VHF radar and optical investigations, "fossil bubbles" can be characterized and their dynamics can be studied.

- It is now well known that atmospheric gravity waves act as seed perturbation in the generation of ESF by facilitating Rayleigh-Taylor instability mechanism. However, it is difficult to identify the gravity wave modes responsible for the seeding of ESF events. Coordinated campaigns involving wind measurements at lower and middle atmosphere as well as ESF observations by radar and optical techniques can be used to throw light on the gravity wave modes acting as seed perturbations.

- It is found that different periodic components ($\leq$ 2.0 hr) in interplanetary electric field (IEF) affect the low latitude ionosphere during different PP events although the theoretical shielding time constant is $\sim$ 0.5 hr [*Senior and Blanc*, 1984]. The frequency dependence of the magnetosphere-ionosphere shielding, therefore, needs to be understood comprehensively.

- Observational evidences are available [*Kelley et al.*, 2003; *Huang et al.*, 2005, 2007] on the long duration PP events. The shielding, it seems, remains unsettled for longer

duration on many occasions. It is, therefore, important to understand comprehensively what decides the magnitude and duration of prompt penetration (PP) events keeping in mind the enormous effects these events have on the equatorial F region electrodynamics.

- In this work, the signatures of PP is found in OI 630.0 nm airglow. This opens up a fairly inexpensive way to track the IEF effects over low latitudes in high temporal resolution mode. In similar line, attempts can be made to identify the signature of disturbance dynamo (DD) mechanism in OI 630.0 nm airglow. The next task will be to devise a concrete methodology to delineate PP and DD signatures in airglow data.

- The two-dimensional non-linear numerical simulation model [*Sekar et al.,* 1990] used in this work can be augmented into a three-dimensional model by incorporating the field-line integrated conductivity effects on the development of ESF. Afterwards, storm time variabilities of ESF can be comprehensively addressed by the three-dimensional model.

- 777.4 nm airglow intensity variations need to be critically studied and compared with F region parameters as there are indications that 777.4 nm airglow intensity may have first order dependence on F layer height variations on certain occasions. Meridional wind and total electron content (TEC) observations should be made in conjunction with 777.4 nm airglow observation to address this aspect.